A Likelihood Method for Determining the On-orbit Point-Spread Function of the *Fermi* Large-Area Telescope

Marshall Roth

A dissertation submitted in partial fulfillment
of the requirements for the degree of

Doctor of Philosophy

University of Washington

2012

Program Authorized to Offer Degree: Department of Physics

University of Washington

Abstract

A Likelihood Method for Determining
the On-orbit Point-Spread Function
of the *Fermi* Large-Area Telescope

Marshall A. Roth

Chair of the Supervisory Committee:
Professor Thompson Burnett
Physics

The Large-Area Telescope (LAT) on the *Fermi* Gamma-Ray Space Telescope is a pair-conversion γ-ray telescope with unprecedented capability to image astrophysical γ-ray sources between 20 MeV and 300 GeV. The pre-launch performance of the LAT, decomposed into effective area, energy and angular dispersions, was determined through extensive Monte Carlo (MC) simulations and beam tests. The point-spread function (PSF) characterizes the angular distribution of reconstructed photons as a function of energy and geometry in the detector.

Here we present a set of likelihood analyses of LAT data based on the spatial and spectral properties of sources, including a determination of the PSF on orbit. We find that the PSF on orbit is generally broader than the MC at energies above 3 GeV and consider several systematic effects to explain this difference. We also investigated several possible spatial models for pair-halo emission around BL Lac AGN and found no evidence for a component with spatial extension larger than the PSF.

ACKNOWLEDGMENTS

I have been very fortunate to be supported by many individuals during my graduate studies, including faculty, colleagues, family, and friends. First and foremost is Toby Burnett, who served as my gateway into the world of data analysis and scientific research. He was patient and encouraging as I discovered the skills of an effective scientist, and for that I am truly thankful. Equally important in my graduate studies has been Jeff Wilkes, whose insight and eloquence in the presentation of science to all audiences I will always try to emulate.

At the University of Washington, I would first like to thank my officemates current and past, Eric Wallace and Matthew Kerr. Both have served as great collaborators and friends, and helped keep my sanity. I'd like to thank Toby, Jeff, Ann Nelson, Miguel Morales, and Scott Anderson for serving on my committee and reading my work. I'd also like to thank Steve Sharpe and Catherine Provost for support and encouragement in the graduate program. Todd Olsen has provided excellent support and maintained a high performance computing cluster, without which this work would not be possible. Finally, I'd like to thank Laura Bodine, Will Terrano, Mike Dziomba, Keven Connolly, and Scott Davis for their feedback on my presentations over the years.

As part of the *Fermi* Collaboration, I have a number of individuals to thank, including the collaboration itself for providing me the means to research and travel. I'd first like to thank Julie McEnery, Rob Cameron, and Eduardo do Couto e Silva for getting me involved early on in the LAT operations. Seth Digel has provided an immense amount of feedback on my work, from presentations to publications, and an attention to detail which has been helpful in developing my communication skills. Eric Charles, Luca Baldini, Leon Rochester, Riccardo Rando, Benoit Lott, Gino Tosti, and Teddy Cheung have been instrumental in providing both a forum to present my work and feedback on my work. I'd also like to thank Josh Lande for becoming an honorary UW group member and facilitating the development of *pointlike* within the collaboration. Finally, I'd like to thank Matthew Wood for the endless hours of reviewing work together and collaborating on my first scientific publication.

My family has been especially supportive through my graduate studies. My parents, Bruce and Cindy, are more than any son could ask for: providing the level of emotional support above and beyond what I could have ever expected. My grandparents have also provided me with the means to seek my goal of becoming a researcher, and I am eternally grateful.

This work was funded in part by the National Aeronautics and Space Administration and the Department of Energy in the United States as well as a National Science Foundation Major Research Instrumentation grant and the University of Washington College of Arts and Sciences.

I dedicate this paper to my family.

Contents

1 Outline 1

2 Introduction: γ-ray Astronomy 3
- 2.1 γ-ray Telescopes . . . 3
  - 2.1.1 Satellites . . . 4
  - 2.1.2 Ground Based . . . 5
- 2.2 γ-ray Sources . . . 5
  - 2.2.1 Pulsars . . . 5
  - 2.2.2 Active Galactic Nuclei . . . 6
  - 2.2.3 Diffuse Emission . . . 9
  - 2.2.4 Earth . . . 9
- 2.3 Summary . . . 10

3 *Fermi* Large-Area Telescope (LAT) 11
- 3.1 Systems . . . 11
  - 3.1.1 Tracker . . . 11
  - 3.1.2 Calorimeter . . . 12
  - 3.1.3 Anti-coincidence Detector . . . 13
- 3.2 Environment . . . 14
- 3.3 Triggering and Reconstruction . . . 15
- 3.4 LAT data . . . 16
- 3.5 Summary . . . 17

4 Instrument Performance 19
- 4.1 Instrument Response Functions (IRFs) . . . 19
- 4.2 PSF . . . 21
- 4.3 Effective Area . . . 24
- 4.4 Energy Dispersion . . . 25
- 4.5 Summary . . . 26

5 Likelihood Analysis 31
- 5.1 Maximum Likelihood . . . 31
- 5.2 Likelihood Analysis of LAT Data . . . 33
- 5.3 Summary . . . 36

6 LAT Boresight Alignment 38
- 6.1 Determination from Likelihood Analysis . . . 38
- 6.2 L&EO Boresight Alignment . . . 39
- 6.3 3-year Analysis and Boresight Alignment Residuals . . . 42

6.4 Systematic Uncertainties, Stability, and Periodicity 43
6.5 Summary 46

7 Determination of the On-Orbit PSF 51
7.1 On-Orbit PSF from Bright AGN 51
7.2 Validation 55
7.3 Systematic Errors of the PSF 59
7.4 Inclination angle-Dependent On-Orbit PSF 61
7.5 Validation of Inclination-angle Dependent On-Orbit PSF 65
7.6 Summary 66

8 The Intergalactic Magnetic Field 75
8.1 Overview 75
8.2 Pair-Halo Phenomena 76
8.3 Maximum Likelihood Analysis in Angular Bins 78
8.4 Limits on the pair-halo emission of 1FGL BL Lac Sources 81
8.5 Limits on the pair-halo emission of TeV BL Lacs 85
8.6 Summary 87

9 Summary 90

List of Figures

2.1 The histograms of the γ-ray phase values for the Vela pulsar (above) and the spectral energy distribution (SED, below) for the phase averaged spectrum for the Vela pulsar from Abdo et al. (2010e). The pulsar emission is effectively turned off between 0.7−1.0 of the pulse phase, making the pulsar emission separable from the background. The pulsar spectra are exponentially cut-off above a few GeV, with limited emission > 10 GeV. 7

2.2 The broadband average spectral energy distribution (SED) of a set of 126 blazars from Fossati et al. (1998). The low energy peak ($10^{13} - 10^{17}$ Hz) corresponds to the peak in the synchrotron spectrum and the high energy peak ($10^{21} - 10^{25}$ Hz) corresponds to the inverse Compton peak. 8

2.3 The *Fermi* model for diffuse Galactic emission at 1 GeV in an Aitoff projection centered at the Galactic center. The brightness at low galactic latitudes follows the matter distribution of the galactic disk. The diffuse emission at high latitudes comes mainly from local cosmic-ray interactions. 9

3.1 A single TKR/CAL module (left) and a cutout schematic of the LAT showing the layout of the 16 TKR/CAL modules (right). On the left diagram, the *front* TKR planes are indicated by the thin grey squares, the *back* planes are indicated by the thick grey squares, and the last two TKR layers with no tungsten with the dotted grey squares. The CAL is the cube below the TKR planes. On the right diagram, the coordinates of the LAT are defined including the inclination angle (θ) the angle from the boresight. The images are taken from a LAT performance paper in preparation. 13

3.2 The exposure variation over the sky in galactic coordinates. The exposures (a)−(d) correspond to the initial 35° rocking angle profile of the LAT for (a) 3 hours ($\sim$ 2 orbits), (b) 1 day, (c) 1 month, and (d) 1 year. Figure (e) is also a 1 year exposure, but for the 50° rocking angle profile. In (e) the orbital poles are over-exposed compared to the 35° rocking angle profile. 15

3.3 Rates at several stages of the data acquisition and reduction process on a typical day (2011 August 17) from a LAT performance paper in preparation. Starting from the highest, the curves shown are for the rates: (i) at the input of the hardware trigger process, (ii) at output of the hardware trigger, (iii) at the output of the on-board filter, (iv) after the classification of all good reconstructed events (`P7TRANSIENT` γ-ray), (v) after the primary selection on γ rays (`P7SOURCE` γ-ray), and (vi) the `P7SOURCE` γ-ray selection with an additional cut on the zenith angle ($\theta_z < 100°$, to remove the Earth's contamination). 16

4.1 Comparison of best-fit Gaussian, single, and double King function fits to a MC angular distribution of *Diffuse* event class γ-rays histogram with energy of 7.5 GeV impinging at inclination angles between 26 and 37° uniformly in solid angle. The best-fit Gaussian, determined by binned likelihood, gives a poor representation of the PSF at small and large separations because of power-law tails at large angles. 28
4.2 Comparison between the *front* (left) and *back* (right) effective area for the `P6_V3` IRF. The energy bins are logarithmically spaced between 17 MeV and 562 GeV, while the $\cos\theta$ bins are spaced linearly between 0.2 (off-axis) and 1.0 (on-axis). 29
4.3 An example of a 'ghost' event taken from a LAT performance paper in preparation. The LAT is projected in the $y-z$ plane with the TKR planes (above), the CAL crystals (below) and the ACD tiles hit (large colored squares), The x's represent the consecutive hits in the TKR of a charged particle traversal. The size of the squares in the CAL correspond to the energy deposited and the dotted line corresponds to the γ-ray direction. 30

5.1 The contours for the ratio of the mean energy $\bar{E}$ of a bin to the geometric mean energy $E_g = \sqrt{E_{min}E_{max}}$ of the bin. The red line shows the relation $\bar{E} = E_g$ for sources with spectra that follow $E^{-3/2}$, the solid black line indicates the contour where $(\bar{E}-E_g)/\bar{E} = \pm 5\%$, and the dashed line indicates $\pm 10\%$. 37

6.1 Projection of the log-likelihood surfaces for the boresight alignment correction into each of the planes a) θ_y-θ_x, b) θ_z-θ_x and c) θ_z-θ_y for one day of data (3 August 2008). The origin corresponds to the ideal alignment and the contours denote the 68% (dashed) and 95% (solid) containment. The elongation of the projected surfaces with respect to the θ_z correction is due to fewer statistics at larger inclination angles. The units are in arcminutes and the L&EO correction to the boresight alignment corresponds to the coordinate $(\theta_x, \theta_y, \theta_z) = (-2.83, -2.88, -8, 18)$. 47
6.2 Boresight alignment residuals $\Delta\theta_x$ (top), $\Delta\theta_y$ (middle), $\Delta\theta_z$ (bottom), determined from the analysis of weekly time bins for three years of data as a function of the mission-elapsed time (MET). The red bands for each parameter are the weighted average values and uncertainties evaluated from Equation 6.11. 48
6.3 Boresight alignment residuals $\Delta\theta_x$ (top), $\Delta\theta_y$ (middle), $\Delta\theta_z$ (bottom), determined from the analysis of monthly time bins for three years of data as a function of the mission-elapsed time (MET). The red bands for each parameter are the weighted average values and uncertainties evaluated from Equation 6.11. 49
6.4 Boresight alignment residuals $\Delta\theta_x$ (top), $\Delta\theta_y$ (middle), $\Delta\theta_z$ (bottom), determined from the analysis of yearly time bins for three years of data as a function of the mission-elapsed time (MET). The red bands for each parameter are the weighted average values and uncertainties evaluated from Equation 6.11. 50

7.1 Comparison of 68% (solid lines) and 95% (dashed lines) containment radii of the MC and on-orbit PSF models for front- (left) and back-converting (right) events. 68
7.2 68% (white points) and 95% (black points) PSF containment radii inferred from applying the on-orbit PSF analysis to a simulated AGN sample (Stack) with the same properties of the calibration AGN sample generated with the P6_V3 PSF for front- (left) and back-converting (right) events. Solid lines show the containment radii predicted by the same IRF used to generate the simulation. 68
7.3 Light curve for all γ rays above 100 MeV within 4° of the Vela (above) and Geminga (below) pulsars in 100 fixed-count phase bins. The on- and off-pulse phase selections are identified in green and red, respectively. 69
7.4 Containment radii for *front* events as determined from the angular distributions of Vela and the stacked AGN sample. Solid and dashed curves show the 68% and 95% containment radii, respectively, given by the model predictions for the P6_V3 and P6_V11 instrument response functions, for an observing profile corresponding to the Vela pulsar and a power-law energy distribution with photon index $\Gamma = 2$. The middle and lower panels show the fractional residual between the Vela and stacked AGN PSFs and the different IRFs for the 68% and 95% PSF containment radii, respectively. 70
7.5 Same as for Figure 7.4, but for *back* events. 71
7.6 The energy bins for the theta-dependent on-orbit PSF analysis. The pulsar emission can be effectively separated from the background between 100 MeV to 10 GeV and provide significant statistics below 1 GeV. The AGN have emission at all energies, but begin to overlap with other sources at 1 GeV. 72
7.7 A comparison between the 68 and 95% containment radii ($A_{\rm eff}$-averaged) for the MC PSF (P7_V6MC), the on-orbit PSF from Section 7.1 for Pass7 data (P7_V6), and the PSF generated from Section 7.4 with inclination-angle dependence (P7_V11). The PSFs are plotted for both *front* and *back* converting γ rays. The discrepancy between data and MC is present in both conversion types, most prominently above 10 GeV. 72
7.8 The square root of the power density spectrum (PDS) $|F|$ of the weekly estimate of the total flux for the Vela pulsar for γ rays with energy above 70 MeV. The PDS is shown for the MC PSF (top, P7SOURCE_V6MC), the inclination-angle independent on-orbit PSF (middle, P7SOURCE_V6), and the inclination angle-dependent on-orbit PSF (bottom, P7SOURCE_V11). The large peaks in the spectrum at 50−52 days correspond to the 53.4-day precession period of the LAT's orbit and have a significance $> 4\sigma$ over the null distribution. . . 73
7.9 Same as 7.8, but with the Geminga pulsar. The peak at orbital precession period (53.4 days) is reduced for all PSFs, but still contains significance of $> 4\sigma$ for P7SOURCE_V6 (middle) as expected since the PSF has no inclination angle dependence. 74

8.1 The geometry of the pair-halo emission and the intergalactic magnetic field (IGMF, reproduced from Dermer et al., 2011). θ_j is the opening angle of the AGN jet, $\lambda_{\gamma\gamma}$ is the mean free path for the TeV pair conversion, θ_{dfl} is the deflection angle due to the magnetic field, and λ_{PSF} is the effective distance along the trajectory that can be resolved by the LAT. If $\lambda_{PSF} \ll \lambda_{\gamma\gamma}$, the LAT can effectively distinguish the extended spatial emission due to the IGMF. 78
8.2 95% upper limits on the fraction of halo model γ rays from the low redshift BL Lacs, assuming a 0.1° (**a**), 0.5° (**b**), and 1.0° (**c**) halo. 84
8.3 95% upper limits on the fraction of halo model γ rays from the high redshift BL Lacs, assuming a 0.1° (**a**), 0.5° (**b**), and 1.0° (**c**) halo. 85
8.4 Upper limits on the energy flux from 1ES0229+200 at the 95% confidence level assuming a 0.1° (**a**), 0.5° (**b**), and 1.0° (**c**) halo, plotted with observations from HESS and VERITAS. 88
8.5 Upper limits on the energy flux from 1ES0347-121 at the 95% confidence level, plotted with observations from HESS assuming a 0.1° (**a**), 0.5° (**b**), and 1.0° (**c**) halo. 89

List of Tables

3.1 The definition of the common parameters in the *Fermi* data products: γ ray data (*FT1*) and spacecraft data (*FT2*). The rows of *FT1* correspond to each event, while the rows *FT2* are for each Good Time Interval (GTI) of 30 seconds of observation. The 30 second GTI for the *FT2* allows for smooth interpolation of the spacecraft pointing data. 17

4.1 The energies of the particles in the beam test of the LAT Calibration Unit (CU). The data were taken at the CERN Proton Synchrotron (PS) and Super Proton Synchrotron (SPS) beams over a wide range of CU orientations (Baldini et al., 2007). 20

4.2 The parameters of the scale function $S_P(E \mid c_0, \beta, c_1)$ for the σ parameter from a simulation of the LAT performance. The parameters are divided into their respective conversion regions: *front* and *back*. 24

6.1 The boresight alignment parameters and the parameter uncertainties calculated from Equation 6.11. The time bin width, t, is measured in days and N_{bins} is the number of time bins in the analysis. The change in the boresight alignment parameters, $\{\Delta\theta_x, \Delta\theta_y, \Delta\theta_z\}$, are measured in arcseconds. 44

6.2 The stability of the boresight alignment parameters in days evaluated from Equation 6.12 for the daily and weekly time bins. The stability of each parameter, S, is expressed in days. 45

6.3 The periods from the DFT of the residuals with a significance greater than 2σ for each boresight alignment parameter in the weekly analysis. The number of fluctuations per alignment parameter are predicted from null distribution to be ≈ 2, so the fluctuations are consistent with the null hypothesis (i.e. no significant periodicity). 46

7.1 The parameters of the scale function $S_P(E)$ representing the 68 and 95% containment radii for the MC (`P6_V3`) and on-orbit (`P6_V11`) PSF. The parameter c_0 corresponds to the containment radius at 100 MeV due primarily to multiple scattering, c_1 corresponds to the containment radius at 100 GeV defined by the geometric angle, and β is the power-law dependence of the multiple scattering. 56

7.2 On- and off-pulse phase selection for Vela and Geminga pulsars. 57

7.3 68% containment radii of the LAT PSF for *front* events in the *Diffuse* class as a function of energy bin inferred from different calibration data sets: Vela, Geminga, and the AGN calibration sample. The containment radius of a source with the observing profile of Vela and a power-law energy distribution with a photon index $\Gamma = 2$ calculated with the `P6_V3` and `P6_V11` IRFs is shown for comparison. 57
7.4 68% containment radii of the LAT PSF for *back* events in the *Diffuse* class as a function of energy bin inferred from different calibration data sets: Vela, Geminga, and the AGN calibration sample. The containment radius of a source with the observing profile of Vela and a power-law energy distribution with a photon index $\Gamma = 2$ calculated with the `P6_V3` and `P6_V11` IRFs is shown for comparison. 58
7.5 The comparison of the average absolute flux normalization $\bar{F}_n$ and uncertainty $\bar{\sigma}_n$ for the PSFs normalized to the flux normalization obtained by the MC PSF `P7SOURCE_V6MC`. 66

8.1 Statistics for the Vela and Geminga pulsars and the low and high redshift BL Lacs in the energy range $1000 - 3162$ MeV for the analysis in Section 4.2. The models for the on-pulse selection ν_i^{on} are displayed next to the number of counts n_i^{on} in each angular bin. The BL Lac model counts ν_i^{agn} are fit for the null case ($N^{halo} = 0$) in Equation 7.5. 81
8.2 As Table 8.1 with the energy range $3162 - 10000$ MeV. 82
8.3 As Table 8.1 with the energy range $10000 - 31623$ MeV. 82
8.4 Statistics for the low-redshift BL Lacs in the energy range $31623 - 100000$ MeV for the analysis in Section 4.3. The model for the BL Lacs, ν_i^{agn}, is displayed next to the number of counts, n, in each angular bin. $N^{agn} m_i$ is displayed to highlight the equal statistics of the BL Lacs in each angular bin. 83
8.5 Summary of the 95% C.L. upper limits on the fraction ($f_{halo} = N^{halo}/(N^{halo} + N^{agn})$) of γ-ray emission from low-redshift BL Lacs attributable to a halo component for the PSF convolved Disk and Gaussian halo models. 86
8.6 Summary of the 95% C.L. upper limits on the fraction ($f_{halo} = N^{halo}/(N^{halo} + N^{agn})$) of γ-ray emission from high-redshift BL Lacs attributable to a halo component for the PSF convolved Disk and Gaussian halo models. 86

Chapter 1

Outline

In Chapter 2, we introduce the field of γ-ray astronomy, including some background from other experiments. We also introduce the current known astrophysical sources of γ rays, including their spectral, spatial, and temporal properties.

In Chapter 3, we describe the properties of *Fermi* and the Large-Area Telescope (LAT), the primary imaging instrument on the spacecraft. We cover each of the subsystems on the LAT responsible for imaging, reconstruction of energy, and rejection of background. We characterize the on-orbit environment, including regions of the orbit where the LAT is unable to acquire γ-ray data. Finally, we outline the triggering and reconstruction processes, as well as the data products produced by the LAT collaboration.

In Chapter 4, we describe the determination and properties of the LAT performance based on Monte Carlo (MC) simulations. We overview the calibration of a subset of the LAT with collider beams and the comparison to the MC predicted performance. We characterize the primary areas of concern in instrument performance: the reconstruction of the γ-ray directions, the measurement of the γ-ray energy, and the effective collection area of the LAT.

In Chapter 5, we outline the method of maximum likelihood and the application to LAT data. We describe methods for assessing significance of models and determining uncertainty in parameter estimation. We describe how to model the effects of the instrument in likelihood analysis of LAT data. We characterize tools used by the collaboration to model γ-ray sources in energy and location on the sky.

In Chapter 6, we outline a method to determine the orientation of the LAT boresight

with respect to the spacecraft. We measure this orientation (boresight alignment) for the Launch and Early Orbit (L&EO) period of observation, the first 55 days of observations post launch, using a likelihood-based analysis. We also examine the boresight alignment of the LAT as a function of time for periodicity and significant changes.

In Chapter 7, we outline a likelihood method for determining the on-orbit performance of the LAT reconstruction of γ-ray directions, or the point-spread function (PSF). We determine the performance of the on-orbit reconstruction performance and cross-check the results with calibration sources and the MC performance. We evaluate the magnitude of systematic errors from instrument calibrations to identify sources of discrepancy between data and MC. We create a more sensitive determination of the PSF and cross-check the determination against bright sources.

Finally, in Chapter 8, we examine properties of the intergalactic magnetic field and the high energy γ-ray emission of active galactic nuclei (AGN). In particular, we examine the process of pair-halo γ-ray production by relativistic leptons from the jets of AGN. We apply a binned likelihood analysis to classes of AGN and to individual sources, and calculate upper limits on the emission from pair-halo interactions.

Chapter 2

Introduction: γ-ray Astronomy

In the late 1960s, the United States commissioned a set of satellites to monitor the testing of nuclear arms following the signing of a treaty with the Soviet Union. The *Vela* satellites flew with both X-ray and γ-ray CsI detectors, which were capable of detecting photons between $0.2 - 1.5$ MeV and had roughly isotropic sensitivity (Klebesadel et al., 1973). While the satellites were intended to observe terrestrial sources of high energy photons, the signature of nuclear detonation, the satellites observed 16 short bursts of high-energy γ rays from extragalactic sources. Dubbed "gamma-ray bursts" or GRBs, these objects emitted astounding amounts of energy, nearly 10^{46} ergs, in a matter of a few seconds. Until the advent of the observation of GRBs, the γ-ray sky was thought to be simple an isotropic background driven by cosmic-ray interactions. With such mysterious observed high energy phenomena, scientists motivated subsequent missions such as the National Aeronautics and Space Administration's (NASA) SAS-2 (Fichtel et al., 1975b; Oegelman et al., 1975) and the European Space Agency's (ESA) COS-B (Hermsen et al., 1981) and began to pick out localized gamma-ray sources associated with a variety of astrophysical objects. In the following section, we enumerate and describe a selection of known γ-ray sources of significance to the *Fermi* mission.

2.1 γ-ray Telescopes

γ rays are the most energetic incarnation of electromagnetic radiation, capping the upper energy range of the spectrum beginning at about 20% of the electron rest energy (100 keV). Unlike conventional telescopes, γ rays can not be effectively refracted or focused, so we

must rely on secondary electromagnetic interactions with matter to infer the properties of the primary γ rays. Above 10 MeV, the primary process for γ rays and matter is pair production off of the electric field of atoms. For heavy nuclei, such as lead, this process is amplified, so experiments which detect primary γ rays require layers of converting material. However, to detect the primary astrophysical γ rays *in situ* requires observation above the Earth's ionosphere, which (helpfully for all life on Earth) attenuates the γ-ray intensity at Earth's surface. The only practical limitation for detecting γ rays with satellites is the sources themselves, which need to produce enough flux to be collected by an observatory no more than a few square meters in size. Since nearly all astrophysical sources are turning off at high energy, satellite based observatories are limited to a maximum energy of $\sim$300 GeV. For ground based detectors, the atmosphere itself is the converting material, producing electromagnetic cascades for the highest energy γ rays and providing a large collection area. Thus the connection between the MeV$-$TeV observation of sources is the synthesis between satellites and ground based observatories.

2.1.1 Satellites

The field of satellite-based γ-ray astronomy is relatively young and has been limited primarily by the ability to spatially resolve sources and provide a reasonable collection area. SAS-2 (the Second Small Astronomy Satellite) and COS-B were spark chamber based telescope satellites with tungsten converter, an effective area of $360-640$ cm^2, an optimal spatial resolution of 2° and an energy range of $30-1000$ MeV. (Bignami et al., 1975; Fichtel et al., 1975a). The last of the spark chamber telescopes was NASA's Energetic Gamma Ray Experiment Telescope (EGRET), which had a significantly larger collection area of 1200cm^2, the best optimal angular resolution of 0.4°, and an effective energy range between $35-30000$ MeV (Kanbach et al., 1988). The performance of these telescopes motivated the design of the future γ-ray telescope in two ways: 1) the development of a silicon based tracking system from particle physics experiments, to remove the consumable dependence of the spark chambers and 2) the development of a segmented anti-coincidence dome to conserve effective collection.

The *Fermi* Large Area Telescope (LAT) was the result of implementing these new technologies, vastly improving the background rejection, angular resolution, energy measurement, and effective area. In the following chapters we will outline the performance of the LAT both in simulations and with data.

2.1.2 Ground Based

Ground-based γ-ray telescopes observe the electromagnetic cascades from γ rays by observing the Cerenkov light produced by the relativistic electrons propagating in the atmosphere. On moonless nights in particular, the nitrogen in the atmosphere produces optical$-$UV light that can be observed by stereoscopic optical telescopes. By examining the structure of the shower development, the telescopes can separate γ-ray and cosmic-ray interactions in the atmosphere and reconstruct γ-ray directions and energy. The high energy energy range is crucial for measuring the properties of active galaxies, which often have emission well above 1 TeV, and the properties of the radiation fields between galaxies.

2.2 γ-ray Sources

While there is great variety in the sources of astrophysical γ rays in the universe, for the purposes of this paper we will focus on a subset of the most important classes for the analysis presented here. In the following sections we will discuss local, galactic sources of γ rays, such as pulsars and the Earth as well as distant, extragalactic sources, such as active galaxies.

2.2.1 Pulsars

Pulsars are rapidly rotating, highly magnetized neutron stars of roughly 1.4 $M_{\odot}$. The pulsars have periodic emission in many energy bands with periods P between $10^{-3} - 10^{1}$ seconds. A pulsar can be viewed as a dipole magnetic field $\vec{B}$ rotating about an axis $\vec{\Omega}$, which results in electromagnetic radiation. The radiation slowly decreases the angular momentum of the pulsar, increasing the period of rotation $\dot{P} > 0$.

The γ-ray emission from pulsars is often detected as pulsed emission as well, with identical

timing characteristics P and $\dot{P}$ as the radio emission. However, in contrast to radio observations, individual pulsations are not detectable, as the γ-ray flux is orders of magnitude lower than the radio emission. To observe pulsations from long term γ-ray observations, the γ rays are assigned a phase value between [0,1] corresponding to the fraction of the period from the start of the radio pulsations. For the vast majority of pulsars, the periodic radio and γ-ray peaks do not line up, with some notable exceptions like the Crab pulsar (Du et al., 2012). Finally, the γ-ray emission is relatively constant in flux and spectrum, showing little variation on the time scale of days.

Several models for pulsed emission in γ rays from the pulsar magnetosphere have been proposed, including pair-cascade emission at the polar caps of the magnetic field (*polar cap* Ruderman & Sutherland, 1975; Sturrock, 1971) and e^+e^- radiation between the null-charge line $\vec{B} \cdot \vec{\Omega}$ and the light cylinder, the co-rotating radius which would travel at the speed of light (*outer gap* Romani & Yadigaroglu, 1995; Venter et al., 2012). Recent observations of the Vela pulsar tend to favor the *outer gap* models (Johnson et al., 2009). Since the light cylinder is quite small on astrophysical scales ($10^2 - 10^5$ km), pulsars cannot be spatially resolved in γ rays.

2.2.2 Active Galactic Nuclei

Many galaxies show evidence of significant non-thermal emission from the accretion of matter onto the central super-massive black hole. The standard model for the accretion process centers around the creation of jets of relativistic charged particles, showing signatures of synchrotron and inverse Compton radiation and cosmic-ray accleration. The orientation of the jet with respect to the line of sight determines the primary classification of the active galaxies. Significant γ-ray emission from the active galaxy is seen when viewed down the axis of the jet, most likely from the inverse Compton emission from relativistic electrons. Active galaxies with this orientation are classified as *blazars* and can be divided further based on the optical emission. The primary spectral model for blazars is radio to X-ray synchrotron at low energy and inverse Compton emission at high energy. Blazars can be divided into two general categories: Flat-Spectrum Radio Quasars (FSRQ) with a flat ra-

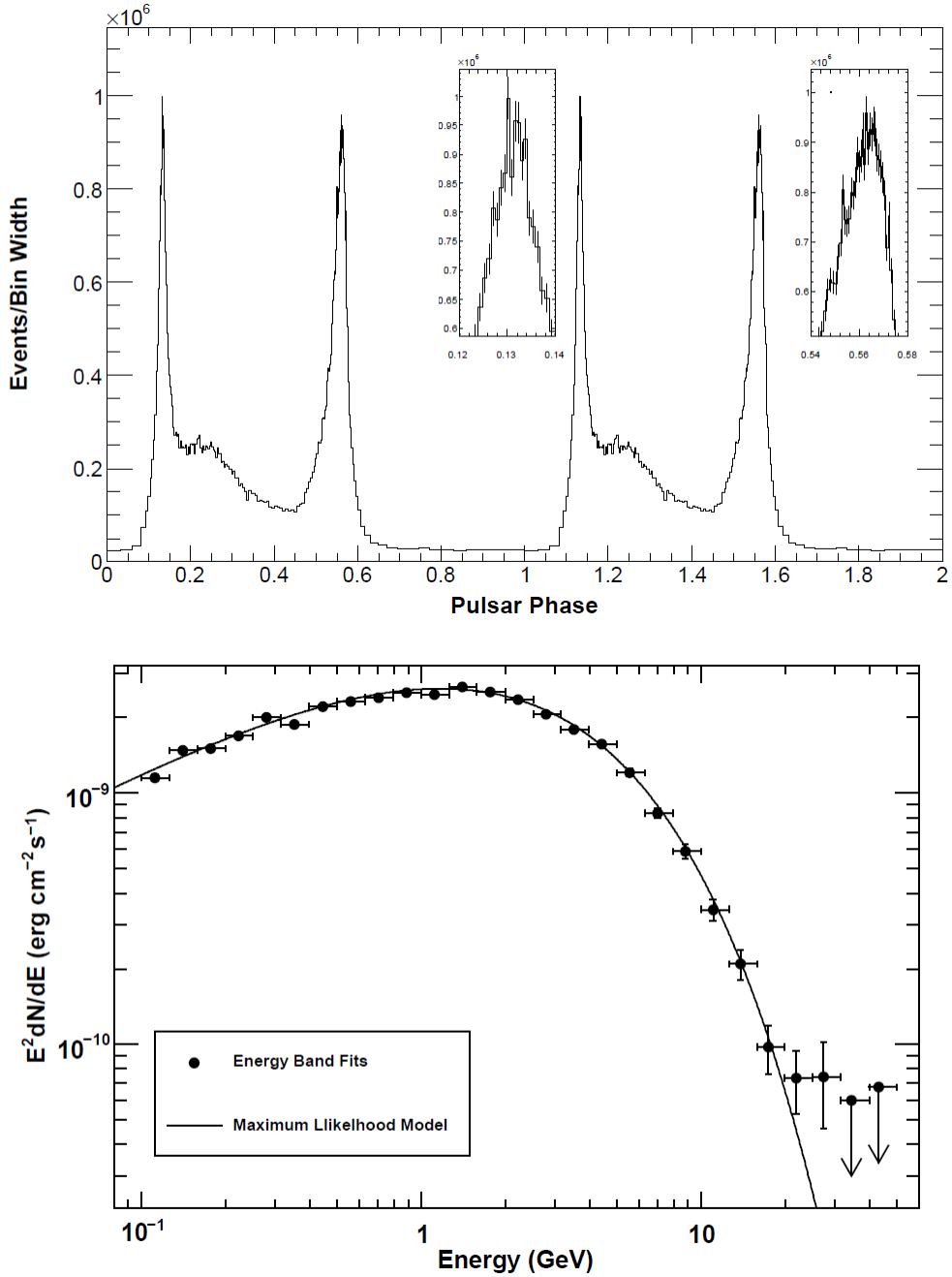

Figure 2.1 The histograms of the γ-ray phase values for the Vela pulsar (above) and the spectral energy distribution (SED, below) for the phase averaged spectrum for the Vela pulsar from Abdo et al. (2010e). The pulsar emission is effectively turned off between 0.7−1.0 of the pulse phase, making the pulsar emission separable from the background. The pulsar spectra are exponentially cut-off above a few GeV, with limited emission > 10 GeV.

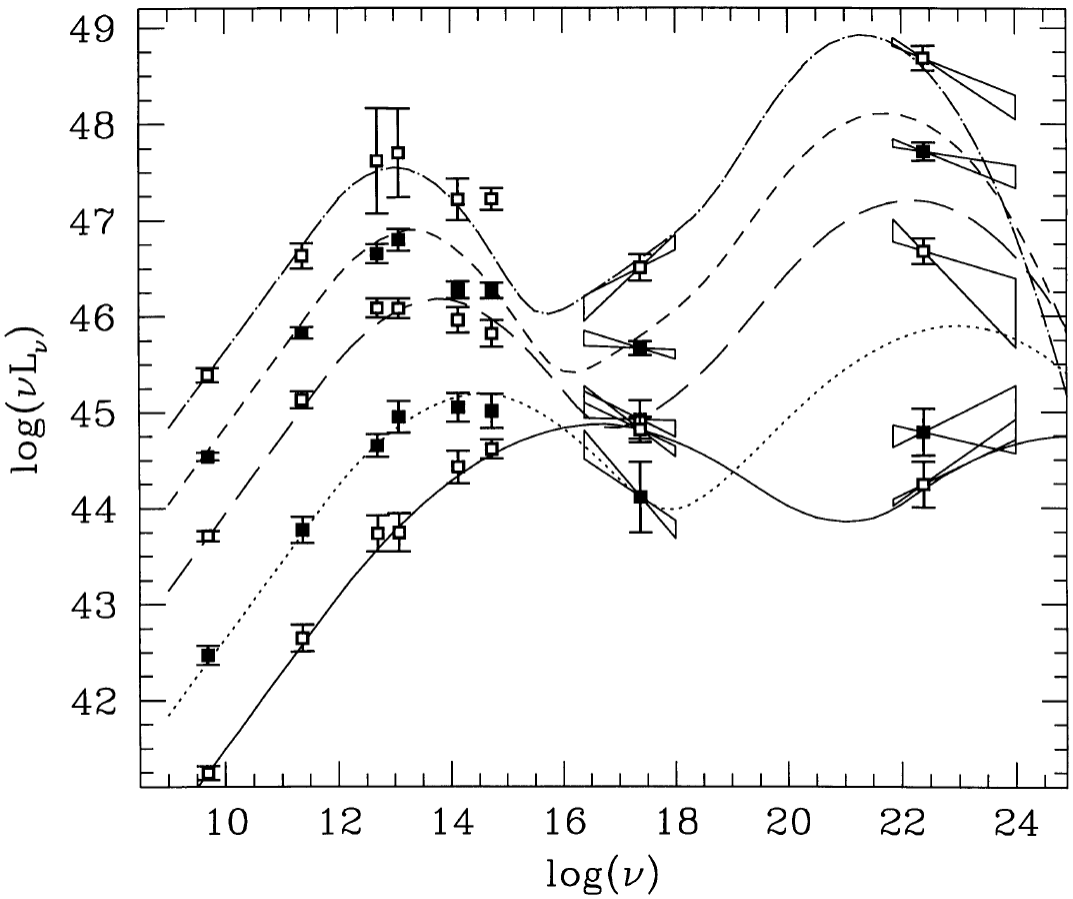

Figure 2.2 The broadband average spectral energy distribution (SED) of a set of 126 blazars from Fossati et al. (1998). The low energy peak ($10^{13} - 10^{17}$ Hz) corresponds to the peak in the synchrotron spectrum and the high energy peak ($10^{21} - 10^{25}$ Hz) corresponds to the inverse Compton peak.

dio spectrum and broad optical emission lines and BL Lacs with hard γ-ray emission and nearly featureless optical emission (Fossati et al., 1998). Blazars are also classified based on the location of the peak in the synchrotron spectrum as low (LSP), intermediate (ISP), and high synchrotron peak (HSP) blazars. Figure 2.3 shows the average spectral energy distributions (SED) for a set of 126 blazars into 5 categories based on the location of the synchrotron peak. In contrast to pulsars, AGN show both flux and spectral variability on the time scales of days and correlated in many wavebands.

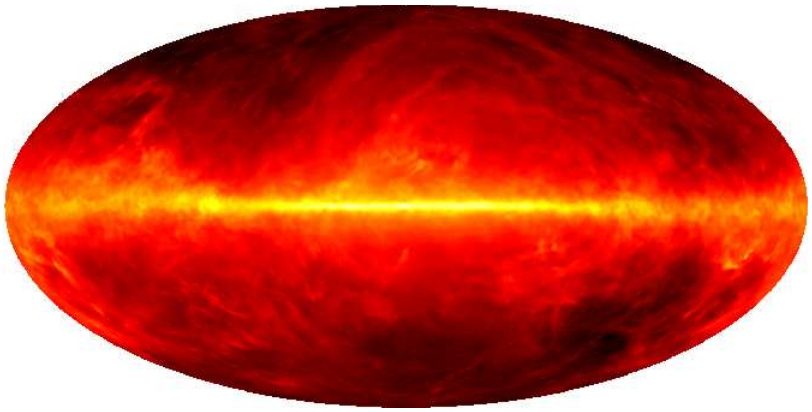

Figure 2.3 The *Fermi* model for diffuse Galactic emission at 1 GeV in an Aitoff projection centered at the Galactic center. The brightness at low galactic latitudes follows the matter distribution of the galactic disk. The diffuse emission at high latitudes comes mainly from local cosmic-ray interactions.

2.2.3 Diffuse Emission

In addition to the pulsar and AGN point sources, there is a hazy background of γ rays associated with the cosmic-ray interactions in the interstellar medium (ISM). γ rays are produced with nucleon interactions of cosmic-rays with the ISM, producing γ rays through the decay of neutral pions π_0. Cosmic-ray leptons produce γ rays through Bremsstrahlung interactions in the ISM and inverse Compton scattering off of the interstellar radiation fields (Tibaldo, 2010). The intensity of γ rays from these interactions traces the cold dust distributions in the Milky Way Galaxy, creating a bright band at low galactic latitudes from the galactic disk and highly structured background in all regions but the highest galactic latitudes. The *Fermi* model for the intensity of γ rays at 1 GeV is displayed in Figure 2.3.

2.2.4 Earth

The brightest persistent source of γ rays comes from the limb of the Earth, where cosmic-ray interactions in the atmosphere produce a bright band of γ rays. The emission is primarily produced in nucleon scattering, where neutral pions π^0 decay into two γ rays. The brightness of the limb is maximum at an angle of 113° from the zenith, decreasing significantly away

from the nadir (Abdo et al., 2009a). For lower energy protons and nuclei, the Earth's magnetic field significantly alters the cosmic-ray trajectories, resulting in a directional 'east-west' bias. The result is an intensity of γ rays with energy less than 10 GeV that is six times larger from the West than from the East.

2.3 Summary

In this chapter, we summarized the field of γ-ray astronomy, including the primary observatories and astrophysical sources. We characterized the primary limitations and efforts to construct observatories capable of detecting astrophysical sources. We identified the primary γ-ray production mechanisms, including cosmic-ray and leptonic-radiation interactions.

Chapter 3

Fermi Large-Area Telescope (LAT)

3.1 Systems

The LAT is the primary γ-ray instrument on-board the *Fermi* satellite, responsible for detecting and imaging γ rays with energy between $\sim$20 MeV to 300 GeV (Atwood et al., 2009). As we discussed in Section 2.1.1, the dominant process of the interaction of γ rays and matter above 20 MeV is pair-production and the LAT design is optimized for the creation and detection of the pairs. The LAT consists of a silicon tracker (TKR) with interleaved tungsten foils to promote pair conversion, a calorimeter (CAL) that provides energy measurement and assists the imaging process, and a segmented anti-coincidence detector (ACD) that rejects charged particle background and reduces the self-veto from showers in the CAL. In this section, we overview the properties of each of these systems and the orbital environment of the LAT.

3.1.1 Tracker

The LAT has 16 modules in a 4×4 array, each consisting of a tracker with 18 layers above a calorimeter. Each layer of the tracker consists of two trays of 384 silicon strips (36 cm $\times$ 56 μm) spaced 228 μm apart. The top tray is spaced 0.2 mm above the lower tray and the trays are oriented at 90°, with the top tray of the lower layer oriented with the bottom tray of the upper layer. The trays are oriented with either the sun facing (x) or the solar panel facing (y) directions of the LAT. The upper 12 layers of the tracker have 3% radiation length[1] (X_0) thick tungsten foils placed above the silicon trays to induce pair conversion.

[1]radiation length = 7/9 of the mean free path for photon pair conversion

The next 4 layers have 18% X_0 (0.072 cm) thick tungsten foils to increase the effective area ($A_{\rm eff}$) and the field of view[2] of the LAT. The spacing between each layer is 32 cm giving an angular resolution of 0.8° for a track between two layers.

The tracker design is a compromise between the need for limited multiple scattering for imaging (3% X_0 tungsten foil) and maximizing collection area (18% X_0 tungsten foil). The performance of these regions of the LAT is substantially different, so much so that the data from the events that convert in the thin (*front*) and thick (*back*) layers are treated separately in the *Fermi ScienceTools* analysis software[3]. At γ ray energies of $\sim$ 100 MeV, the multiple scattering process limits the imaging power of the LAT, while at energies above 1 GeV, the ratio between the instrument pitch and the track length in the detector is the limiting factor.

3.1.2 Calorimeter

The calorimeter (CAL) in each of the 16 modules consists of 96 CsI(Tl) crystal logs (2.7 cm $\times$ 2.0 cm $\times$ 32.6 cm) arranged in 8 horizontal layers of 12 logs (Grove & Johnson, 2010). For each layer in the CAL, the logs are oriented perpendicular to the layers above and below (hodoscopic configuration, e.g Carlson et al., 1996) and the depth of the CAL is 8.6 radiation lengths. The scintillation light generated from ionization energy deposited in the CAL logs is collected by large- and small-area photodiodes at each end of the logs, responsible for collecting light for low- (2 MeV to 1.6 GeV) and and high-energy (100 MeV to 70 GeV) deposition, respectively. The asymmetry between the light measured at each end of the CAL logs allows for reconstruction of the shower position within the log, giving the CAL imaging ability as well. The spatial orientation and structure of the energy deposition is particularly important at high energy, assisting the track reconstruction algorithms and removing background upward-propagating γ rays. The segmentation of the CAL into layers also aids in correction of the energy measurement for showers which leak outside of the LAT by modeling the propagation of the shower development in each layer.

[2]field of view $= \int A_{\rm eff}(\theta,\phi)d\Omega/A_{\rm eff}(0,0) \approx 2.4$ sr, where $A_{\rm eff}$ is the effective area of the LAT
[3]http://fermi.gsfc.nasa.gov/ssc/data/analysis/scitools/overview.html

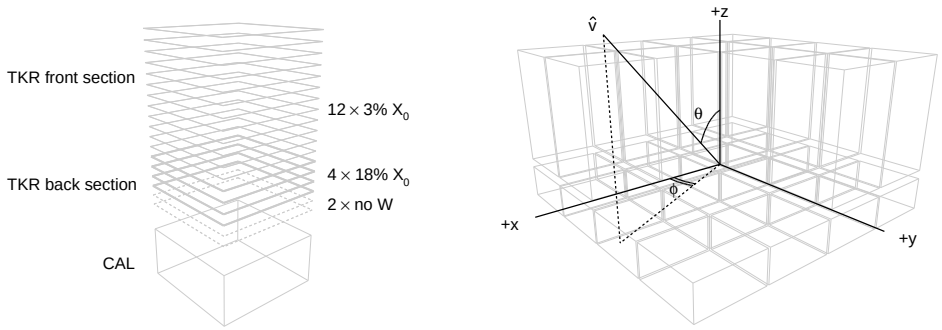

Figure 3.1 A single TKR/CAL module (left) and a cutout schematic of the LAT showing the layout of the 16 TKR/CAL modules (right). On the left diagram, the *front* TKR planes are indicated by the thin grey squares, the *back* planes are indicated by the thick grey squares, and the last two TKR layers with no tungsten with the dotted grey squares. The CAL is the cube below the TKR planes. On the right diagram, the coordinates of the LAT are defined including the inclination angle (θ) the angle from the boresight. The images are taken from a LAT performance paper in preparation.

3.1.3 Anti-coincidence Detector

In an environment where the vast majority of particles depositing energy in the LAT are not actually γ rays, the anti-coincidence detector (ACD) is crucial for identifying the charged particle background. The ACD must be very efficient, as the background intensity of charged particles is approximately 10^5 times larger than the γ-ray signal. The LAT ACD vetos background events with an efficiency of 99.97% for a single charged particle. However, the ACD is also crucial in removing internal backgrounds from interactions in the CAL. EGRET's ACD consisted of a single dome over its TKR and CAL, which was efficient at catching charged particles from outside, but above 10 GeV the detector had little effective area. The primary drawback in the single ACD design came from high energy showers in the CAL, where high energy photons were produced and Compton scattered in the ACD. To get around this issue of self-vetoing events, the LAT's ACD is segmented and the trigger is trained to only consider the ACD near the inferred γ-ray position. The ACD consists of thin plastic scintillator segments (1 cm $\times$ 100 cm^2) coupled to photo multiplier tubes (PMT) with wavelength shifting fiber (Moiseev et al., 2007). The tiles are overlapped to cover the entire LAT and protected with a thin micrometeorite shield. The combination of ACD and shield is only 0.06 X_0, thus limiting the conversion of events just outside TKR

and CAL.

3.2 Environment

Fermi was launched at Cape Canaveral, Florida on 11 June 2008 on a Delta II Heavy launch vehicle and orbits at an altitude of 565 km with a nearly circular orbit. The orbit has an inclination of 25.6°, reduced from the 28.5° at Cape Canaveral with a supplementary course correction on orbit. The orbit precesses with respect to the motion of the earth with a period of 53.4 days.

The spacecraft passes through the South Atlantic Anomaly (SAA), a region in the southern hemisphere containing geomagnetically trapped protons and electrons near the surface. The flux of charged particles in the SAA subjects the LAT to unsafe currents in the ACD, so the voltages in the PMTs are lowered to 45% of their nominal values and science data is no longer recorded. This results in a loss of observation time of approximately 17% (Abdo et al., 2009c).

The *Fermi*'s primary observation strategy is a 'rocking' mode, in which the LAT alternates between pointing toward the north and south orbital poles in successive orbits. At the beginning of the mission, the LAT 'rocked' between ±35° from the zenith towards the poles. With the LAT's large field of view (∼20% of the sky at 1 GeV), this strategy results in relatively uniform exposure of the entire sky over just a few orbits (∼ 3 hours). However, analysis of the LAT battery temperatures indicated the thermal radiators on the bottom of the craft were not effectively radiating away excess heat. The radiators required sufficient exposure away from the Earth to radiate properly and the 35° rocking angle was insufficient to facilitate this. In September 2009, the rocking angle was incrementally increased to 50°, alleviating this issue at the expense of over-emphasizing the LAT to the orbital poles. Additionally, the LAT may also be pointed at a particular location on the sky, either automatically or by program, where the LAT observes the location until it becomes occulted by the Earth. The time dependent and rocking angle exposure variation can be seen in Figure 3.2.

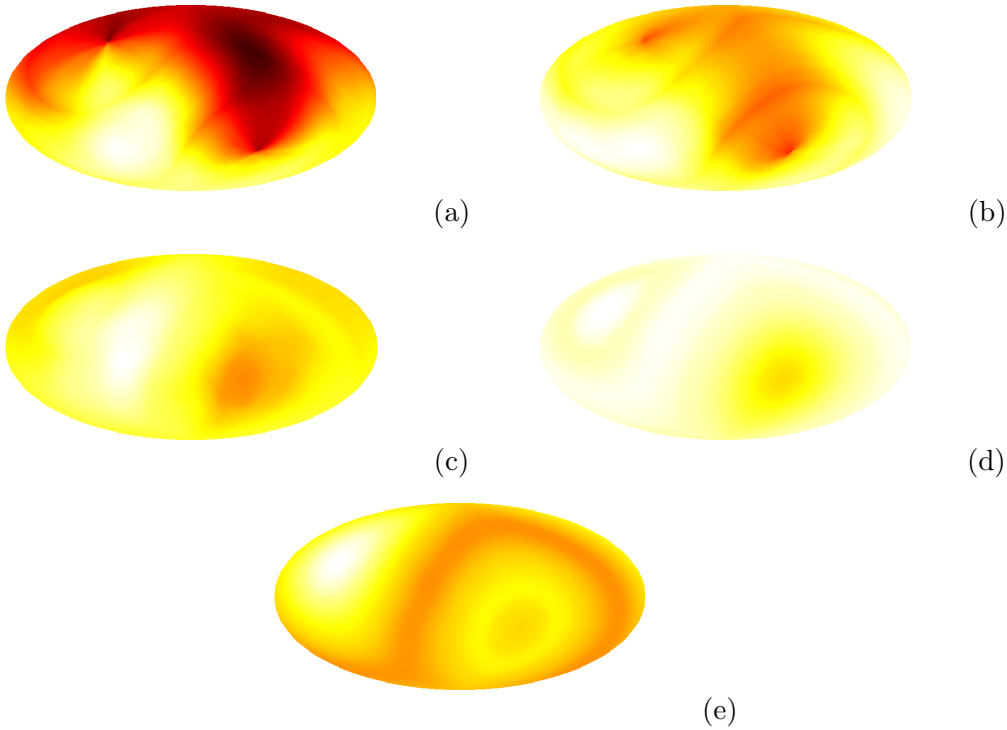

Figure 3.2 The exposure variation over the sky in galactic coordinates. The exposures (a)−(d) correspond to the initial 35° rocking angle profile of the LAT for (a) 3 hours ($\sim$ 2 orbits), (b) 1 day, (c) 1 month, and (d) 1 year. Figure (e) is also a 1 year exposure, but for the 50° rocking angle profile. In (e) the orbital poles are over-exposed compared to the 35° rocking angle profile.

3.3 Triggering and Reconstruction

The primary event trigger on-board the LAT is the so called '3-in-a-row' trigger, which begins when 3 successive TKR layers in a single tower are above the threshold for an ionizing particle within the trigger window. If this condition is satisfied (or any CAL crystal goes above threshold), the on-board systems trigger a readout of all modules. The readout time per event is 26.5 μs at the minimum, with the majority of the deadtime deriving from sending the event information to the LAT's on-board event processing. The readout time becomes appreciable to the background rate, introducing a rate-dependent livetime, which we will discuss in the next section. The event rates for different stages of cuts can be seen in Figure 3.3. Events that pass the requirements of the on-board filter are then downlinked through the Tracking and Data Relay Satellite System (TDRSS), a set of nine satellites and a handful of ground stations operating on a Ku-band receiver.

The data is then transported to the Stanford Linear Accelerator (SLAC) facility, where the event analysis begins. The GLast Event Analysis Machine (GLEAM) (Boinee et al., 2003) ingests the instrument data and calibration information, including the orientation and inter- and intra-alignment of the modules. GLEAM reconstructs the events based on simulations of the instrument, the details of which will be outlined in later Chapters.

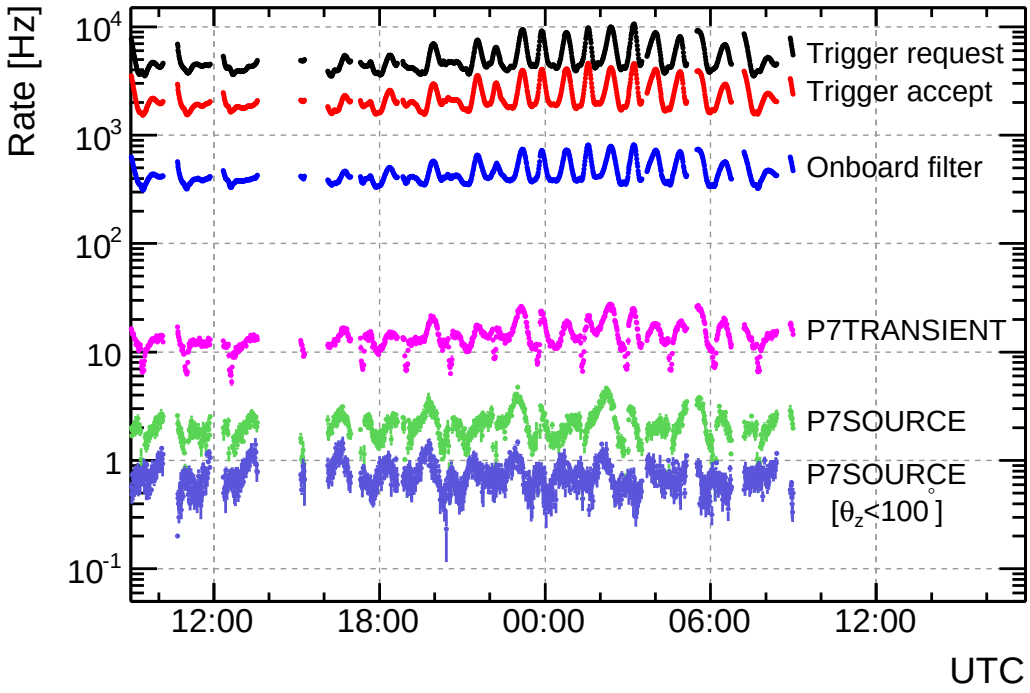

Figure 3.3 Rates at several stages of the data acquisition and reduction process on a typical day (2011 August 17) from a LAT performance paper in preparation. Starting from the highest, the curves shown are for the rates: (i) at the input of the hardware trigger process, (ii) at output of the hardware trigger, (iii) at the output of the on-board filter, (iv) after the classification of all good reconstructed events (`P7TRANSIENT` γ-ray), (v) after the primary selection on γ rays (`P7SOURCE` γ-ray), and (vi) the `P7SOURCE` γ-ray selection with an additional cut on the zenith angle ($\theta_z < 100°$, to remove the Earth's contamination).

3.4 LAT data

In contrast to imaging or pixel-based telescopes, the LAT does not report the intensity of γ rays from a location on the sky, but rather provides a separate analysis of each event recorded by the LAT. For analysis of the performance of each subsystem on the LAT, the Instrument

Table 3.1. The definition of the common parameters in the *Fermi* data products: γ ray data (*FT1*) and spacecraft data (*FT2*). The rows of *FT1* correspond to each event, while the rows *FT2* are for each Good Time Interval (GTI) of 30 seconds of observation. The 30 second GTI for the *FT2* allows for smooth interpolation of the spacecraft pointing data.

File	Parameter	Description
FT1	ENERGY	γ-ray energy in MeV
	RA,DEC	Right Ascension (α) and Declination (δ) of the γ ray (J2000)
	L,B	Galactic longitude and Latitude
	THETA,PHI	Direction of γ ray in LAT in polar coordinates
	ZENITH_ANGLE,AZIMUTH_ANGLE	Direction of γ ray in Earth polar coordinates
	TIME	Seconds of the event from Jan. 1 2001, 00:00:00 UTC (MET)
	CONVERSION_TYPE	Region of LAT γ ray converted in (*front* or *back*)
	EVENT_CLASS	Event classification (background vs. γ ray)
FT2	START,STOP	Beginning and end of the Good Time Interval (GTI) in MET
	SC_POSITION, LAT_GEO/LON_GEO	Spacecraft position in inertial and earth coordinates
	RAD_GEO	Spacecraft altitude
	RA_/DEC_ZENITH	(α,δ) of the zenith
	RA_/DEC_SCZ,RA_/DEC_SCX	(α,δ) of the z and x axis of the spacecraft
	LIVETIME	Seconds during the GTI when the LAT available to take data

Science Operations Center[4] (ISOC) provides the *Fermi* collaboration with ROOT[5] n-tuple data files with approximately 200 variables. Each of these variables corresponds to the output from the GLEAM analysis and is a summary of the digitization and reconstruction steps. The majority of the variables are not necessary for most sky-analysis, so the Fermi Science Support Center[6] (FSSC) provides two data products to reduce the overhead. The first is the *FT1* data file, containing the best estimates for the γ-ray parameters in Table 3.1. The second is the *FT2* data file, containing the spacecraft pointing and orbital information with the parameters defined in Table 3.1. Both files are stored in the FITS[7] table file format, a protocol for storing tabular and image data, and available from the FSSC data server[8].

3.5 Summary

We described the systems of the LAT telescope including the precision TKR and CAL for imaging γ rays and measuring energy and the ACD for rejecting charged particle back-

[4]http://glast-isoc.slac.stanford.edu/
[5]http://root.cern.ch/drupal/
[6]http://fermi.gsfc.nasa.gov/ssc/
[7]http://fits.gsfc.nasa.gov/
[8]http://fermi.gsfc.nasa.gov/cgi-bin/ssc/LAT/LATDataQuery.cgi

ground. We characterized the orbital environment of *Fermi* and the observation strategies of the LAT. We gave an overview of the data flow, from the trigger to the user, and a list of the common observables useful for analysis.

Chapter 4

Instrument Performance

As discussed in Chapter 3, the LAT is pair-conversion telescope utilizing tungsten layers of two thicknesses to convert γ rays into e^+e^- pairs. Since the LAT was designed as an imaging instrument, the ability to accurately reconstruct the direction of incident γ rays is crucial to the overall performance. The intrinsic limitations of the LAT's imaging are constrained by both the primary and secondary processes involved in the measurement of the γ ray directions; namely the conversion of the γ rays in the tungsten and traversal of the e^+e^- pairs through the material in the LAT. Furthermore, the large field of view, multiple conversion layers, and large energy range creates a rich variation in shower geometry and by extension, angular resolution. In the following section, we discuss the physical processes involved in the reconstruction of γ rays in the LAT and the simulation and validation of the instrument performance.

4.1 Instrument Response Functions (IRFs)

Due to time constraints in the construction of the LAT, only a fraction of the LAT's γ-ray energy sensitivity and performance was accessible by beam testing, so the LAT's response to γ rays and background (cosmic rays and albedo γ rays) has been simulated through Monte Carlo (MC). The MC simulates the LAT at all stages: the interactions of particles in the LAT (Geant4, Allison et al., 2006), the simulation of the LAT's digitization of the particle interactions and event reconstruction (GLEAM), and finally the simulation of the LAT's trigger and on-board filter (Atwood et al., 2009). Events that pass through these steps are then classified based on the likely particle type using a series of classification

Table 4.1. The energies of the particles in the beam test of the LAT Calibration Unit (CU). The data were taken at the CERN Proton Synchrotron (PS) and Super Proton Synchrotron (SPS) beams over a wide range of CU orientations (Baldini et al., 2007).

Particle	Events	Energy (GeV)	Beam
γ^1	4.0M	$0.05 - 1.5$	PS
γ^2	12.0M	$0 - 2.5$	PS
e^-	6.4M	$1, 5$	PS
e^-	17.8M	$10, 20, 50, 100, 200, 280$	SPS
e^+	2.5M	1	PS
p	19.0M	$6, 10$	PS
p	0.8M	$20, 100$	SPS
π^-	0.6M	5	PS
π^-	1.6M	20	SPS

[1]Independent energy measurement by photon tagging system.

[2]No independent energy measurement.

trees into a set of event classes. The event classes are defined by the acceptable level of background in the sample and the quality of the event reconstruction, ranging from all reconstructed particles to ultra-pure sets of γ rays. These simulations were then compared with a performance test of a LAT Calibration Unit (CU) consisting of two complete TKR and three CAL modules. The performance test consisted of several different beams of particles $(\gamma, e^{\pm}, p, \pi^-)$ at energies comparable to the LAT sensitivity (see Table 4.1) to simulate the on-orbit background interactions in the LAT (Baldini et al., 2007). In general, there was good agreement between MC simulations and performance of the LAT CU: the TKR reconstruction performance, the predicted backsplash of charged particles in the ACD, and the hadronic model of Geant4 for the background beam interactions.

The MC calibration sets for event classes are used to define the corresponding sets of LAT instrument response functions (IRFs): the point-spread function (PSF), the effective area (A_{eff}), and the energy dispersion (ED). The calibration sets, or the *allGamma* MC samples, are generated uniformly in $\log(E)$ and Ω and contain 400 million γ rays between $\log_{10}(E/100\text{ MeV})$ of 1.25 to 2.75 and 200 million between 2.75 to 5.75. The polar angle Ω is constrained to be downward-going, so only 2π of the total solid angle is simulated.

4.2 PSF

The PSF is the distribution of the angle between the true and reconstructed direction of γ rays. The LAT PSF depends primarily on four variables: the energy of the primary γ ray E, the incoming γ-ray direction $\hat{r}$, the conversion plane C, and the event selection s. The event selection s represents the cuts applied to the raw data to meet the requirements of the corresponding event classes. The γ rays that convert in the top, thin tungsten conversion planes C have longer track lengths in the detector and less material for multiple scattering. The consequences are dramatic at all energies, as the thin conversion planes have an angular distribution for reconstructed γ rays that is narrower by a factor of two. The *Fermi* ScienceTools distributes different PSF definitions for the thin and thick regions of the LAT, which are defined as *front* and *back*, respectively. The geometry of the LAT introduces a dependence of the incoming γ-ray direction $\hat{r}$, as the LAT PSF depends on the amount of material the converted pairs traverse in the TKR and CAL. The qualitative effect on the PSF is a broadening of the angular distributions at large angles with respect to the boresight, or the inclination angle. Finally, the strongest dependence of the PSF is on the energy of the primary γ ray E. At low energies (<10 GeV), the angular dispersion of converted pairs is dominated by multiple scattering and has the form $\sim 1/E$. At high energies (>3 GeV), the PSF depends on the ratio of the pitch (distance between centers of adjacent silicon strips) of the TKR to the length of the pair's track, which is constant with E. To simplify the PSF representation, we make two assumptions of the PSF with respect to $\hat{r}$: 1) the distribution of the reconstructed γ ray directions $\hat{r}'$ is azimuthally symmetric about $\hat{r}$ and 2) the PSF only depends on the inclination angle (θ-component of $\hat{r}$), implying the LAT PSF is symmetric about the boresight. Since the angular resolution of the LAT is at worst $\sim 20°$, we implement criterion 1) from above and the small angle approximation in the following way

$$\int f(\Omega)d\Omega = \int_0^{\pi}\int_0^{2\pi} f(\delta)\ d\phi\ d(\cos\delta) \approx 2\pi\int_0^{\infty} f(\delta)\ d\left(\frac{\delta^2}{2}\right) = 2\pi\int_0^{\infty} f(\delta)\delta d\delta \qquad (4.1)$$

where f is a normalized function of the angle between $\hat{r}$ and $\hat{r}'$, δ.

The angular distribution for multiple scattering is a random walk through material and follows the normal distribution in the limit of a large number of scatterings. However, when the LAT TKR misses the first hit after conversion, the penalty in the reconstruction of γ-ray directions is a distribution with an extended tail component (Atwood et al., 2009). Above 1 GeV, particle backsplash from the pairs interacting with the CAL and hard scattering processes such as bremsstrahlung limit the γ-ray reconstruction in the TKR. In this regime, the moments of energy deposition in the CAL constrain the search cone for the primary converted pair tracks (Atwood et al., 2009). While the CAL-enhanced searches improve the overall reconstruction of $\hat{r}'$, there are substantial tails in the angular distributions in this energy range. To account for the effect of extended tails in our functional representation of the PSF, we use the King function to model the angular distribution of $\hat{r}'$ about $\hat{r}$ (Read et al., 2011). The King function is defined as

$$K\left(\delta \mid \sigma, \gamma\right) = \frac{1}{2\pi\sigma^2}\left(1 - \frac{1}{\gamma}\right)\left(1 + \frac{\delta^2}{2\sigma^2}\frac{1}{\gamma}\right)^{-\gamma} \tag{4.2}$$

where δ is the angle between the $\hat{r}'$ and $\hat{r}$. σ determines the overall width of the distribution, while γ determines the significance of the tails of the distribution. The King function has the limiting property of

$$\lim_{\gamma\to\infty} K(\delta \mid \sigma, \gamma) \;\rightarrow\; N(\delta \mid \sigma) \tag{4.3}$$

where $N(\delta \mid \sigma) = \frac{1}{2\pi\sigma^2}\exp\left(-\frac{\delta^2}{2\sigma^2}\right)$ is the 2-dimensional symmetric normal distribution centered at the origin with a variance σ. The typical values of γ are between 1.5 and 3 for the fits to the LAT angular distributions, indicating the presence of large tail components. The prominence of the tails (and by proxy γ) is largely dependent on the energy, qualitatively increasing with energy.

When comparing the King function form of the PSF to model independent representations, it is often useful to define the containment radii R_F of the PSF

$$R_F : F = \int_0^{R_F} f(\delta)\delta d\delta \tag{4.4}$$

where F is the percentage of the distribution contained between 0 and R_F. Since there are two degrees of freedom in the single King function, two containment radii are necessary to completely characterize σ and γ. We adopt the convention of the 1σ and 2σ containments of a 1D normal distribution, using the 68 and 95% containment radii R_{68} and R_{95} to characterize the model independent PSF. In comparison to the 1D normal distribution, the 68 and 95% containment correspond to 1.51σ and 2.44σ for a 2D normal distribution. For a single King function, R_F can be calculated analytically

$$R_F(K) = \sigma\sqrt{2\gamma}\sqrt{(1-F)^{\frac{1}{-\gamma+1}} - 1} \tag{4.5}$$

which, for the 'characteristic' value of $\gamma = 2.25$ for the PSF, yields $R_{68} \approx 2.6\sigma$ and $R_{95} \approx 6.7\sigma$.

While both σ and γ depend on energy in principle, σ is more strongly tied to the magnitude of the multiple scattering at low energy and the pitch/track length ratio at high energy. The $1/E$ dependence of the angular size of the multiple scattering is by far the largest energy dependence of any process, so we define a function $S_P(E)$ which accounts for the energy dependence of σ. It is defined such that the peak of the distribution $K(\delta \mid \sigma, \gamma) \times \delta$ occurs when $\delta = \sqrt{2}\ S_P(E)$. We chose a functional form of $S_P(E)$ that summed the multiple scattering and pitch/track length components in quadrature

$$S_P(E \mid c_0, \beta, c_1) = \sqrt{\left[c_0 \cdot \left(\frac{E}{100\ \mathrm{MeV}}\right)^{-\beta}\right] + c_1^2} \tag{4.6}$$

where c_0 corresponds to R_{68} at $\sim$170 MeV, c_1 is the pitch/track length angle, and β is the multiple scattering power law. Since the tails of the angular distribution increase above 1 GeV, β is typically < 1 with a 'characteristic' value of $\beta \approx 0.8$. The parameters for $S_P(E)$ from a simulation of the LAT performance are displayed in Table 4.2 for both *front*- and *back*-converting γ rays.

As noted by Kerr (2011), the fractional differences of a single King function to the distributions can be as large as 20% near R_{68}, albeit much smaller than the residuals for a fit to a normal distribution. To account for these residuals, some representations of the PSF use

Table 4.2. The parameters of the scale function $S_P(E \mid c_0, \beta, c_1)$ for the σ parameter from a simulation of the LAT performance. The parameters are divided into their respective conversion regions: *front* and *back*.

Conversion Type	$c_0[^\circ]$	$c_1[^\circ]$	β
front	3.32	0.022	0.80
back	5.50	0.074	0.80

the sum of two King functions: *core*, which is most significant for small δ, and *tail*, which is most significant in the tails of the angular distribution. The two King function form can be expressed as

$$K_2(\delta \mid f_c, \sigma_c, \gamma_c, \sigma_t, \gamma_t) = f_c \; K(\delta \mid \sigma_c, \gamma_c) + (1 - f_c) \; K(\delta \mid \sigma_t, \gamma_t) \tag{4.7}$$

where the subscript c and t denote the *core* and *tail* components, respectively. The relative normalization is controlled by f_c, the fraction of the distribution described by the *core* King function. While this form matches the distributions of δ much better in general, there is no analytic functional form for the containment R_F in terms of the two King function parameters. Thus, any containment radii quoted for K_2 function will have been computed numerically. A sample distribution from a simulation of the LAT performance is plotted in Figure 4.1, with normal distribution (Gaussian), single King function, and double King function fit to the δ distribution.

4.3 Effective Area

The A_{eff} is the product of pair-conversion probability with the geometric collection area including reconstruction and background rejection efficiency (s) and depends on $\hat{r}$. The A_{eff} as a function of energy and polar angles can be calculated from the ratio of the number of events $n(E_i, \theta_j, \phi_k)$ which pass the criteria s to the total number of events N_{gen}

$$A_{\text{eff}}(E_i, \theta_j, \phi_k) = 6 \text{ m}^2 \times \frac{n(E_i, \theta_j, \phi_k)}{N_{\text{gen}}} \times \frac{\Delta\Omega_{jk}}{2\pi} \frac{\log(E_i)}{\Delta E_i}. \tag{4.8}$$

where E_i is the center of the ith energy bin, ΔE_i is the width of the ith energy bin, θ_i and ϕ_k are the centers of the polar angles, and $\Delta\Omega_{jk}$ is the solid angle subtended by the angular bin centered on (θ_i,ϕ_k) (Abdo et al., 2012 in prep.). The factor of 6 m^2 is the cross sectional area of the sphere where the γ rays are simulated, which covers the LAT and the majority of the spacecraft. Like the PSF, the ϕ-dependence of the $A_{\rm eff}$ is generally small enough to ignore for most analyses, so we sum Equation 4.8 over k

$$A_{\rm eff}(E_i, \theta_j) = 6 \text{ m}^2 \times \frac{n(E_i, \theta_j)}{N_{\rm gen}} \times \Delta\theta_j \frac{\log(E_i)}{\Delta E_i} \tag{4.9}$$

The minimum energy for the effective area is approximately 30−50 MeV depending on the event class selection and increases roughly linearly until 1 GeV, where it remains relatively flat past 100 GeV. The effective area is maximum along the boresight axis at all energies and decreases linearly with inclination angle until it reaches its minimum of zero at $\theta \approx 72-75°$ or $\cos(\theta) \approx 0.25$. The *front* conversion class has a slightly larger $A_{\rm eff}$ than *back* (roughly 20% at all energies), while the *back* has more $A_{\rm eff}$ at high inclination angles (roughly 3 times larger near $\theta = 70°$).

We found additional effects on the $A_{\rm eff}$ from analysis of on-orbit data, involving loss of effective area, and simulated their effects in the MC. Energy deposition in the TKR, CAL, and ACD from charged particles that traversed the LAT a few μs before an event was recorded caused a significant number of events to be misclassified or rejected. These 'ghost' tracks resulted in a net loss of about 10% of the $A_{\rm eff}$, with the largest loss of 20% near 1 GeV. The *front* and *back* $A_{\rm eff}$ from the `Pass6` event class reconstruction for the `Pass6` pre-launch IRF are plotted in Figure 4.2. An example of an event with 'ghost' activity can be seen in Figure 4.3.

4.4 Energy Dispersion

The energy reconstruction of the LAT involves both TKR and CAL data. The process begins with an initial estimate of the energy based on the sum of the energies in the CAL crystals. The analysis then computes the most likely direction for the converted pair's trajectory

based on the spatial structure of the energy deposition in the CAL (energy moments). For trajectories that traverse LAT tower boundaries, including the sides and back of the CAL, the algorithm calculates expected losses in these regions as corrections to the energy. The spatial structure of the energy deposition (energy moments) is crucial for seeding the TKR Kalman filter pattern recognition, as the tracks are constrained to fit in a cone defined by the best estimate of the shower development direction.

The energy dispersion is the PDF of the difference between the true energy E of the γ ray in the MC simulation versus the best estimate by the event reconstruction E' and depends only on s. We found that the LAT has a small bias to reconstruct the energy of the γ ray slightly below its true energy. Like the PSF, the energy dispersion has a well defined core and long tails, but unlike the PSF, has a very weak energy dependence. The 68% containment of energy dispersion as a function of energy is roughly parabolic, maximized at low and high energy (<100 MeV and >100 GeV) and minimized in the mid-energy range of the LAT ($3 - 12$ GeV), varying between $5 - 15\%$ at the extremum. For long term source analysis of the purer γ-ray samples, the tails of the energy dispersion are removed significantly to improve data quality, limiting the influence of dispersion on the source flux. We will ignore dispersion in the following sections, as accounting for it is computationally intensive and has a negligible effect in the determination of the PSF and the majority of source analysis.

4.5 Summary

In the this chapter, we have described both the simulation of the LAT and the performance of the CU. We presented the IRFs that characterize the MC performance of the LAT and the event reconstruction in terms of angular dispersion (PSF), energy dispersion (ED), and effective area (A_{eff}). We found that performance of the CU in beam tests closely matched the MC simulation over the limited energy range of the real events. Since the launch of the LAT, we determined there were events with 'ghost' tracks that negatively affected event reconstruction and classification, leading to a loss of effective area. In the next section, we will determine the performance of the LAT PSF on-orbit and compare the PSF to the MC

simulations.

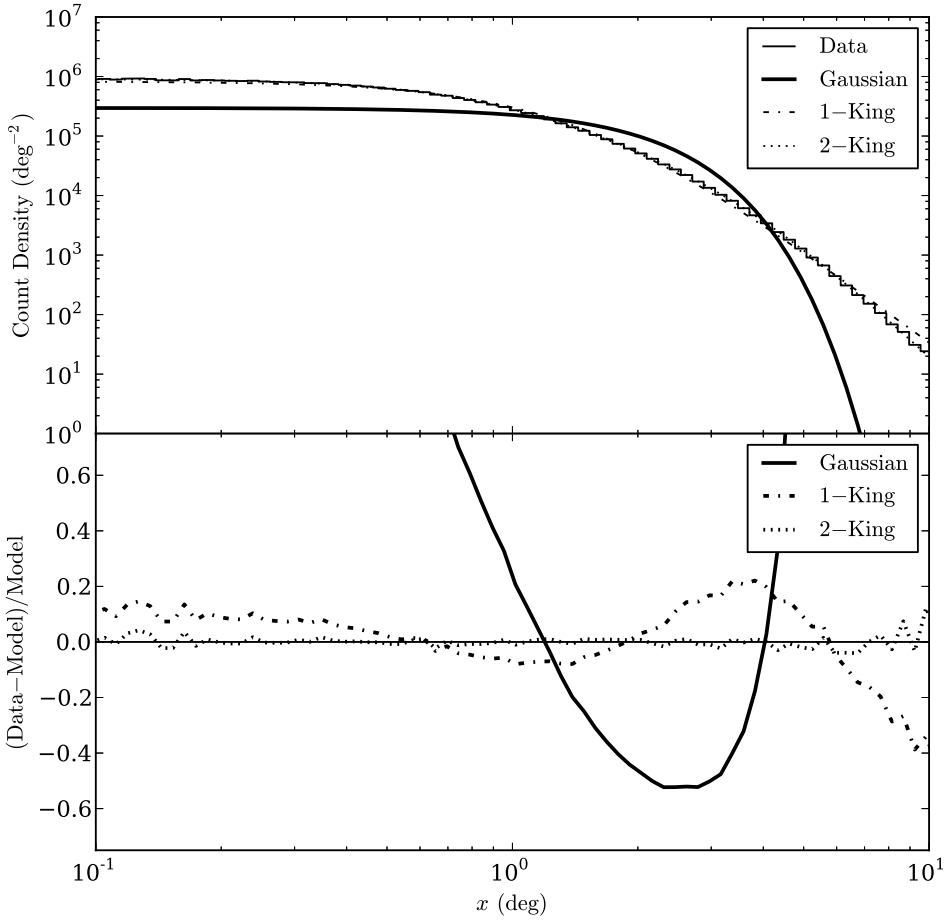

Figure 4.1 Comparison of best-fit Gaussian, single, and double King function fits to a MC angular distribution of *Diffuse* event class γ-rays histogram with energy of 7.5 GeV impinging at inclination angles between 26 and 37° uniformly in solid angle. The best-fit Gaussian, determined by binned likelihood, gives a poor representation of the PSF at small and large separations because of power-law tails at large angles.

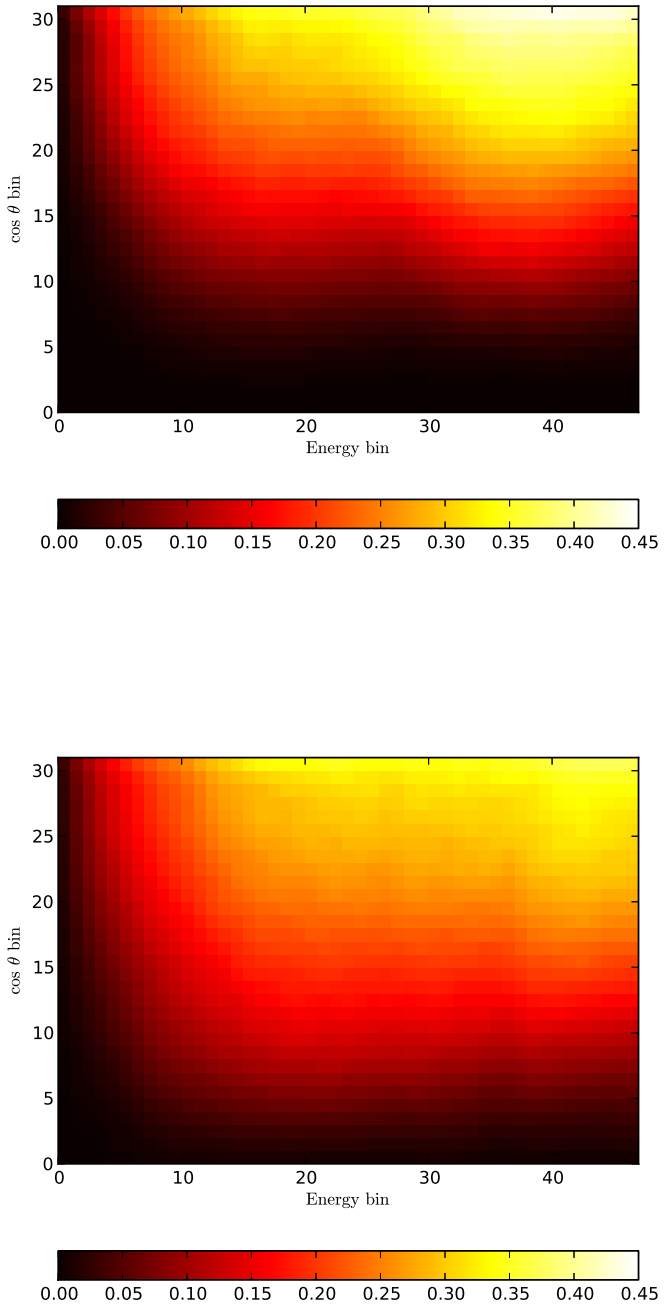

Figure 4.2 Comparison between the *front* (left) and *back* (right) effective area for the `P6_V3` IRF. The energy bins are logarithmically spaced between 17 MeV and 562 GeV, while the $\cos\theta$ bins are spaced linearly between 0.2 (off-axis) and 1.0 (on-axis).

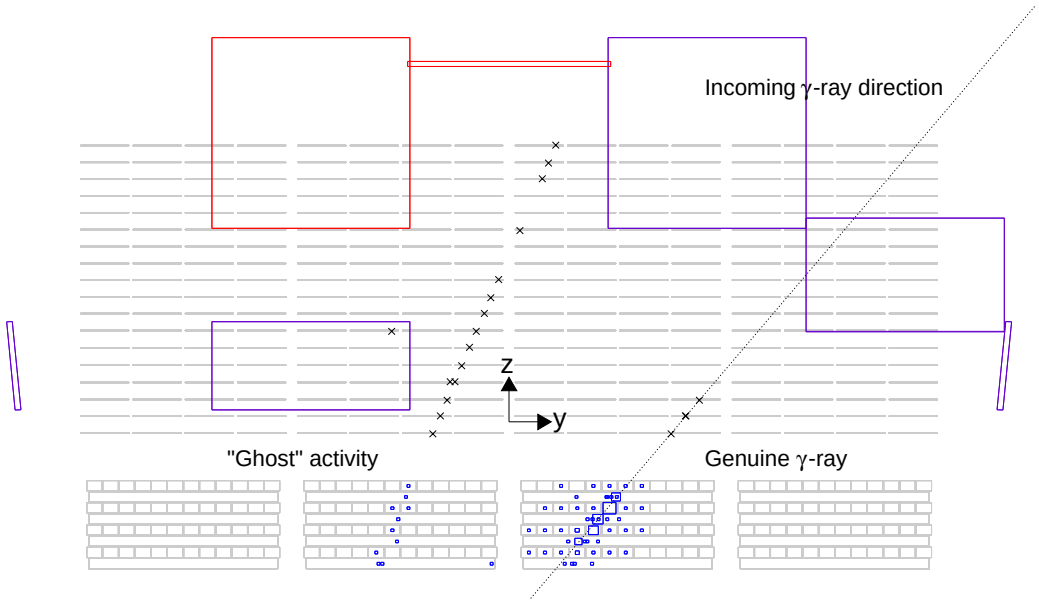

Figure 4.3 An example of a 'ghost' event taken from a LAT performance paper in preparation. The LAT is projected in the $y - z$ plane with the TKR planes (above), the CAL crystals (below) and the ACD tiles hit (large colored squares), The x's represent the consecutive hits in the TKR of a charged particle traversal. The size of the squares in the CAL correspond to the energy deposited and the dotted line corresponds to the γ-ray direction.

Chapter 5

Likelihood Analysis

As we noted earlier, the γ rays are stored as data on an event-by-event basis rather than an intensity from an area on the sky. The relatively large PSF at low energies makes it difficult to spatially resolve sources and extremely difficult in regions with significant diffuse Galactic emission. The variation in the LAT's performance over a single orbit requires separate analysis of each event. Photon counting telescope experiments, such as COS-B (Pollock et al., 1981, 1985), EGRET (Mattox et al., 1996), and *Fermi* use the method of maximum likelihood (Neyman & Pearson, 1928) to analyze data.

5.1 Maximum Likelihood

The method of maximum likelihood for parameter estimation can be defined as follows: given a set of measurements $\{x\}$ and a set of model parameters $\vec{\theta}$ for a PDF $g(x \mid \vec{\theta})$, the joint probability for the x_i to be between x_i and $x_i + dx_i$ given the parameters $\vec{\theta}$ is

$$P(\vec{\theta} \mid \{x\}) = \prod_i^N g(x_i \mid \vec{\theta})\ dx_i. \tag{5.1}$$

Discarding the dx_i, as they do not depend on the parameters, leaves the likelihood function

$$\mathcal{L}(\vec{\theta} \mid \{x\}) = \prod_i^N g(x_i \mid \vec{\theta}) \tag{5.2}$$

and the maximum likelihood estimates (MLE) for the parameters are given by

$$\vec{\theta}_0 : \mathcal{L}(\vec{\theta}_0 \mid \{x\}) = \sup[\mathcal{L}(\vec{\theta} \mid \{x\})]. \tag{5.3}$$

The MLE are normally distributed in the limit of a large number of counts from the central limit theorem and thus the likelihood function can be described by the d parameters and covariance matrix $\mathcal{C}$ near the maximum likelihood as

$$\mathcal{L}(\vec{\theta}_0 - \vec{\theta} \mid \{x\}) \approx \frac{1}{(2\pi)^{d/2} \det[\mathcal{C}^{-1}]^{1/2}} \exp\left[-\frac{1}{2}(\vec{\theta}_0 - \vec{\theta})^T \cdot \mathcal{C} \cdot (\vec{\theta}_0 - \vec{\theta})\right]. \tag{5.4}$$

For some analyses, we assume the total number N of γ rays observed is a Poisson distributed variable and we add a term to the likelihood function for a model of N_0 observed

$$\mathcal{L}(\vec{\theta}, \hat{N} \mid \{x\}) = \frac{\hat{N}^{-N}}{N!} \exp\left[-\hat{N}\right] \prod_i^N f(x_i \mid \vec{\theta}). \tag{5.5}$$

which is defined to be the extended likelihood function and generally has smaller MLE uncertainties than the likelihood function. For computational and statistical reasons, it is preferable to use the natural logarithm of the likelihood functions, as opposed to the likelihood functions themselves. Equation 5.4 becomes

$$\log \mathcal{L}(\vec{\theta} \mid \{x\}) \approx -\frac{1}{2}(\vec{\theta}_0 - \vec{\theta})^T \cdot \mathcal{C} \cdot (\vec{\theta}_0 - \vec{\theta}) \tag{5.6}$$

where constant terms in the log-likelihood are removed for clarity. If we take the second derivative of the log-likelihood with respect to any parameter, we find

$$-\frac{d^2 \log \mathcal{L}}{d\theta_i^2} \approx \mathcal{C}_{ii} = \sigma_i^{-2} \tag{5.7}$$

where σ_i is the uncertainty of the ith MLE. We adopt this method for error estimation for all MLE in this paper. For source analysis, we assume the γ rays we see are statistically independent and model the γ rays we observe as the superposition of PDFs

$$g(x \mid \vec{\theta}, \vec{\mu}) = \sum_j^n \mu_j \; f_j(x \mid \vec{\theta}) \tag{5.8}$$

where $\vec{f}$ and $\vec{\mu}$ are the model and the PDF fraction, respectively. The extended log-likelihood

then becomes

$$\begin{aligned}
\log \mathcal{L}(\vec{\theta}, \vec{\mu}, \hat{N} \mid \{x\}) &= -N \log(\hat{N}) - N_0 + \sum_i^N \log \left(\sum_j^n \mu_j \ f_j(x_i \mid \vec{\theta}) \right) \\
&= -\hat{N} + \sum_i^N \left[\log \left(\sum_j^n \mu_j \ f_j(x_i \mid \vec{\theta}) \right) + \log(\hat{N}) \right] \\
&= -\sum_j^N \hat{N}_j + \sum_i^N \log \left(\sum_j^n \hat{N}_j \ f_j(x_i \mid \vec{\theta}) \right)
\end{aligned} \tag{5.9}$$

where $\hat{N}_j = \hat{N}\mu_j$ is the estimated number of counts from the jth model. Finally, the log-likelihood has the following convenient property: if $\log \mathcal{L}_1$ is the maximum log-likelihood of the model with n free parameters and $\log \mathcal{L}_0$ is the maximum likelihood of the model with m free parameters (proper subset of the n parameters), the test-statistic $TS = -2(\log \mathcal{L}_1 - \log \mathcal{L}_0)$ will be distributed as

$$P(TS) = \chi^2_{n-m}(TS); \qquad n > m \tag{5.10}$$

where χ^2_n is the chi-square distribution with n degrees of freedom (Chernoff, 1954; Wilks, 1938). The TS will follow this distribution as long as the fixed parameters are not on the boundary of their possible values.

5.2 Likelihood Analysis of LAT Data

With the likelihood machinery in place, we now describe the application to LAT data. For likelihood analysis, we limit the observables to be $\{x\} = \left\{E, \hat{\Omega}, \hat{r}, t\right\}$: the observed energy of the γ ray, the observed position on the sky, the observed position in the detector, and the observation time. Given a set of γ rays, the general likelihood-based source analysis procedure is to model a region in terms of point sources $\vec{S}$ and backgrounds $\vec{B}$. We can then express the total model as

$$g(E, \hat{\Omega}, \hat{r}, t) = \sum_i^{\{S,B\}} \mu_i f_i(E, \hat{\Omega}, \hat{r}, t) \tag{5.11}$$

where the μ_i are the fraction of the source/background in the total model. The corresponding PDF for each model $f(E, \hat{\Omega}, \hat{r}, t) = d^6N/dEd\Omega drdt$ is, in general, quite complicated, as it requires a convolution over the 'true' set of variables $\{x'\} = \left\{E', \hat{\Omega}', \hat{r}', t'\right\}$. The first simplification from comes from the time and instrument coordinate integrals, we assume that this term is $\delta(t - t')\delta(\hat{r} - \hat{r}')$, i.e. we have perfect knowledge of the LAT coordinates and the observation time of the γ ray. We consider sources to be constant over the selected LAT observation window, even though they often have intrinsic variation which is time and energy dependent. We simplify the structure of the PDF further in the likelihood analyses and model f for the sources and background as

$$f(E, \hat{\Omega}, \hat{r}, t) = \int \mathcal{F}(E', \hat{\Omega}', t)\ P(E', \hat{\Omega}, \hat{\Omega}', \hat{r})\ A_{\text{eff}}(E', \hat{r})\ L_I(\hat{\Omega}, \hat{r})\ E_{disp}(E, E') d\Omega' dE' \quad (5.12)$$

which is separable into a flux term $\mathcal{F}(E', \hat{\Omega}, t)$ with units of cm^{-2} sr^{-1} s^{-1} and an instrument-dependent term $P(E', \hat{\Omega}, \hat{\Omega}', \hat{r}) \times A_{\text{eff}}(E', \hat{r}) \times L_I(\hat{\Omega}, \hat{r}) \times E_{disp}(E, E')$ with units of MeV^{-1} cm^2 sr^{-1}. The computational limitations of likelihood analysis are significant when the number of sources is $\sim$1000 and the number of γ rays is $\sim 10^7$, so for practical analyses we must integrate over a subset of the variables to reduce the dependencies.

As we noted in the previous section, the energy dispersion has a relatively minor effect on the spectrum of sources, so for our analyses we treat it as $E_{disp} = \delta(E - E')$. This makes the energy integral in Equation 5.12 trivial, replacing the true energy with the observed energy. The angular integral over $\mathcal{F}(E, \hat{\Omega}', t) \times P(E, \hat{\Omega}, \hat{\Omega}', \hat{r})$ represents the convolution of the spatial model of the source with the angular dispersion, or the PSF. This factor is simply the PSF for a point source $\left(\mathcal{F}(\hat{\Omega}) = \delta(\hat{\Omega} - \hat{\Omega}_s)\right)$; however, the spatial distribution of the Galactic diffuse background is highly structured and the convolution is non-trivial in this case.

The *ScienceTools* source likelihood analysis tool *gtlike* makes no further simplifications to the likelihood calculation in its unbinned mode, other than to specify the energy dependence of $\mathcal{F}$. There are a number of spectral models used for sources, the most common being a Power-law(PL), Exponential-cutoff(EC), Broken Power-law(BPL), and Log-parabola(LP)

which are expressed as

$$
\begin{aligned}
&\mathcal{F}(E) \propto E^{-\Gamma}; \quad \text{PL} \\
&\mathcal{F}(E) \propto E^{-\Gamma} \exp\left[-\frac{E}{E_c}\right]; \quad \text{EC} \\
&\begin{cases} \mathcal{F}(E) \propto E^{-\Gamma_1} & E < E_c \\ \mathcal{F}(E) \propto E^{-\Gamma_2} & E > E_c \end{cases}; \quad \text{BPL} \\
&\mathcal{F}(E) \propto E^{-\Gamma-\beta \log E}; \quad \text{LP}
\end{aligned}
\tag{5.13}
$$

and are representative of the spectral variety of γ-ray sources. The γ-ray emission of pulsars, such as Vela, follows the EC model with emission above the cutoff energy $E_c \approx 1 - 3$ GeV exponentially supressed. Some AGN such as the BL Lac MRK 421 can be characterized by a single PL with $\Gamma = 1.78 \pm 0.02$ (Abdo et al., 2011a), whereas the FSRQ 3C 454.3 has a spectral break at $E_c \approx 2$ GeV with Γ_1=2.31±0.02 and Γ_2=3.2 ± 0.12 with the BPL model (The Fermi-LAT collaboration, 2010). 3C 454.3 has also been analyzed with a LP spectral model, with best fit parameters $\Gamma = 2.52 \pm 0.03$ and $\beta = 0.11 \pm 0.02$ (The Fermi-LAT collaboration, 2010).

To test for the presence of sources with the spectral models given above, we use the log-likelihood calculation from Equation 5.9 and construct a TS with

$$
TS = -2\left(\log \mathcal{L}(\mu_s = \hat{\mu}_s) - \log \mathcal{L}(\mu_s = 0)\right) \tag{5.14}
$$

where μ_s is fraction of the source in the model and $\hat{\mu}_s$ is the MLE for this value. Thus, from Chernoff's theorem, $\sqrt{TS}$ corresponds to the significance in σ of the normal distribution for the source to be present with fraction $\hat{\mu}_s$ versus the null model ($\mu_s = 0$). This analysis is used to generate the parameters for each source in the catalogs produced by the *Fermi* collaboration (Abdo et al., 2010a,d; Ackermann et al., 2011b; Nolan et al., 2012).

Unfortunately, the unbinned mode of *gtlike* is still too computationally intensive for years of data without some prior knowledge of source properties. A separate source analysis program in Science Tools, *pointlike*, is used to seed the unbinned *gtlike* analysis. *pointlike*

makes two further simplifications to the likelihood calculation: 1) The data are binned in energy and location on the sky and 2) an average instrument response is used for long exposures with the assumption that the sky coverage averages out instrumental effects. The spectrum for all *Fermi* sources is monotonically decreasing with energy, often as a PL, so we utilize logarithmic spaced energy bins. In Figure 5.1, we compare the ratio of the mean energy to the geometric mean of the energy bin as a function of Γ in a PL spectrum and the number of bins per logarithmic decade. When at least four bins per logarithmic decade are used, the mean energy of the bin is within 5% of the geometric mean of the bin, effectively resolving spectral features between $\Gamma = 1 - 3$. The binning on the sky was accomplished with the HEALPix[1] pixelization scheme and outlined by Kerr (2011). The PSF is large at low energy and the number of γ rays is large, so large pixels are used to store the data. At high energy, the PSF is small and the number of γ rays is small and so the smallest pixels are used so that there is effectively single γ rays in each pixel. Finally, to limit the loss of angular resolution by the pixelization, the size of the pixels is 1/3 of the R_{68} of the PSF. This representation compresses the data effectively at low energy and preserves directional information at high energy where localization is most important. For observation periods longer than the orbital precession period of 53.4 days, the LAT covers the sky nearly uniformly in instrument coordinates, and *pointlike* calculates an effective instrument performance over the observation period. The simplifications reduce the likelihood calculation from the original 10^{13} calculations down to about 10^6 through binning and 10^3 through parallelization. The validation of the *pointlike* application is documented by Kerr (2011).

5.3 Summary

In this chapter, we characterized the method of maximum likelihood and the application to LAT data. We outlined the statistical test for assessing the significance of sources and the spectral models used to model the energy-dependent emission. We showed that in order to make the likelihood calculations tractable we must make a number of simplifications to the

[1] http://healpix.jpl.nasa.gov/

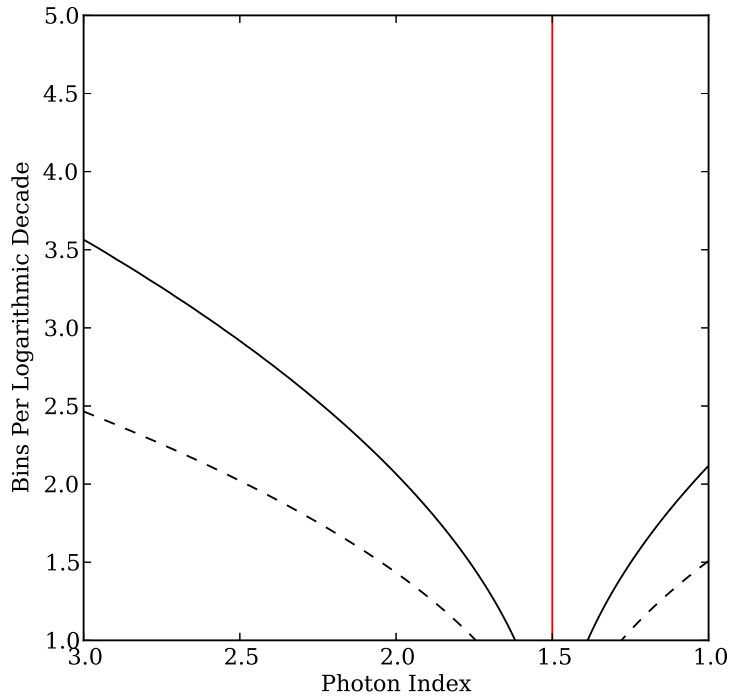

Figure 5.1 The contours for the ratio of the mean energy $\bar{E}$ of a bin to the geometric mean energy $E_g = \sqrt{E_{min}E_{max}}$ of the bin. The red line shows the relation $\bar{E} = E_g$ for sources with spectra that follow $E^{-3/2}$, the solid black line indicates the contour where $(\bar{E} - E_g)/\bar{E} = \pm 5\%$, and the dashed line indicates $\pm 10\%$.

source and background models. We described two likelihood analyses: *pointlike* for efficient calculation of the binned likelihood and *gtlike* which is less efficient but calculates the full likelihood.

Chapter 6

LAT Boresight Alignment

The reconstruction of γ-ray directions is computed with respect to the instrument coordinates. To convert the instrument coordinates at any given time to celestial coordinates, the LAT uses the Guidance, Navigation and Control system or the 'star tracker' (Abdo et al., 2009c). The star tracker consists of optical telescopes that recognize the star field patterns while on-orbit and determines the orientation of the spacecraft to within a few arcseconds. The star tracker was calibrated before the launch of the telescope, however several effects likely influence the relative orientation of the spacecraft and LAT on-orbit. Thermal variations, acoustic vibrations, inter-tower alignment, 0g fluctuations, and uncertainty in the star tracker alignment on the ground may introduce small deviations in the spacecraft-LAT orientation. The deviations in the orientation can introduce a systematic error in the estimation in the PSF, if the effect remains uncorrected. This orientation is called the 'boresight alignment' and in this chapter we derive the boresight alignment of the LAT on-orbit and characterize the performance of the correction.

6.1 Determination from Likelihood Analysis

The boresight alignment of the LAT can be characterized as independent rotations about the LAT x, y, and z axes. The z-axis corresponds to the pointing direction, or boresight, of the LAT and the y-axis corresponds to the direction of the solar panels, as the x-axis is always pointed to the sun. The rotation of a vector, $\hat{r}$, in instrument coordinates under the

boresight alignment, $\vec{\theta}$, may be expressed as

$$\hat{r}'(\vec{\theta}) = \hat{r}'(\theta_x, \theta_y, \theta_z) = \mathbf{R}_x(\theta_x) \times \mathbf{R}_y(\theta_y) \times \mathbf{R}_z(\theta_z) \times \hat{r} \tag{6.1}$$

where $\mathbf{R}_x, \mathbf{R}_y, \mathbf{R}_z$ are the rotation matrices defined as

$$\mathbf{R}_x(\theta) = \begin{pmatrix} 1 & 0 & 0 \\ 0 & \cos\theta & \sin\theta \\ 0 & -\sin\theta & \cos\theta \end{pmatrix} \tag{6.2}$$

$$\mathbf{R}_y(\theta) = \begin{pmatrix} \cos\theta & 0 & -\sin\theta \\ 0 & 1 & 0 \\ \sin\theta & 0 & \cos\theta \end{pmatrix} \tag{6.3}$$

$$\mathbf{R}_z(\theta) = \begin{pmatrix} \cos\theta & \sin\theta & 0 \\ -\sin\theta & \cos\theta & 0 \\ 0 & 0 & 1 \end{pmatrix}. \tag{6.4}$$

This realization was chosen for the small angle commutation properties as the magnitude of the alignment was expected to be $\mid \vec{\theta} \mid \ll 1$. Given the rotation matrix between celestial and instrument coordinates as a function of time, $\mathbf{R}_{sky}(t)$, and the boresight alignment $\mathbf{R}_{bor}(\vec{\theta}) = \mathbf{R}_x(\theta_x) \times \mathbf{R}_y(\theta_y) \times \mathbf{R}_z(\theta_z)$, the boresight alignment transformation of a vector in celestial coordinates, $\hat{r}$, may be expressed as

$$\hat{r}'(\vec{\theta}, t) = \mathbf{R}_{sky}(t) \times \mathbf{R}_{bor}(\vec{\theta}) \times \mathbf{R}_{sky}^{-1}(t) \times \hat{r} = \mathbf{R}_{eff}(\vec{\theta}, t) \times \hat{r} \tag{6.5}$$

where $\mathbf{R}_{eff}(\vec{\theta}, t) = \mathbf{R}_{sky}(t) \times \mathbf{R}_{bor}(\theta_x, \theta_y, \theta_z) \times \mathbf{R}_{sky}^{-1}(t)$.

6.2 L&EO Boresight Alignment

In order to determine the boresight corrections on-orbit, we introduce an analysis that models the angular distribution of γ rays around point sources. The analysis combines the

γ-ray distributions around point sources into a single combined sample, which we denote as a 'stacked' sample. In the previous chapter, we noted the PSF is well-modeled by the King function, so we use it to model the point-source angular distribution of the stacked sample. When a large number of point sources with different background intensities are combined together, the diffuse Galactic γ-ray and residual cosmic-ray background can be modeled as an isotropic distribution, which is uniform in density. The γ rays from point sources above 1 GeV have a substantially narrower angular distribution and a small background, so we limit the analysis to these γ rays. Additionally, the *front*-converting γ rays have a systematically narrower angular distribution than *back*-converting γ rays, so we select *front* only here.

During the Launch & Early Orbit (L&EO) of the LAT, which included the first 55 days of observation beginning on 23 June 2008 (Abdo et al., 2009c), we selected the γ rays from a preliminary set of point sources that had been detected at a significance of 5σ ($TS > 25$) above 1 GeV. The statistics from the point sources are dominated by 4 sources in this energy range: the constant emission of the Vela, Geminga, and Crab pulsars and the flaring blazar 3C 454.3 (Abdo et al., 2009b). We calculated the angular separation (δ) for each γ ray from each source in the preliminary source set and determined the dependence of the separation on the direction, boresight alignment, and time (i.e. $\delta(\hat{r}, \vec{\theta}, t)$). We chose a maximum separation distance of 4°, which corresponds to the 99% containment radius of the `P6_V3` PSF and effectively limits the overlap of point sources. In addition, we binned the data with 4 bins per logarithmic decade in energy between 1–100 GeV to balance the change in the PSF size with the statistics in each energy bin. We used a joint maximum log-likelihood with respect to the reconstructed γ-ray direction to evaluate the best fit parameters to the boresight alignment

$$\log L_{bor}(\{N^{psf}\},\{N^{iso}\},\vec{\theta} \mid \mathbf{r}) = \sum_{i}^{energy} -N_i^{psf} - N_i^{iso} + \sum_{j}^{n_i} \log\left(N_i^{psf} f_i(\delta(\hat{r}_{ij},\vec{\theta},t)) + N_i^{iso}\ I\right) \tag{6.6}$$

where $\mathbf{r}$ is the set of reconstructed γ ray directions; $\{N^{psf}\}$ and $\{N^{iso}\}$ are the number of

γ rays associated with the PSF and isotropic components, respectively, for each energy bin; $f_i(\delta)$ is the effective[1] `P6_V3` PSF, and I is the isotropic normalization. While the effective PSF would traditionally be defined by the integral over the different spatial functions, we make the approximation that

$$\bar{f}_i(\delta \mid \vec{p}) = \mathrm{Eff}[f_i(\delta \mid \vec{p}), A_{\mathrm{eff}}, \Omega_{inst}] \approx f_i(\delta \mid \mathrm{Eff}[\vec{p}, A_{\mathrm{eff}}, \Omega_{inst}]) \tag{6.7}$$

so the A_{eff}-averaged functions can be approximated by the function with A_{eff}-averaged function parameters (averaged over instrument coordinates Ω_{inst}). For the `P6_V3` PSF, the function parameters are σ_c, γ_c, γ_t, and f_c for the double King function in Equation 4.7. The rotation of the vector into instrument coordinates from sky coordinates, $\mathbf{R}_{sky}$, was determined by the data in the corresponding *FT2* file, which includes all spacecraft data as a function of time.

For each evaluation, the log-likelihood in Equation 6.6 was summed over the n_i γ rays in the ith energy bin and then over all energy bins. To obtain the optimal solution, the log-likelihood was maximized with respect to the parameters $\{N^{psf}\}, \{N^{iso}\}$, and $\vec{\theta}$, yielding the boresight alignment constants

$$\begin{aligned} \theta_x &= -170 \pm 28 \text{ arcsec} \\ \theta_y &= -173 \pm 28 \text{ arcsec} \\ \theta_z &= -491 \pm 45 \text{ arcsec.} \end{aligned} \tag{6.8}$$

The log-likelihood contours for one day of data in are shown in Figure 6.1. The large uncertainty in the parameter θ_z is due to the decrease in statistics at large inclination angles where the effective area is smaller than on axis. Since θ_z only affects γ rays which convert at large inclination angles, the statistical uncertainty in θ_z for exposures longer than the orbital precession is a factor of 1.5 larger than θ_x and θ_y. The boresight alignment constants were applied to all data after the L&EO period (after 4 August 2008) in the LAT event reconstruction code.

[1]effective: $\bar{a} = \mathrm{Eff}[a, p, \vec{x}] = \int a(\vec{x}) p(\vec{x})\ d^N x / \int p(\vec{x})\ d^N x$

6.3 3-year Analysis and Boresight Alignment Residuals

After the boresight alignments were applied to all flight data, the effort began to examine the residuals in the alignment over longer time ranges and to validate the constancy of the correction. In addition to the increase in statistics from individual sources, the number of sources with a significance of $TS > 25$ above 1 GeV also increased and were subsequently added to the boresight alignment calibration set. The residuals in the boresight alignment were determined in two ways: 1) by combining measurements and errors in quadrature for small time bins and 2) measuring the alignment for the entire mission. The stability of the boresight alignment was determined from measurements of the alignment in weekly and monthly time bins.

Using the larger set of calibration sources, we applied the analysis of the previous to 3 years of on-orbit data (MET 239557417–334165417s) to determine the residuals in the alignment. We determined the set of point sources which had $TS > 25$ above 1 GeV and used them as the calibration set for the boresight alignment determination. The likelihood from Equation 6.6 was maximized for this data set and the best fit boresight alignment were determined to be

$$\begin{aligned} \theta_x &= -179 \pm 2 \text{ arcsec} \\ \theta_y &= -137 \pm 2 \text{ arcsec} \\ \theta_z &= -465 \pm 4 \text{ arcsec} \end{aligned} \tag{6.9}$$

which corresponds to a relative change of

$$\begin{aligned} \Delta\theta_x &= -9 \pm 28 \text{ arcsec} \\ \Delta\theta_y &= +36 \pm 28 \text{ arcsec} \\ \Delta\theta_z &= +26 \pm 45 \text{ arcsec} \end{aligned} \tag{6.10}$$

where $\Delta\theta$ is the difference between the 3-year correction and the L&EO correction. The boresight alignment for the 3 year data set is consistent within the statistical uncertainties of the L&EO alignment, with the largest excursion in the θ_y value with a change of 1.5σ. The

magnitude of the θ_y difference, $\sim 0.01°$, is much smaller than the PSF size for any energy or conversion type. However, for shorter observations, where a point source spends much more time with a specific orientation with respect to the LAT, the residual may introduce a systematic uncertainty into localizations. The 3 year calibration values have been added to the boresight alignment correction of all on-orbit data in an available reprocessed set.

6.4 Systematic Uncertainties, Stability, and Periodicity

The check of stability and periodic fluctuations of the boresight alignment ensures that the alignment does not require a significant time-dependent characterization and has no time-dependent systematic uncertainty. To examine the systematic uncertainties of the correction, we split the 3-year data set into weekly (604800s), monthly (2592000s), and yearly (31536000s) time bins. The analysis of the Section 6.2 was again applied to each of these data sets, yielding the boresight alignment parameters and uncertainties plotted in Figures 6.2, 6.3, and 6.4. The parameters and their errors were added in quadrature in order to determine the weighted boresight alignment parameters and the statistical uncertainties. The weighted average of the parameters and error determination for the time bins can be expressed as

$$\begin{aligned} \bar{\sigma} &= \left(\sum_{i}^{time\ bins} \frac{1}{\sigma_i^2} \right)^{-1/2} \\ \bar{\theta} &= \bar{\sigma}^2 \sum_{i}^{time\ bins} \frac{\theta_i}{\sigma_i^2} \end{aligned} \tag{6.11}$$

if the measurement errors are assumed to be Gaussian. These values are calculated for each of the boresight alignment parameters in each of the different times binnings, and the results are plotted in Table 6.1. We find that the boresight alignment measurement in each of the time binnings is consistent with the result for the full 3-year analysis. We conclude, based on these results, that there is no systematic uncertainty with the estimate of boresight alignment for short time ranges.

Next, we determined the stability of the boresight alignment by examining the trending

Table 6.1. The boresight alignment parameters and the parameter uncertainties calculated from Equation 6.11. The time bin width, t, is measured in days and N_{bins} is the number of time bins in the analysis. The change in the boresight alignment parameters, $\{\Delta\theta_x, \Delta\theta_y, \Delta\theta_z\}$, are measured in arcseconds.

t	N_{bins}	$\Delta\theta_x$	$\Delta\theta_y$	$\Delta\theta_z$
7	156	-12 ± 2	+35 ± 2	+32 ± 3
30	36	-11 ± 2	+35 ± 2	+33 ± 3
365	3	-11 ± 2	+35 ± 2	+32 ± 3

of the residuals for each of the time binnings. We performed a linear regression on the residuals $r_i = (\theta_i - \bar{\theta})/\sigma_i$ to determine the change in significance as a function of time. Since the yearly time bins only contain 3 data points for each alignment constant, we limit our analysis to the weekly and monthly time bins. Given the slope of the residuals, m_r, for a given boresight alignment parameter, we define the stability, S, and corresponding uncertainty of the residual to be

$$\begin{aligned} S(\vec{\theta}) &= \frac{1}{m_r(\vec{\theta})} \\ \sigma_S(\vec{\theta}) &= \frac{\sigma_m(\vec{\theta})}{m_r(\vec{\theta})^2} \end{aligned} \tag{6.12}$$

where the stability corresponds to the time required for the boresight alignment value to change by 1σ. The stability and corresponding statistical uncertainty for each of the boresight alignment parameters is shown in Table 6.2. We find that the stability of the x and y corrections to the boresight are effectively stable beyond the 3-year time period of the analysis. For the z correction, when the weekly and monthly measurements are combined together, the stability is $S(\theta_z) = 490 \pm 126$ days or roughly 1.5 years. This effect is visible in the yearly plots in Figure 6.4, where the first-year correction for θ_z is significantly smaller than the last two years. However, since the LAT is less sensitive to the θ_z correction and the magnitude of the residual is comparatively small to the L&EO correction, a time-dependent implementation is not required.

In addition to examining linear trends, we looked at the weekly time bins to check for

Table 6.2. The stability of the boresight alignment parameters in days evaluated from Equation 6.12 for the daily and weekly time bins. The stability of each parameter, S, is expressed in days.

t (days)	N_{bins}	$S(\theta_x)$	$S(\theta_y)$	$S(\theta_z)$
7	156	6188 ± 10409	1827 ± 924	1113 ± 315
30	36	20153 ± 227759	1176 ± 735	490 ± 126

periodic fluctuations. The LAT observation strategy changed the rocking angle from 35° from the zenith 50°, in order to help the batteries radiate heat more efficiently. This had the effect of making the exposure for observation periods shorter than the orbital precession highly non-uniform over the sky. To check for significant variation of the boresight alignment, we took the discrete Fourier transform (DFT) of the residuals, R_i, for the weekly time bins. We then generated a Monte Carlo sample, m_i, from a normal distribution with $\mu = 0$ and $\sigma = 1$, which is the null distribution for the r_i, to simulate a random sample of residuals and calculated the corresponding DFT of the sample, M_i. We calculated a p-value for the observed residuals from the Monte Carlo by examining the power spectral density of the residuals and the Monte Carlo ($P_i = R_i^* \times R_i, Q_i = M_i^* \times M_i$), and determined the probability of observing a value for M_i larger than the observed P_i. The significance s in σ of an observed p-value, p, for the power spectral density of the residuals can be calculated from the one-tailed integral of the normal distribution and can be expressed as

$$s = \sqrt{2}\ \mathrm{erfc}^{-1}\,(2p)\,\sigma \tag{6.13}$$

where erfc^{-1} is the inverse complementary error function. For the 3-year weekly boresight alignment analysis, there were no p-values observed for any of the boresight alignment parameters with greater than 3σ significance. There were 8 s-values larger than 2σ observed and listed in Table 6.3. Given the number of time bins and the expected number of fluctuations over 2σ $\left(77 \times \frac{\mathrm{erfc}(\sqrt{2})}{2} \approx 2\right)$ for each boresight alignment parameter, the fluctuations in Table 6.3 are consistent with the null hypothesis. We conclude that there are no significant

Table 6.3. The periods from the DFT of the residuals with a significance greater than 2σ for each boresight alignment parameter in the weekly analysis. The number of fluctuations per alignment parameter are predicted from null distribution to be ≈ 2, so the fluctuations are consistent with the null hypothesis (i.e. no significant periodicity).

$\vec{\theta}$	T(days)	p-value	s
θ_x	17.4	0.021	2.03
	19.2	0.016	2.13
θ_y	15.4	0.004	2.67
	17.7	0.022	2.00
	365	0.013	2.21
θ_z	16.3	0.005	2.59
	22.3	0.003	2.70
	26.7	0.008	2.40

periodic fluctuations in the boresight alignment.

6.5 Summary

The boresight alignment determined by our likelihood analysis shows a primary offset between the LAT and space-craft of $\mid \vec{\theta} \mid \approx 525$ arsec. An analysis of 3 years of the corrected data revealed residuals of the same size as the uncertainty in the initial boresight alignment uncertainty, approximately 30 arcseconds. We examined the residuals for weekly, monthly, and yearly data sets for both linear and periodic trends in the boresight alignment correction and no significant trends were seen. The lack of a linear trending suggests a highly stable correction with no significant time dependence. The lack of periodic trending suggests low systematic uncertainty in the estimation of the boresight alignment for time ranges on the order of one week.

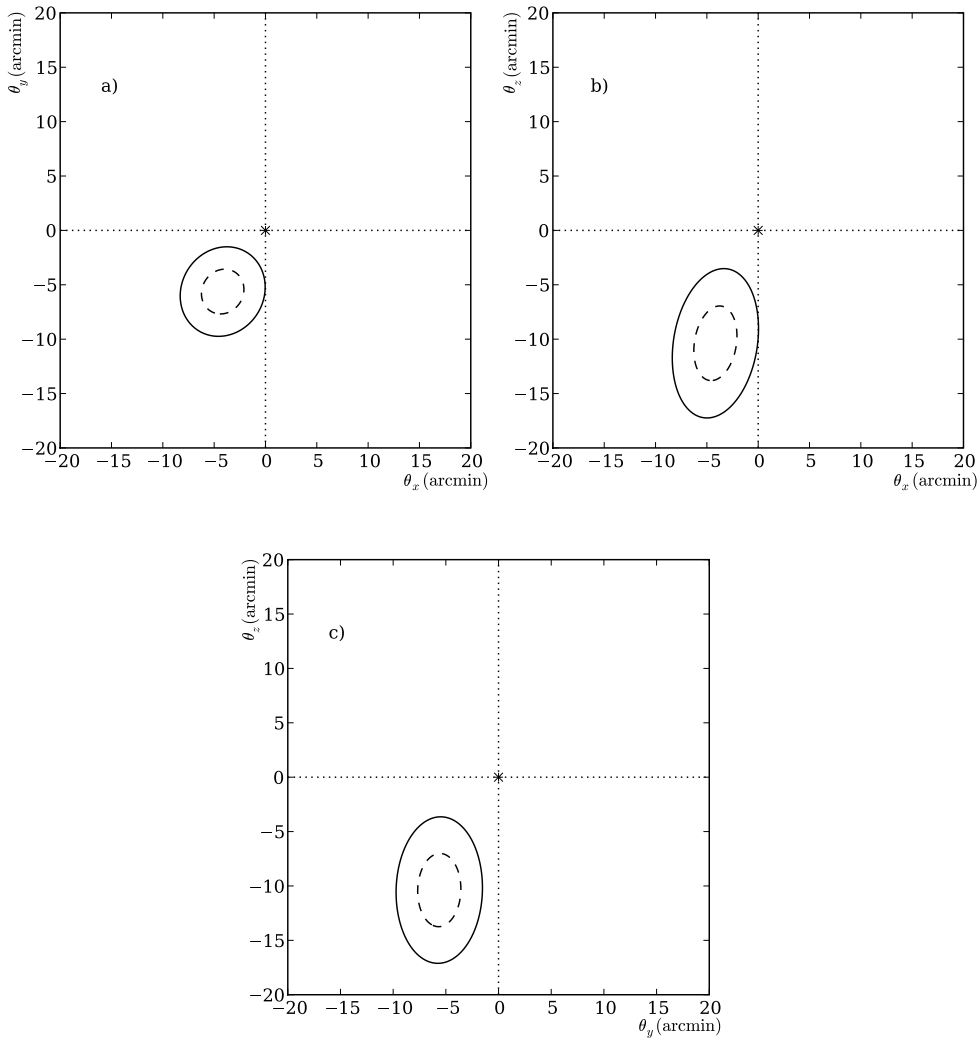

Figure 6.1 Projection of the log-likelihood surfaces for the boresight alignment correction into each of the planes a) θ_y-θ_x, b) θ_z-θ_x and c) θ_z-θ_y for one day of data (3 August 2008). The origin corresponds to the ideal alignment and the contours denote the 68% (dashed) and 95% (solid) containment. The elongation of the projected surfaces with respect to the θ_z correction is due to fewer statistics at larger inclination angles. The units are in arcminutes and the L&EO correction to the boresight alignment corresponds to the coordinate $(\theta_x, \theta_y, \theta_z) = (-2.83, -2.88, -8, 18)$.

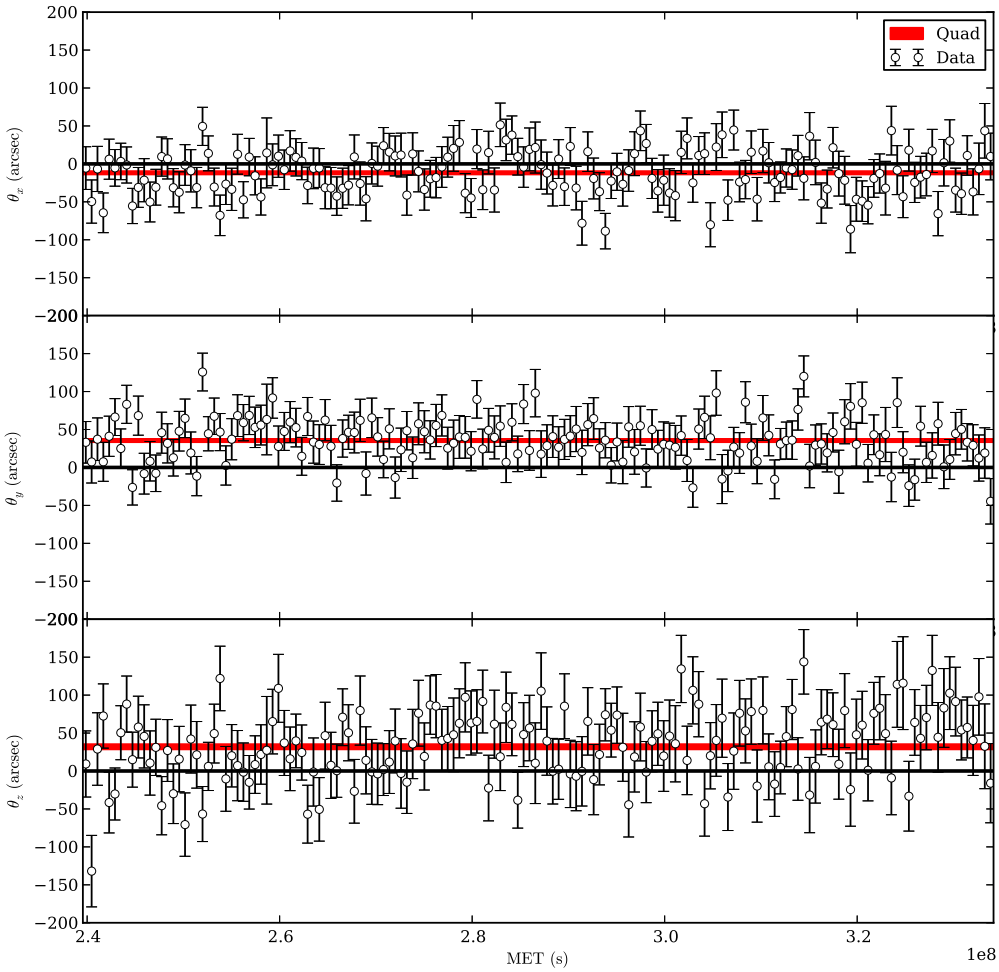

Figure 6.2 Boresight alignment residuals $\Delta\theta_x$ (top), $\Delta\theta_y$ (middle), $\Delta\theta_z$ (bottom), determined from the analysis of weekly time bins for three years of data as a function of the mission-elapsed time (MET). The red bands for each parameter are the weighted average values and uncertainties evaluated from Equation 6.11.

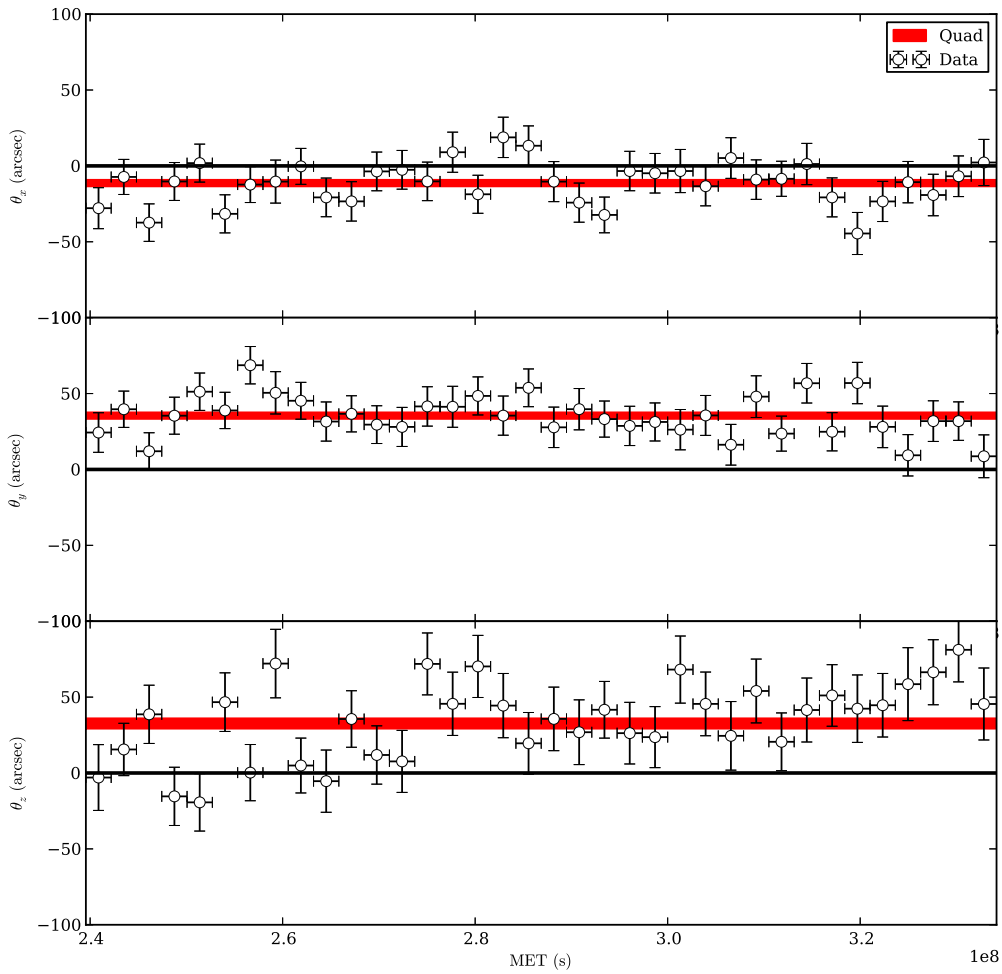

Figure 6.3 Boresight alignment residuals $\Delta\theta_x$ (top), $\Delta\theta_y$ (middle), $\Delta\theta_z$ (bottom), determined from the analysis of monthly time bins for three years of data as a function of the mission-elapsed time (MET). The red bands for each parameter are the weighted average values and uncertainties evaluated from Equation 6.11.

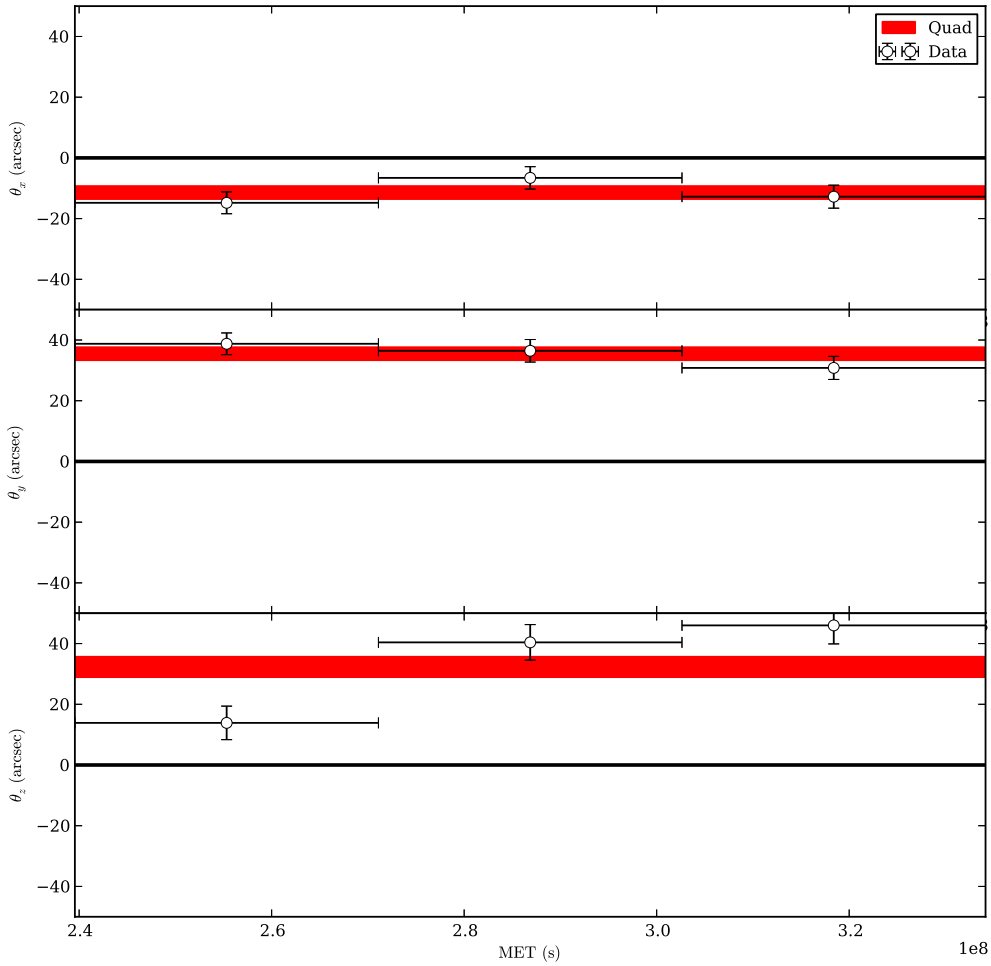

Figure 6.4 Boresight alignment residuals $\Delta\theta_x$ (top), $\Delta\theta_y$ (middle), $\Delta\theta_z$ (bottom), determined from the analysis of yearly time bins for three years of data as a function of the mission-elapsed time (MET). The red bands for each parameter are the weighted average values and uncertainties evaluated from Equation 6.11.

Chapter 7

Determination of the On-Orbit PSF

As we discussed in Section 4.1, we were not able to measure the full response of the LAT before launch and have relied on the instrument response functions derived from simulation. After launch, we began the effort to validate the performance of simulated IRFs in the on-orbit environment. In Section 4.3, we already noted that the presence of 'ghost' particles depositing energy in the TKR, CAL, and ACD a few μs before a the triggering of a event resulted in a substantial loss in the A_{eff}. To examine the validity of the MC PSF, we required sources which emitted γ rays over the entire energy range of the LAT in addition to bright, persistent sources of γ rays. We also required γ rays from sources whose angular extent on the sky is much smaller than the angular resolution of the LAT.

In this chapter, we present an analysis to determine the PSF on-orbit using the γ rays from bright AGN and pulsars. First, we will outline the maximum likelihood analysis used to determine the on-orbit PSF from bright AGN, with no inclination angle dependence. Then, we present the validation of the on-orbit PSF using a cross-check of AGN and pulsars. Additionally, we outline an maximum likelihood analysis to create an on-orbit PSF which introduces inclination angle dependence. Finally, we present a cross-check of the on-orbit PSF with inclination angle dependence using bright pulsars.

7.1 On-Orbit PSF from Bright AGN

For our on-orbit PSF analysis, we chose to use AGN as calibration sources for three reasons 1) large statistics at all energies, 2) low average background intensity, and 3) appearance as true point sources to the LAT. As we described in Section 2.2.2, AGN can be broadband

emitters of γ rays with an average photon index, Γ, of $\approx$2.3. This is in contrast to pulsars that are characterized by a hard spectrum ($\Gamma \simeq 1.5$) with an exponential cutoff around $1-3$ GeV. Pulsars are also often found at low Galactic latitudes, where the hadronic and leptonic interactions of cosmic rays creates a bright, structured background of γ rays. Pulsar Wind Nebulae (PWN), from interactions of charged particles accelerated in the pulsar with the interstellar medium, also can create a bright, structured background (i.e. the Crab Nebula, Abdo et al., 2011b). This makes AGN, in general, good test beds for determining the PSF (we will address point 3 in a later chapter).

We chose a set of 65 bright, associated AGN from the *Fermi* Large Area Telescope First Source Catalog (1FGL, Abdo et al., 2010a) to create a calibration sample. All sources have a flux between 1 and 100 GeV of at least 1.66×10^{-9} photons cm^{-2} s^{-1} and a test statistic (TS) for a point source of at least 81 above 1 GeV. The selection of these dominant sources ensures substantial statistics above 1 GeV, which determines the majority of the localization statistics for point sources.

The data from the *Diffuse* class of the `Pass6` event reconstruction are the best quality for analyzing point sources for longer exposures, as the charged particle background intensity is low. Data for the determination of the `Pass6` *Diffuse* PSF were taken between 4 August 2008 to 4 August 2010 (Mission Elapsed Time (MET) range of 239557417-302629417). Since the average source separation for sources in 1FGL was about 7°, we selected the γ rays between 1 and 100 GeV that were within a region of interest (ROI) with a 4° radius of each source in the AGN calibration sample. The choice of 1 GeV as the minimum energy and the 4° maximum radius was based on the 99% containment radius derived from the MC PSF `P6_V3`, where the *back* converting ROIs would begin to overlap at 1.2 GeV. γ rays which entered the LAT with a zenith angle greater than 105° were excluded to remove any residual contamination from the limb of the Earth, as described in Section 2.2.4. Additionally, γ rays with inclination angles greater than 66.4° were excluded, as the PSF is substantially worse in this range and the $A_{\rm eff}$ is small. The data were split up by their conversion types, *front* and *back*, as the *back* angular distributions are twice as broad on average as the *front*. The data were also binned in energy, with four logarithmically spaced bins per decade between

1 and 32 GeV and a single energy bin between 32 and 100 GeV. The angular separation δ was calculated between the 1FGL location of the calibration source and each γ ray in the ROI of the source and into a single set of angular separations $\{\delta\}$ for each energy bin. The uncertainty in the localized position of each source in the 1FGL catalog is negligible with respect to the PSF size, so these positions were adopted as the 'true' position.

The principle behind the likelihood analysis used to determine the on-orbit PSF is quite similar to the likelihood analysis used to determine the boresight alignment; namely, the combined angular distributions of γ rays around AGN are modeled as the sum of the PSF and a uniform, or isotropic background. In Section 6.2, we defined the likelihood for the boresight in terms of the an assumed PSF form $f_i(\delta)$, the A_{eff}-weighted average `P6_V3` PSF. The `P6_V3` PSF, which overlays the 'ghost' tracks in the determination of the PSF, makes a simplification to the form of the PSF by setting $\sigma_c = \sigma_t$ in Equation 4.7 to aid in the convergence of the parameter fitters in the MC. In our determination of the on-orbit PSF, we make a further simplification by adopting Equation 4.2 (single King function) as the PSF form, which has just two free parameters, σ and γ. The extended log-likelihood for the model of the distribution of γ rays around the bright AGN for each energy bin is expressed as

$$\log L(N^{psf}, N^{uni}, \sigma, \gamma \mid \{\delta\}) = -N^{psf} - N^{uni} + \sum_{j}^{photons} \log\Big(N^{psf}\ K(\delta_j, \sigma, \gamma) + N^{uni}\ I\Big) \tag{7.1}$$

where $\{\delta\}$ are the set of angles between each γ ray and each source in the calibration sample, N^{psf} and N^{uni} are the models for the numbers of PSF and background γ rays, K is the King function of Equation 4.2, and I is the uniform background model normalization. We also limited the dependence of the σ and γ to energy only, using a single inclination angle bin for a each energy bin. The PSF form and inclination independence were implemented to aid in the determination at high energy (>10 GeV), where the number of source γ rays is small.

In addition to correctly modeling point sources on-orbit with the PSF, we also wished to smooth the energy dependence of the parameterization, as the statistical fluctuations in

the on-orbit PSF parameters are large at high energy. As we noted in Section 4.2, the σ parameter is represented well by the scaling function $S_P(E)$ (Equation 4.6). However, the energy dependence of γ is generally much more complicated, so we looked for an alternative method for smoothing. We found the energy dependence of the 68 and 95% containment radii from the MC PSF, like σ, has form which is close to $S_P(E)$. We also noted in Section 4.2 that for a single King function, any two containment radii completely determine the parameters σ and γ. With this principle in mind, we modeled the energy dependence of 68 and 95% containment radii with Equation 4.6, using two different sets of values for c_0, c_1, and β.

We formulate the maximum likelihood analysis parameterized by the 68 and 95% containment radii, modeling the angular distributions as the sum of a single King function and a uniform background. The extended log-likelihood of this model can be expressed as

$$\begin{aligned} &\log L_{tot}(\theta_{0,68}, \theta_{1,68}, \beta_{68}, \theta_{0,95}, \theta_{1,95}, \beta_{95} \mid \{\delta\}) = \\ &\qquad \sum_{i}^{Energy\ bins} \log L(N^i_{psf}, N^i_{iso}, \sigma(R_{68}(E_i), R_{95}(E_i)), \gamma(R_{68}(E_i), R_{95}(E_i)) \mid \{\delta\}_i) \end{aligned} \tag{7.2}$$

where the subscripts 68 and 95 denote the parameters from Equation 4.6 representing the 68 and 95% containment radii, respectively. The dependence of R_{68} on $\theta_{0,68}$, $\theta_{1,68}$, and β_{68} (and equivalently for R_{95}) is implied in the likelihood, E_i is the mean energy of the energy bin, and $\log L$ is the log-likelihood from Equation 7.1. The log-likelihood in Equation 7.2 was maximized with respect to the 68 and 95% containment radii parameters and the parameters for the A_{eff}-averaged MC PSF `P6_V3` are compared with those from this analysis, which was named `P6_V11`, in Table 7.1. The A_{eff}-averaged `P6_V3` PSF is plotted against the `P6_V11` PSF as a function of energy in Figure 7.1.

We find that the on-orbit PSF is generally broader than the MC simulations beginning above a few GeV, where the PSF is beginning to be limited by ratio of the track length to the instrument pitch, or the 'geometric' angle. The broadening effect can be seen clearly in Table 7.1, where the parameter c_1 characterizes the magnitude of the geometric angle. The on-orbit PSF parameter c_1 is consistently a factor of two larger than the MC, which

accounts for the majority of the discrepancy between MC and data seen in Figure 7.1.

To examine potential systematic uncertainties of determining the PSF from on-orbit data, specifically the extrapolation of the PSF beyond the 1-100 GeV range, we generated and analyzed a detailed simulation of the sky. We simulated all sources from the *Fermi* Large Area Telescope Second Source Catalog (2FGL; Nolan et al., 2012), along with the Galactic and isotropic diffuse models, using the *ScienceTool gtobssim* with the `P6_V3` PSF. The simulation covered the same time span as the on-orbit data selection and used the same cuts on inclination angle, energy, and zenith angle. We chose to use the 2FGL catalog for the simulation to account for the presence of sources not in the 1FGL that could introduce structured background and create a systematic uncertainty in the PSF determination. We analyzed the simulation with the same set of 65 AGN from the on-orbit PSF analysis and determined the simulation PSF in the same manner as the on-orbit data, using Equation 7.2. The 68 and 95% containment radii determined by the PSF analysis are compared with the corresponding the `P6_V3` PSF containment in Figure 7.2. We find good agreement between the 68 and 95% containments derived from the `P6_V3` PSF and the corresponding containments derived from the sky simulation. Additionally, we find the containment radii extrapolated below 1 GeV and above 100 GeV is in good agreement. This is a reasonable expectation, as the containment follows the $E^{-0.8}$ power law from muliple scattering closely below 1 GeV and the constant geometric angle above 100 GeV.

Since there was a large discrepancy between the MC and on-orbit PSF, we sought to confirm the validity and consistency of the on-orbit PSF using other techniques and source types. In the next section, we outline a PSF model-independent check on the on-orbit PSF using the data from bright pulsars and bright AGN.

7.2 Validation

As we noted in Section 2.2.1, the pulsed emission from a pulsar appears as a true point source to the LAT. The pulsed emission is often isolated in the phase window so that we can effectively separate the pulsar emission from the the background pulsar wind nebula (PWN) and Galactic and isotropic diffuse γ-ray emission. The two brightest γ ray pulsars (and point

Table 7.1. The parameters of the scale function $S_P(E)$ representing the 68 and 95% containment radii for the MC (`P6_V3`) and on-orbit (`P6_V11`) PSF. The parameter c_0 corresponds to the containment radius at 100 MeV due primarily to multiple scattering, c_1 corresponds to the containment radius at 100 GeV defined by the geometric angle, and β is the power-law dependence of the multiple scattering.

PSF	$c_{0,68}[^\circ]$	$c_{1,68}[^\circ]$	β_{68}	$c_{0,95}[^\circ]$	$c_{1,95}[^\circ]$	β_{95}
`P6_V3` *front*	3.882	0.056	0.810	10.619	0.160	0.852
`P6_V11` *front*	4.088	0.109	0.839	11.155	0.301	0.844
`P6_V3` *back*	5.816	0.092	0.760	17.794	0.357	0.841
`P6_V11` *back*	6.700	0.263	0.796	20.997	0.756	0.786

sources) are the Vela (PSR J0835−4510) and Geminga (PSR J0633+1746) pulsars. Both pulsars have extremely peaked pulsed emission (∼15% of the phase) with a signal-to-noise ratio between 100−200. The pulsars also have ∼30% of the phase where the background emission is dominant and the Vela pulsar emission, in particular, is completely absent. In contrast to the previous sections, we make no assumptions about the functional form that best describes the pulsars' γ-ray angular distributions, but rather examine the inferred integral distributions of source γ rays. In this section, we create a model independent check of the on-orbit PSF based on the containment radii derived from the cumulative distributions of γ rays from pulsars and AGN to estimate its accuracy.

The γ-ray sample from the Vela and Geminga pulsars was divided into four logarithmic bins per decade in energy and also separated into *front* and *back* conversion types. For each energy bin and conversion type, on- and off-pulse angular distributions were created from the pulsar data sample by selecting events with pulse-phase ranges given in Table 7.2. The pulse phases for the Vela pulsar were determined by using ephemerides derived from timing with the Parkes telescope (Weltevrede et al., 2010) and the pulse phases for the Geminga pulsar were determined from *Fermi* data (Abdo et al., 2010c). The pulse phases were applied to LAT data with the TEMPO2 application (Hobbs et al., 2006)[1]. Light curves for Vela and Geminga can be seen in Figure 7.3, displaying the peaked on-pulse pulsar emission and the long off-pulse background dominated phase. The background in

[1] *Fermi* pulsar ephemerides may be found at http://fermi.gsfc.nasa.gov/ssc/data/access/lat/ephems/

Table 7.2. On- and off-pulse phase selection for Vela and Geminga pulsars.

Source	On-pulse	Off-pulse
Vela (PSR J0835−4510)	0.1–0.15, 0.5–0.6	0.7–0.1
Geminga (PSR J0633+1746)	0.1–0.17, 0.6–0.68	0.25–0.55

Table 7.3. 68% containment radii of the LAT PSF for *front* events in the *Diffuse* class as a function of energy bin inferred from different calibration data sets: Vela, Geminga, and the AGN calibration sample. The containment radius of a source with the observing profile of Vela and a power-law energy distribution with a photon index $\Gamma = 2$ calculated with the `P6_V3` and `P6_V11` IRFs is shown for comparison.

Energy Bin [$\log_{10}$(E/MeV)]	Vela	Geminga	AGN	P6_V3	P6_V11
2.00 – 2.25	2.62 ± 0.06	2.2 ± 0.2	···	2.77	2.99
2.25 – 2.50	1.94 ± 0.02	2.02 ± 0.09	···	1.88	1.96
2.50 – 2.75	1.24 ± 0.01	1.25 ± 0.03	···	1.21	1.23
2.75 – 3.00	0.771 ± 0.008	0.78 ± 0.01	···	0.754	0.763
3.00 – 3.25	0.48 ± 0.005	0.483 ± 0.008	···	0.466	0.481
3.25 – 3.50	0.313 ± 0.004	0.301 ± 0.005	···	0.300	0.309
3.50 – 3.75	0.205 ± 0.004	0.212 ± 0.006	0.188 ± 0.005	0.201	0.209
3.75 – 4.00	0.173 ± 0.009	0.20 ± 0.01	0.168 ± 0.006	0.139	0.154
4.00 – 4.25	0.15 ± 0.01	0.13 ± 0.02	0.137 ± 0.008	0.0984	0.128
4.25 – 4.50	0.11 ± 0.02	0.19 ± 0.07	0.113 ± 0.007	0.0723	0.116
4.50 – 4.75	···	···	0.088 ± 0.009	0.0576	0.112
4.75 – 5.00	···	···	0.08 ± 0.01	0.0516	0.110

the on-pulse distributions was estimated by scaling the off-pulse distributions by the ratio of the widths of the on- and off-pulse phase intervals. The angular distribution of γ rays from a point source was then inferred as the differences by angular bin of the on- and scaled off-pulse counts distributions. This technique should provide a perfect subtraction of any steady sources of γ-ray emission, such as a PWN or the diffuse emission described above. The Vela-X PWN, a spatially extended source that is offset from the Vela Pulsar by $\sim 1°$, is approximately 500 times fainter than the Vela pulsar at 1 GeV (Abdo et al., 2010b). No evidence for a PWN has been found associated with the Geminga pulsar (Ackermann et al., 2011a).

Above 10 GeV where the statistics in the pulsar data set are limited, a comparison was made with the same high-latitude AGN sample that was used to derive the on-orbit

Table 7.4. 68% containment radii of the LAT PSF for *back* events in the *Diffuse* class as a function of energy bin inferred from different calibration data sets: Vela, Geminga, and the AGN calibration sample. The containment radius of a source with the observing profile of Vela and a power-law energy distribution with a photon index $\Gamma = 2$ calculated with the `P6_V3` and `P6_V11` IRFs is shown for comparison.

Energy Bin [$\log_{10}$(E/MeV)]	Vela	Geminga	AGN	P6_V3	P6_V11
2.00 – 2.25	4.7 ± 0.1	5.0 ± 0.5	$\cdots$	4.74	5.04
2.25 – 2.50	3.29 ± 0.04	3.2 ± 0.1	$\cdots$	3.21	3.38
2.50 – 2.75	2.12 ± 0.02	2.1 ± 0.05	$\cdots$	2.09	2.18
2.75 – 3.00	1.35 ± 0.01	1.41 ± 0.03	$\cdots$	1.31	1.40
3.00 – 3.25	0.88 ± 0.01	0.89 ± 0.01	$\cdots$	0.822	0.911
3.25 – 3.50	0.59 ± 0.01	0.6 ± 0.01	$\cdots$	0.525	0.613
3.50 – 3.75	0.412 ± 0.009	0.44 ± 0.01	0.40 ± 0.02	0.347	0.440
3.75 – 4.00	0.37 ± 0.02	0.34 ± 0.02	0.36 ± 0.02	0.240	0.344
4.00 – 4.25	0.37 ± 0.05	0.29 ± 0.04	0.30 ± 0.02	0.175	0.299
4.25 – 4.50	0.3 ± 0.2	0.5 ± 0.3	0.19 ± 0.02	0.136	0.278
4.50 – 4.75	$\cdots$	$\cdots$	0.19 ± 0.03	0.113	0.269
4.75 – 5.00	$\cdots$	$\cdots$	0.23 ± 0.05	0.101	0.265

PSF model. For the stacked AGN sample, the background was estimated by assuming an isotropic intensity determined by the γ rays in the annulus of angular radius range $1.5^\circ - 3.0^\circ$ centered on the stacked 1FGL coordinates of the blazars. The 68% and 95% containment radii for the events in each energy bin were measured from the inferred cumulative distribution of the excess. The statistical errors on the containment radii derived from both pulsars and stacked AGN were estimated from the dispersions of containment radii determined from a large sample of Monte Carlo realizations for the signal and background distributions.

Tables 7.3 and 7.4 give the 68% containment radii for *front* and *back* events estimated from Geminga and Vela below 31.6 GeV and the AGN calibration data set above 3.16 GeV. For comparison the exposure- and spectrally-weighted PSF model prediction for the `P6_V3` and `P6_V11` PSFs are shown for a source with the observing profile of Vela and a power-law energy distribution with a photon index of $\Gamma = 2$. The observing profile is the accumulated exposure time of a source as a function of its inclination angle in the LAT. Although the effective PSF depends on the observing profile[2], for observations that span a time period many times greater than the orbital precession period of the LAT (53.4 days), which is the

[2]observing profile: $\int S(\theta, \phi, t) L(\theta, \phi, t) d\Omega dt$, where S is the location of the source in instrument coordinates and L is the livetime

case for this analysis, the effective PSF model has only a weak dependence on the source location on the sky and is primarily a function of declination. In the energy range 100 MeV – 100 GeV, the largest difference between the `P6_V3` 68% containment radii calculated with the observing profiles of Vela and the stacked AGN sample is 2%, and we therefore assume that the differences in the observing profiles of the calibration data sets can be ignored for the purposes of these comparisons. We find that the AGN and pulsar data sets analyzed here give consistent estimates of the PSF size as a function of energy. The agreement between the containment radii inferred from Geminga and Vela validates the approach of using the off-pulse γ rays to define the background.

Figures 7.4 and 7.5 compare the PSF containment radii inferred from Vela and the AGN calibration data sets as a function of energy with the containment radii given by the `P6_V3` and `P6_V11` PSFs for *front* and *back* events, respectively. The residuals of both PSFs in the 68% containment radius are less than 10% below 3 GeV for both event classes. Above 3 GeV the MC PSF model (`P6_V3`) begins to significantly underpredict the size of the 68% containment radius of both *front* and *back* events. The on-orbit PSF model (`P6_V11`) provides an improved representation of the 68% containment radius at high energies with residuals less than 20% but overpredicts the 95% containment radius for *back* events. We attribute the `P6_V11` *back* residual to using the single King function parameterization, which can overestimate the 95% containment radius of the PSF (see for example Figure 4.1).

7.3 Systematic Errors of the PSF

Although the reason for the discrepancy between the on-orbit (`P6_V11`) and MC (`P6_V3`) IRFs at high energies is not fully understood, we argue that it is not due to intrinsic broadening of the γ-ray distributions around the AGN sample that was used for calibration. Above 3 GeV the discrepancy in the 68% containment is $0.1-0.2^\circ$ for *back* events but $< 0.1^\circ$ for *front* events (see Tables 7.3 and 7.4). Given that the *front* PSF is approximately two times narrower than the *back* PSF, this discrepancy can not be self-consistently modeled as an intrinsic spatial extension convolved with the LAT PSF. Furthermore, in the intermediate energy range (3 GeV – 30 GeV) where the PSF can be independently measured using both

pulsars and AGN, the PSF containments inferred from pulsars are found to be consistent with those inferred from AGN (see Tables 7.3 and 7.4). We therefore conclude that the the majority of the PSF discrepancy can be attributed to systematic uncertainty in modeling the LAT.

In the LAT event reconstruction software (Atwood et al., 2009), positional and directional information from the Calorimeter (CAL) detector system is used to seed the pattern recognition analysis that is applied to track candidates recorded by the Tracker (TKR) detector system. The seed provided by the CAL becomes especially important at high energies (above $\sim$3 GeV), where events typically have several track candidates present in the TKR. The calculation of position information from the CAL relies on accurate maps of the scintillation response of the CAL crystals (Atwood et al., 2009; Grove & Johnson, 2010). The response maps used to produce the `Pass6` *Diffuse* data release were derived prior to launch using cosmic ray muons.

We identified the crystal response maps as a possible source of the discrepancy between the observed and simulated PSF at high energies, either because of a time dependence in the crystal response or because of an inaccuracy of the maps in representing the actual spatial dependence of the crystal response. To evaluate whether the PSF discrepancy was changing with time, we determined the 68% and 95% containment radii for each of the energy bins in Section 7.1 in six 5-month intervals. We detected no significant changes in the containment radii in the energy range $1-32$ GeV for either conversion type. Over the same time interval, however, on-orbit radiation damage to the scintillating crystals caused a typical decrease in scintillation light attenuation length of about 3%, which corresponds to an average position bias of 3 mm near the ends of crystals and up to 10 mm bias in the most sensitive crystals. Because the PSF did not show a detectable change with time, we conclude that time dependence in the crystal response is not the dominant source of the PSF discrepancy.

To test whether inaccuracy in the response maps could be the cause, we reanalyzed the sea-level and on-orbit cosmic ray calibration data to derive maps that more closely describe the response near the end of each crystal. Using the revised response maps, we repeated

the event reconstruction for a test data set consisting of events from five AGN from the calibration sample at high latitude toward directions with low intensities of Galactic diffuse emission. For γ rays with energy greater than 5 GeV, we found that the mean angular separation from the source position in this event sample drops from $0.133^\circ \pm 0.004^\circ$ to $0.114^\circ \pm 0.004^\circ$. By using the improved calibration, we recovered $\sim 70\%$ of the resolution loss relative to the Monte Carlo expectation. We conclude, therefore, that inaccuracy in the crystal response maps used for the `Pass6` *Diffuse* event reconstruction indeed is the source of much of the PSF discrepancy.

7.4 Inclination angle-Dependent On-Orbit PSF

As discussed earlier in the chapter, the on-orbit PSF derived for the `Pass6` *Diffuse* event reconstruction has no inclination-angle dependence built into the PSF definitions and has only a single King function representation. While the inclination angle averaged PSF is useful for exposures longer than the orbital precession period of the spacecraft, significant discrepancies in flux measurements of the Crab were seen for time scales on the order of days. To facilitate short term observations, we developed a maximum likelihood analysis to model the inclination-angle dependence of the PSF, using the γ rays from pulsars and bright AGN binned in energy, inclination angle, and the angular separation between the γ ray and source δ. The analysis implements a smoothing of the PSF parameters based on a weighting of the log-likelihood in energy and inclination angle.

The standard event reconstruction is currently `Pass7`, which incorporates many of the observed on-orbit effects into the classification and energy reconstruction steps, but makes no changes to the location and geometry of the γ rays. The `P7_V4` *Source* class, similar to the `P6_V3` *Diffuse*, has the largest number of probable γ rays along with a charged particle background intensity acceptable for point-source analysis. We selected data from this class for the analysis between 4 August 2008 and 4 Nov 2011 (MET 2395574717s to 342114217s), or roughly 3.25 years, and applied a zenith angle cut of 90° and an inclination angle cut of 78.5° (see Section 7.1 for more details on these cuts). We selected data between 100 MeV and 100 GeV and binned the γ rays in 8 logarithmic bins per decade between 100 MeV

and 1 GeV, 4 bins per decade between 1 GeV and 32 GeV, and a single bin between 32 and 100 GeV. We binned the data in inclination angle $\cos\theta$ bins: between $\cos\theta$ of 0.2 to 0.6, 0.6 to 0.8, and 0.8 to 1.0, to balance the statistics in each bin. For each energy and $\cos\theta$ bin, we calculated an average energy and $\cos\theta$ value to represent the 'characteristic' central values of the bin. All of the binning choices were structured to make the statistics as even as possible across energy and inclination angle. We chose ROI's for each source such that the radius of the ROI was equal to $1.5 \times R_{99.5}$ for the 99.5% containment radius of the `P6_11` PSF, giving each energy bin an ROI containing a majority of the PSF shape. We determined the on- and off- pulse data for the Vela and Geminga pulsars using the same phase selection parameters as the previous section. For each energy and inclination bin for the AGN, we took the data from the ROI of each source and combined the angular separation of γ rays from their associated sources into a single sample.

In the previous section, we outlined a method for obtaining a very pure point-source model from pulsars through the technique of phase-gated background subtraction. In this section, we will use the data from the pulsars to characterize the PSF at energies below 1 GeV and a combination of AGN and pulsar data above 1 GeV. To speed up the likelihood calculations, we introduce a binning for the angular distribution of γ rays around sources, with a general goal of dividing the statistics evenly between angular bins. With this in mind, our model for the number of on-pulse γ rays from a pulsar in angular bin i can be expressed as

$$\nu_i^{on}(N^{psf}, m_i, \nu_i^{off}) = m_i N^{psr} + \alpha \nu_i^{off} \tag{7.3}$$

where m_i is the fraction PSF in the ROI contained in angular bin i, N^{psr} is the model for the number of γ rays from the pulsar, ν_i^{off} is the model for the number of off-pulse pulsar γ rays in angular bin i, and α is the ratio between the on- and off-pulse phase widths. At energies below 10 GeV, we chose angular bins edges such that n_i^{on}, the number of observed on-pulse pulsar γ rays in angular bin i, is the same for all angular bins.

Above 1 GeV, the overlap of the bright AGN ROI is minimal, so we use data from the calibration sample of 65 AGN from the `Pass6` analysis to supplement the pulsar data in the energy range $1-10$ GeV. Our model for the combined emission of the AGN is a sum of the

PSF and an isotropic (uniform) component and the number of γ rays in angular bin i may be expressed as.

$$\nu_i^{agn}\left(N^{agn}, N^{iso}, m_i, b_i\right) = m_i N^{agn} + b_i N^{iso} \tag{7.4}$$

where N^{agn} is the model for the total number of source γ rays in the ROI, N^{iso} is the model for the number of isotropic γ rays in the ROI, and b_i is the fraction solid angle in the ROI contained in angular bin i. Above 10 GeV, the pulsed emission from pulsars is too weak to characterize the PSF, so we use only the bright AGN data between 10 and 100 GeV. We determined the optimal angular bin edges by estimating the background density at large separations and subtracting it and used the inferred PSF distribution to make m_i roughly equal in each angular bin. A summary of the energy binning for the pulsars and AGN can be found in Figure 7.6.

Given the models of the pulsar on- and off-pulse emission and the model of the bright AGN, we define a log-likelihood in terms of the free parameters for each energy and inclination angle bin

$$\begin{aligned}\log L(N^{psr}, N^{iso}, N^{agn}, \nu_i^{off},\ \vec{m}(\sigma_c, \sigma_t, \gamma_c, \gamma_t, f_c), \vec{b} \mid \{n^{on}\}, \{n^{off}\}, \{n^{agn}\}) = \\ \sum_i^{\delta\ bins} \log L_P\left(\nu_i^{on}(N^{psf}, m_i, \nu_i^{off}) \mid n_i^{on}\right) + \\ \sum_i^{\delta\ bins} \log L_P\left(\nu_i^{off} \mid n_i^{off}\right) + \\ \sum_i^{\delta\ bins} \log L_P\left(\nu_i^{agn}\left(N^{agn}, N^{iso}, m_i, b_i\right) \mid n^{agn}\right)\end{aligned} \tag{7.5}$$

given the number observed counts in the angular bins for on-pulse pulsar emission $\{n^{on}\}$, off-pulse pulsar emission $\{n^{off}\}$, and the AGN $\{n^{agn}\}$. $\log L_P$ is the log-likelihood for the Poisson distribution, defined as

$$\log L_P(\nu \mid n) = \log\left(\frac{e^{-\nu}\nu^n}{n!}\right) = n\log(\nu) - \nu - \log n! \tag{7.6}$$

where ν counts are predicted to n observed. The PSF, $\vec{m}$, is modeled as the double King function (Equation 4.7), where the values are calculated by determining the fraction of the

PSF in each bin for the ROI.

To create a smoothly varying set of PSF parameters in energy and inclination angle, we use a linear approximation for the local variation of the parameters and then calculate a weight to the log-likelihood from 'nearby' energy and inclination angle bins. The linear approximation of the parameters can be expressed in terms of two slopes ($s_{\log E}, s_{\cos\theta}$) and a central value p_0

$$p(p_0, s_{\log E}, s_{\cos\theta}, E_0, \theta_0 \mid E, \theta) = s_{\log E}\left(\log\frac{E}{E_0}\right) + s_{\cos\theta}(\cos\theta - \cos\theta_0) + p_0 \tag{7.7}$$

for reference energy E_0 and inclination angle θ_0. For the set of PSF parameters $\vec{p} = \{\sigma_c, \sigma_t, \gamma_c, \gamma_t, f_c\}$, this requires 15 parameters overall (3 for each double King parameter). Given the set of log-likelihood values for a realization of the PSF $\vec{m}$ in each inclination angle and energy bin (freeing all of the other parameters in Equation 7.5), we calculate a weighted log-likelihood for the linear approximation as

$$\log L_w(\vec{p_0}, \vec{s}_{\log E}, \vec{s}_{\cos\theta} \mid \{\log L\}, E, \theta) = \sum_j^{E\ bins}\sum_k^{\theta\ bins} \log L_{jk}(\vec{m}\,(\vec{p_0}, \vec{s}_{\log E}, \vec{s}_{\cos\theta}, E_j, \theta_k)) \exp\left(-\frac{d(E, E_j, \theta, \theta_k)^2}{2}\right) \tag{7.8}$$

where d, the distance measure is defined as

$$d(E, E_j, \theta, \theta_k)^2 = w \times \left(16 \cdot \log_{10}\left(\frac{E_j}{E}\right)^2 + 100 \cdot (\cos\theta_k - \cos\theta)^2\right) \tag{7.9}$$

where w is a scale factor set to 0.5 in this case. The factor of 16 for the $\log E$ scales the energy dependence to 4 steps per logarithmic decade and the factor of 100 scales the $\cos\theta$ dependence to steps of 0.1. These factors transition between the energy bins used in the analysis to the energy bins of the tables of PSF parameters in the *ScienceTools* software. The principle behind the weighted log-likelihood is simple: the further from the reference E and θ the bin is, the less it contributes to the overall log-likelihood. The PSF parameters in the *ScienceTools* tables were derived for 18 bins in energy from 18 MeV to 562 GeV and 8

bins in $\cos\theta$ from Equation 7.8 and the data described above. The 68 and 95% containment radii for the MC PSF (`P7SOURCE_V6MC`), the on-orbit PSF generated from the analysis in Section 7.1 for `Pass7` data (`P7SOURCE_V6`), and the PSF generated with inclination angle dependence (`P7SOURCE_VX`) are compared in Figure 7.7.

7.5 Validation of Inclination-angle Dependent On-Orbit PSF

To validate the short term validity of the inclination angle dependent PSF, Dr. Rolf Buehler, a member of the *Fermi* collaboration, constructed a test bench for validation based on short term measurements of the flux of the Vela and Geminga pulsars. The test bench involved running the *Fermi* Science Tool *gtlike*, a general likelihood application for modeling sources, in unbinned mode on 12-hour time bins to measure the pulsar flux using different PSFs. When the analysis was constructed, 109080000 seconds of livetime data were available ($\sim$3.45 years), creating 2505 separate measurements for each pulsar. He used data from the `Pass7` *Source* event analysis between energies of 70 MeV and 100 GeV with an ROI of 15° around each pulsar and tested the `P7SOURCE_V6MC`, `P7SOURCE_V6`, and `P7SOURCE_VX` PSFs. The *gtlike* application modeled all of the 2FGL sources, Galactic diffuse emission, and isotropic emission in the ROI, with spectral and spatial parameters fixed to their 2FGL values. The only free parameters in the *gtlike* analysis were the flux normalization for the pulsars and the isotropic background flux normalization.

As with the check for systematic periodicity of the boresight alignment parameters in Section 6.4, we quantified the short term systematics of the PSFs with a Fourier analysis. We determined the weighted average value of the flux (Equation 6.11) and calculated the residuals $r_i = (\bar{f} - f_i)/\sigma_i$. We took the DFT of r_i to obtain the frequency components of the residuals R_i. To determine the significance of the R_i, we ran 100000 simulations of r_i for the expected null distribution (a normal distribution with μ=0 and σ=1) and determined the number of fluctuations with $M_i^* M_i > R_i^* R_i$. From the p-value of the simulations, we calculated the corresponding significance in terms of the normal distribution. The most significant frequency components were in the Vela analysis, where all PSFs showed indications of systematic differences with the same period as the 53.4-day orbital precession of the LAT.

Table 7.5. The comparison of the average absolute flux normalization $\bar{F}_n$ and uncertainty $\bar{\sigma}_n$ for the PSFs normalized to the flux normalization obtained by the MC PSF `P7SOURCE_V6MC`.

Source	PSF	$\bar{F}_n$	$\bar{\sigma}_F$
Vela	`P7SOURCE_V6MC`	1.0000	0.0017
Vela	`P7SOURCE_V6`	1.0700	0.0015
Vela	`P7SOURCE_VX`	1.0526	0.0015
Geminga	`P7SOURCE_V6MC`	1.0000	0.0029
Geminga	`P7SOURCE_V6`	1.0854	0.0024
Geminga	`P7SOURCE_VX`	1.0828	0.0024

These differences were above the 4σ level (less that 1 in 100000) for all PSFs. For Geminga, however, only the `P7SOURCE_V6` PSF shows significant evidence of periodicity, indicating that the long term averaged PSF fails for sufficiently short observations. Not surprisingly, the systematic differences for the `P7SOURCE_V6` PSF are worse for both Vela and Geminga compared to the PSFs with inclination angle dependence. While the existence of systematic periodicity indicates the time-averaged PSF is insufficient for this type of analysis, the test bench only reports relative differences in flux. In Table 7.5, we compare the average flux normalizations determined by each PSF and find that the MC PSF underpredicts the flux with respect to the on-orbit PSFs by $5-10\%$. Based on these results, the inclination angle dependence in `P7SOURCE_VX` reduces the systematic uncertainty for extremely bright sources for short observations (compared to `P7SOURCE_V6`) and more accurately measures the flux for longer observations (compared to `P7SOURCE_V6MC`).

7.6 Summary

We derived the on-orbit PSF using a combined data set from bright AGN and found significant differences compared to the MC PSF starting at a few GeV. We checked the results of the AGN analysis against an analysis of bright pulsars and continued to find differences with the MC PSF. We then constructed an on-orbit PSF with inclination-angle dependence of the parameterization using the combined data of pulsars and AGN. We checked for sys-

tematics of this PSF by checking pulsar flux measurements for short time scales and found discrepancies for only the single brightest γ-ray pulsar. We conclude that the inclination angle dependence of the PSF is only necessary for observations of the brightest sources in time ranges shorter than the orbital precession period.

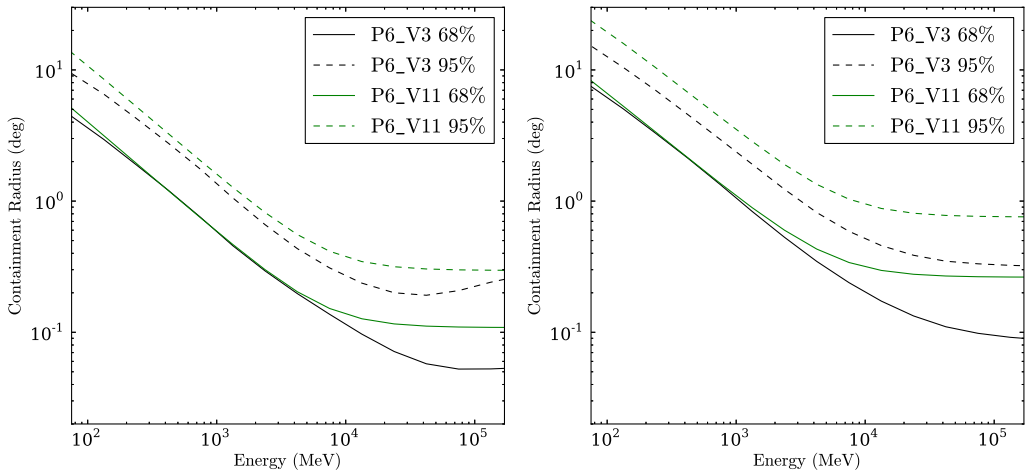

Figure 7.1 Comparison of 68% (solid lines) and 95% (dashed lines) containment radii of the MC and on-orbit PSF models for front- (left) and back-converting (right) events.

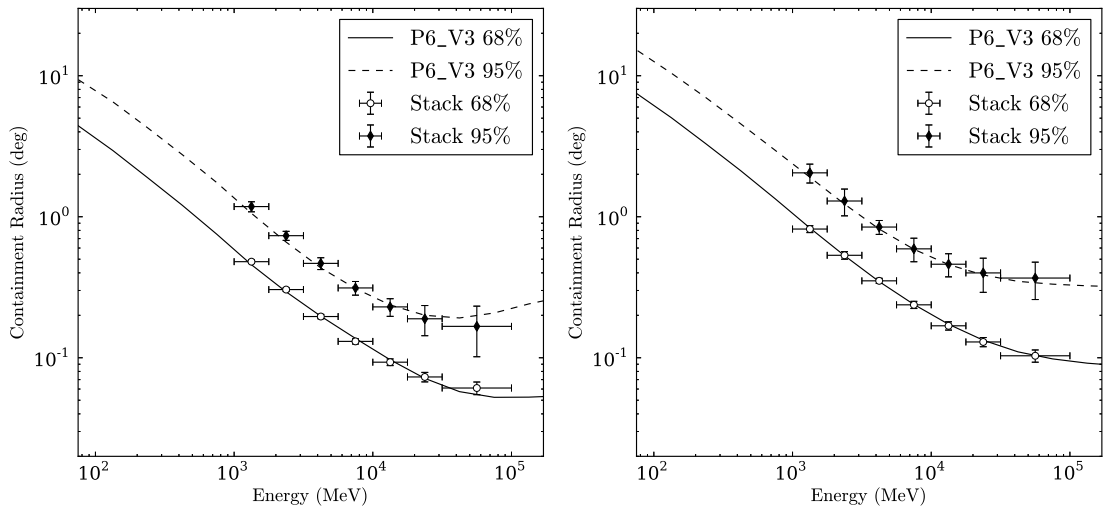

Figure 7.2 68% (white points) and 95% (black points) PSF containment radii inferred from applying the on-orbit PSF analysis to a simulated AGN sample (Stack) with the same properties of the calibration AGN sample generated with the `P6_V3` PSF for front- (left) and back-converting (right) events. Solid lines show the containment radii predicted by the same IRF used to generate the simulation.

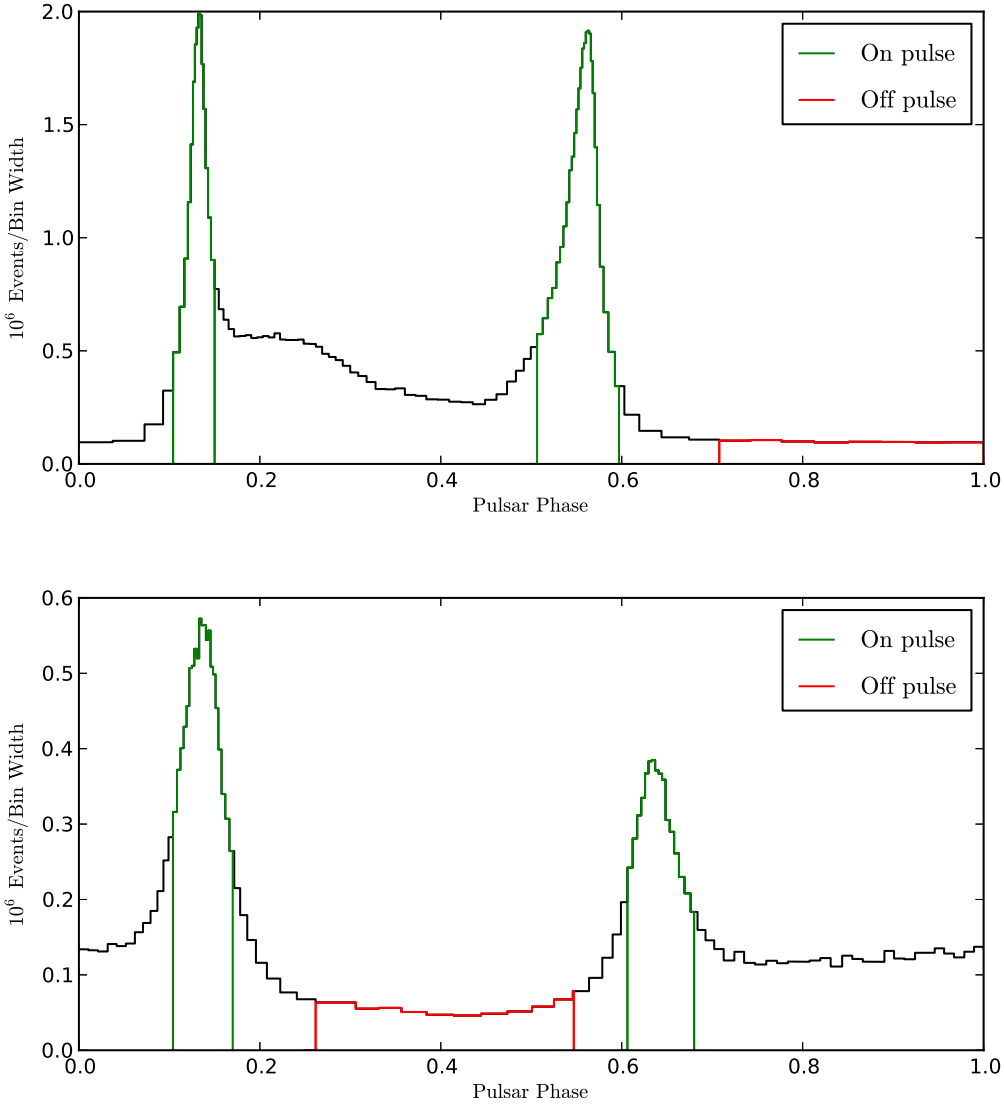

Figure 7.3 Light curve for all γ rays above 100 MeV within 4° of the Vela (above) and Geminga (below) pulsars in 100 fixed-count phase bins. The on- and off-pulse phase selections are identified in green and red, respectively.

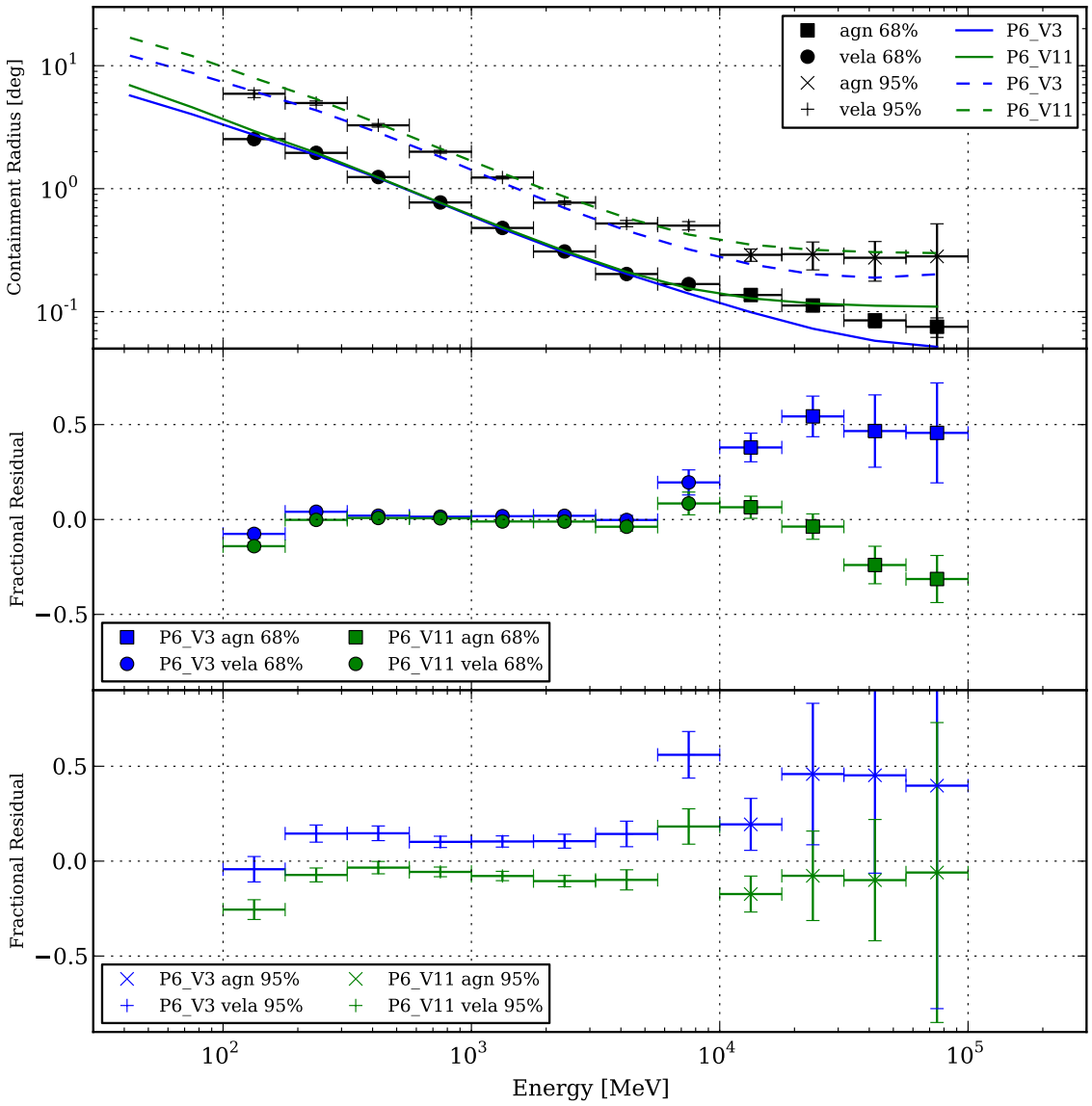

Figure 7.4 Containment radii for *front* events as determined from the angular distributions of Vela and the stacked AGN sample. Solid and dashed curves show the 68% and 95% containment radii, respectively, given by the model predictions for the `P6_V3` and `P6_V11` instrument response functions, for an observing profile corresponding to the Vela pulsar and a power-law energy distribution with photon index $\Gamma = 2$. The middle and lower panels show the fractional residual between the Vela and stacked AGN PSFs and the different IRFs for the 68% and 95% PSF containment radii, respectively.

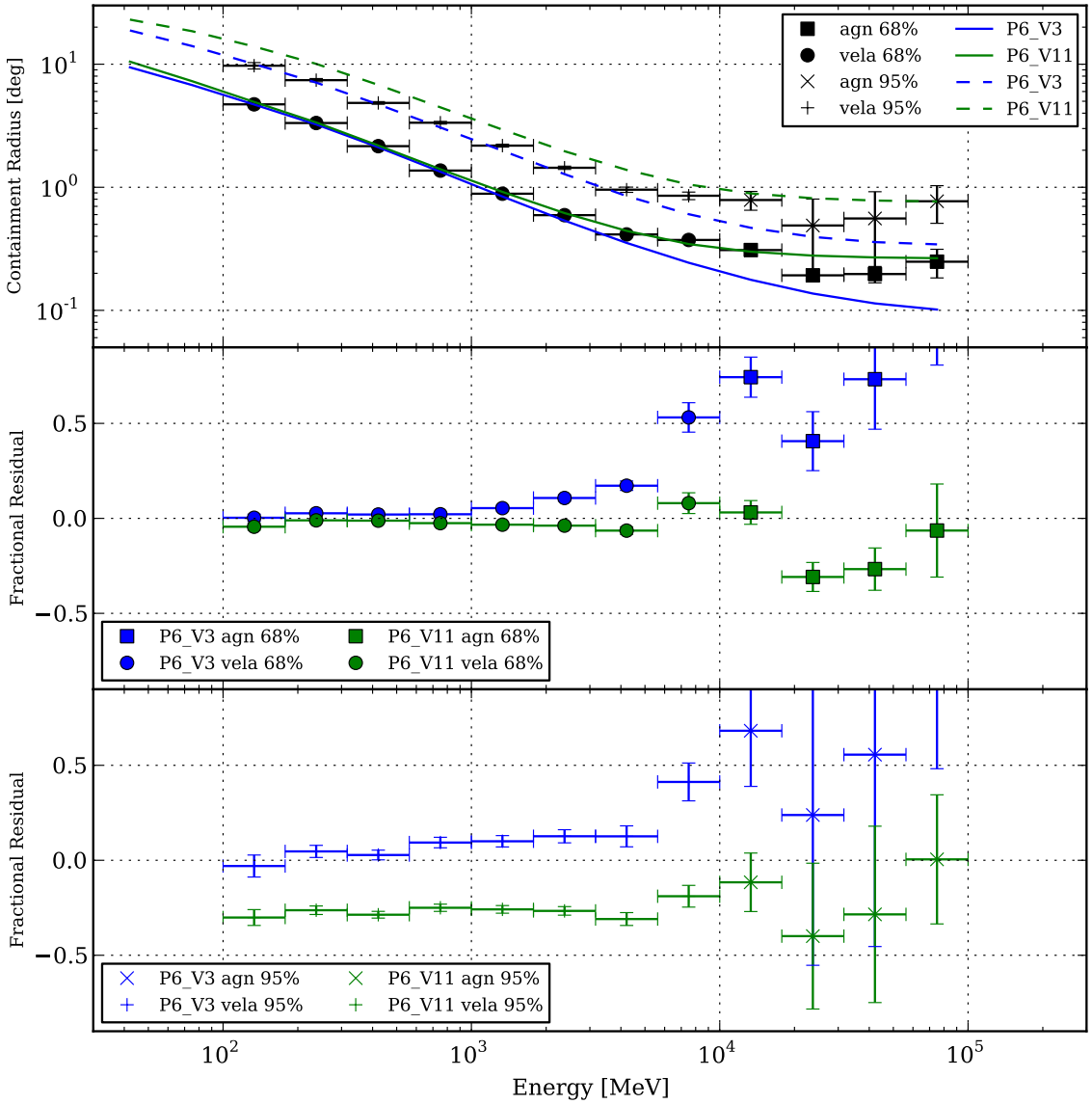

Figure 7.5 Same as for Figure 7.4, but for *back* events.

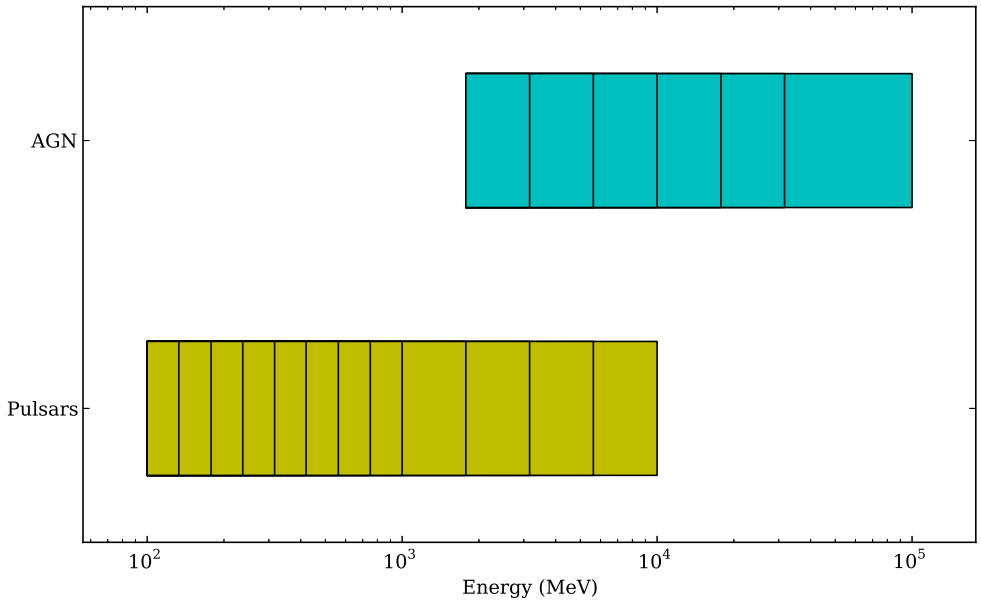

Figure 7.6 The energy bins for the theta-dependent on-orbit PSF analysis. The pulsar emission can be effectively separated from the background between 100 MeV to 10 GeV and provide significant statistics below 1 GeV. The AGN have emission at all energies, but begin to overlap with other sources at 1 GeV.

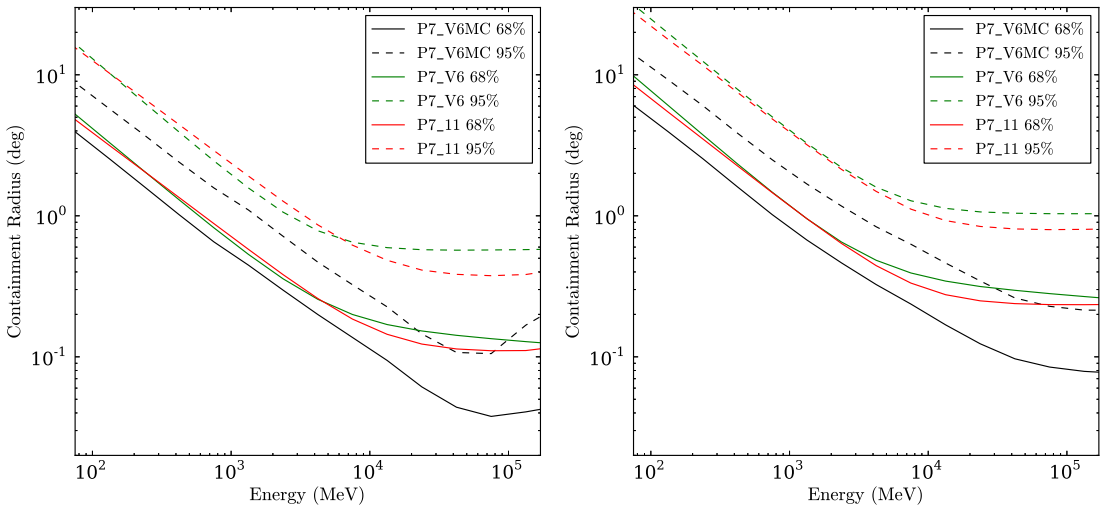

Figure 7.7 A comparison between the 68 and 95% containment radii ($A_{\rm eff}$-averaged) for the MC PSF (`P7_V6MC`), the on-orbit PSF from Section 7.1 for `Pass7` data (`P7_V6`), and the PSF generated from Section 7.4 with inclination-angle dependence (`P7_V11`). The PSFs are plotted for both *front* and *back* converting γ rays. The discrepancy between data and MC is present in both conversion types, most prominently above 10 GeV.

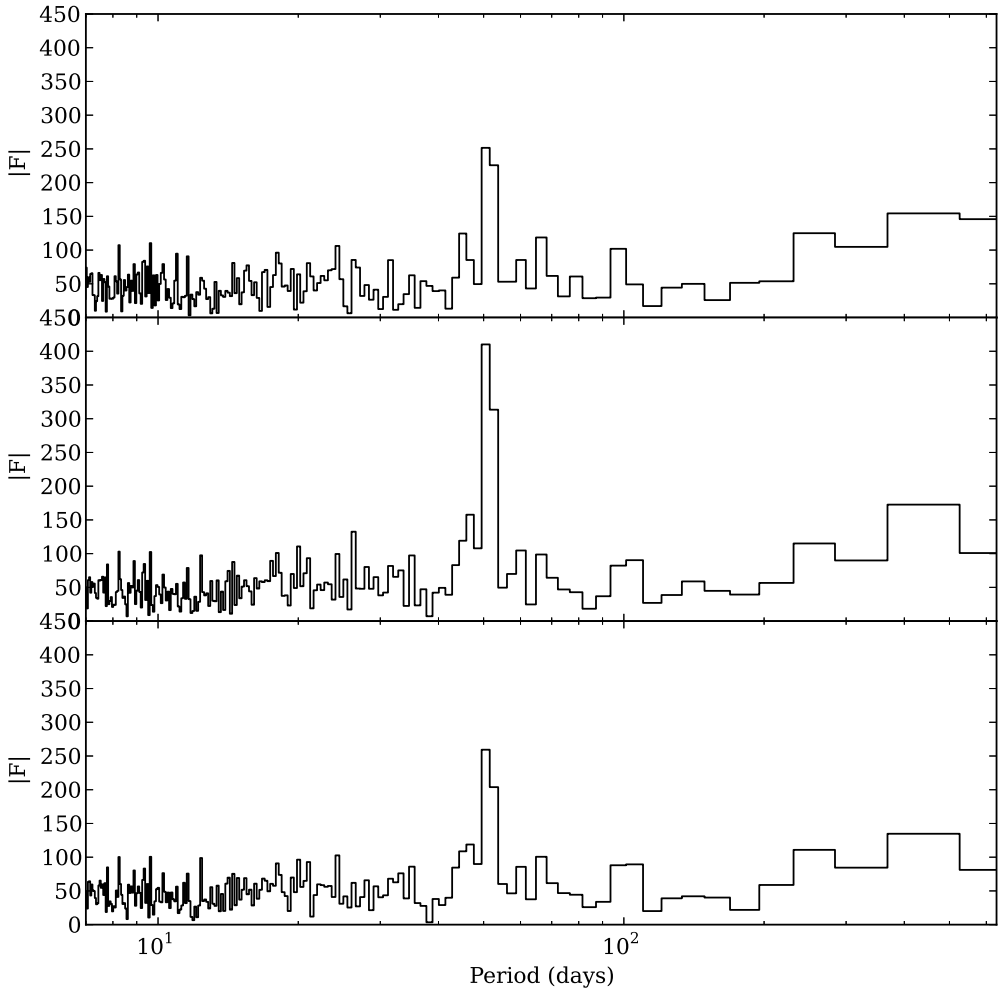

Figure 7.8 The square root of the power density spectrum (PDS) $|F|$ of the weekly estimate of the total flux for the Vela pulsar for γ rays with energy above 70 MeV. The PDS is shown for the MC PSF (top, `P7SOURCE_V6MC`), the inclination-angle independent on-orbit PSF (middle, `P7SOURCE_V6`), and the inclination angle-dependent on-orbit PSF (bottom, `P7SOURCE_V11`). The large peaks in the spectrum at 50−52 days correspond to the 53.4-day precession period of the LAT's orbit and have a significance $> 4\sigma$ over the null distribution.

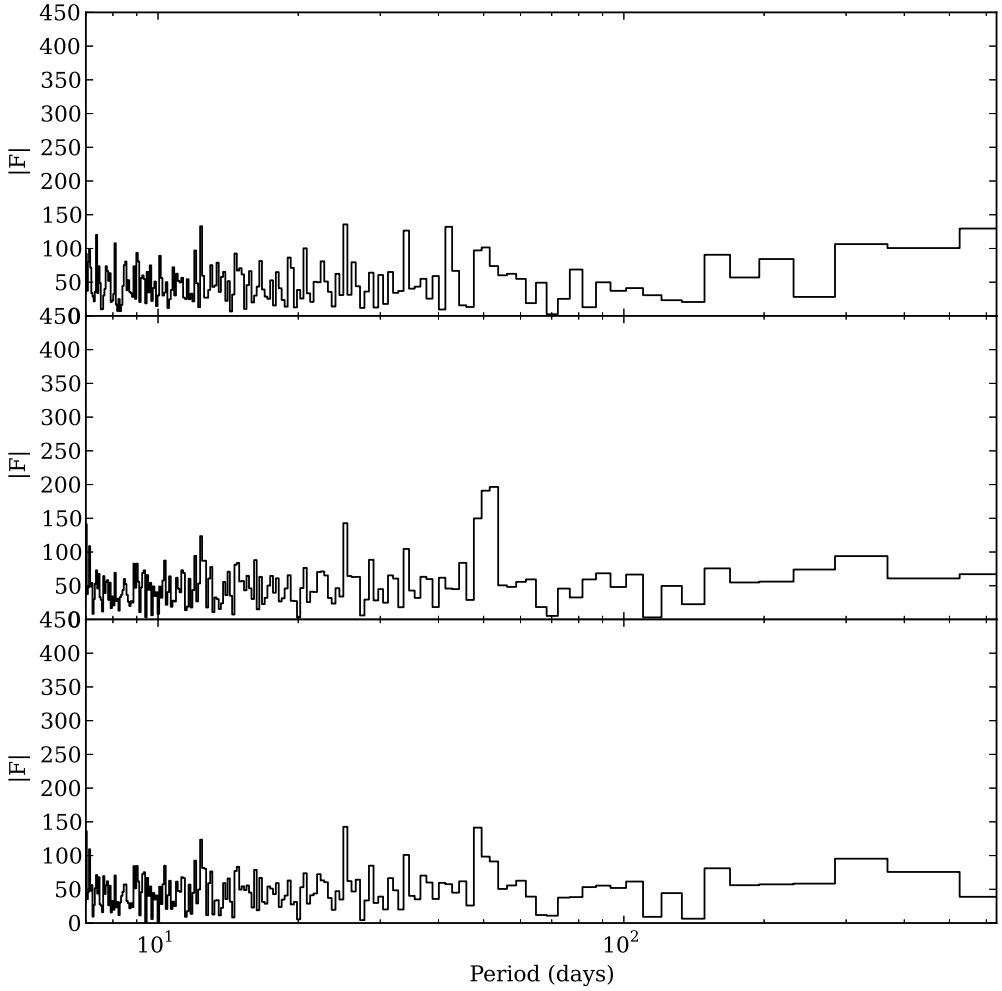

Figure 7.9 Same as 7.8, but with the Geminga pulsar. The peak at orbital precession period (53.4 days) is reduced for all PSFs, but still contains significance of $> 4\sigma$ for `P7SOURCE_V6` (middle) as expected since the PSF has no inclination angle dependence.

Chapter 8

The Intergalactic Magnetic Field

8.1 Overview

In Chapter 7, we derived the PSF under the assumption that the spatial size of AGN jets is not resolved the by the LAT. Interaction of TeV γ rays with the extragalactic-background light (EBL) and the magnetic fields in intergalactic space, however, can broaden the spatial size of AGN. The consistency between the PSF and data from pulsars in Section 7.2 indicates that the broadening must be a small effect. Here, we characterize the effects of the intergalactic magnetic field on high energy emission of AGN and the prospects for LAT observation.

Relatively weak (μG) magnetic fields have been observed in galaxies and galaxy clusters by measurements of Zeeman splitting and Faraday rotation of radio emission (Beck, 2008; Kulsrud & Zweibel, 2008). While the precise origin of these fields is not well understood, there are models for the evolution of the galactic fields involving a growing magnetic hydrodynamic (MHD) mode from 'seed' fields (i.e. $\alpha - \Omega$ dynamo, Kulsrud & Zweibel, 2008). In the intergalactic medium (IGM), these seed magnetic fields remain relatively unamplified, with upper limits on their magnitude of $\sim 10^{-11}$ G from Faraday rotation measures of galaxy clusters (Beck, 2008). The seed fields (IGMF) themselves are most likely cosmological in origin, arising during the early Universe or galaxy formation. The exact properties of the seed fields in terms of magnitude B_I or spatial coherence λ_B are still relatively unconstrained, with B_I between $10^{-18} - 10^{-6}$ G and λ_B between $\sim 10^{-5}$ pc and the Hubble distance (Neronov & Semikoz, 2009). While the majority of observations have been direct detection of radio and optical effects (e.g. Heiles & Troland, 2004; Kronberg & Simard-

Normandin, 1976), we introduce the 'pair-halo' effect in the high energy γ-ray emission of AGN to characterize these properties.

The mean free path for γ rays interacting with the EBL $\lambda_{\gamma\gamma}(E)$ decreases significantly above a 100 GeV and reaches a minimum at an energy corresponding to the peak of the cosmic microwave background radiation (CMB) energy spectrum. At low redshifts ($z \ll 1$), this corresponds to an energy of 10^{15} eV (Aharonian, 2004) with $\lambda_{\gamma\gamma}(1000 \text{ TeV}) \approx 10$ kpc. The interactions of the γ rays and the EBL primarily produce e^+e^- pairs, each with roughly half of the energy of the primary γ ray. Since the pairs are still relativistic, they scatter the EBL into γ rays through inverse Compton and lose energy through this 'cascade' emission. Many AGN produce multi-TeV γ rays, most likely through the process of synchrotron self-Compton, where the synchrotron emission of relativistic electrons in AGN jets is scattered through inverse Compton by the same population of electrons. AGN also exhibit signs of EBL attenuated spectra, primarily through the $\gamma - \gamma$ interactions (Finke et al., 2010). In this chapter, we examine *Fermi*-LAT data for evidence of IGMF through the pair-halo emission of AGN.

8.2 Pair-Halo Phenomena

The canonical 1-zone SSC model of AGN is characterized by a doubly peaked spectrum: the first peak corresponds to a population of relativistic electrons emitting synchrotron radiation and the second corresponds to the inverse Compton scattering by the electrons of the synchrotron emission. The inverse Compton spectrum is often modeled as an exponential cutoff

$$\frac{dN}{dE} \propto E^{-\Gamma} \exp\left(-\frac{E}{E_{cut}}\right) \tag{8.1}$$

with E_{cut} corresponding to roughly to kinematic limit $4\gamma^2 E_{synch}$ for electrons with Lorentz factors γ and peak synchrotron energy E_{synch}. For HSP AGN, the peak of the inverse Compton component of the spectrum will often be in the TeV range and the photon index Γ is between 0.2 to 0.9. If the distance to the AGN is comparable to the mean free path for EBL $\gamma\,\gamma$ interaction ($z \approx 0.1$), the spectrum will be suppressed at high energies and produce

secondary, lower energy γ rays. The e^+e^- pairs produced in the EBL cascades create the secondary γ rays over a distance $\lambda_T \approx 3m_ec^2/4\sigma_T u_{CMB}\gamma$, where σ_T is the Thomson cross section and u_{CMB} is the energy density of the CMB. For pairs with a Larmor radius $r_L = \gamma m_e c^2/eB_I$ in the IGM comparable to the electron cooling length λ_T, the secondary γ-ray emission will be deflected away from the primary γ-ray direction by an angle $\theta_B = \lambda_T/r_L$ (Dermer et al., 2011). The quantity θ_B characterizes the deflection of secondary emission and allows us to characterize three cases in terms of the emission cone of the AGN (θ_{AGN}):

- $\theta_B \ll \theta_{AGN}$ - The observed secondary emission is unaffected as the electrons cool through Thomson losses before deflection.
- $\theta_B \gg 1$ - The observed secondary emission is reduced by a factor $\sim \theta_{AGN}^2/4$ relative to the lossless case and the electrons Thomson-cool isotropically.
- $\theta_{AGN} < \theta_B \ll 1$ - The observed secondary emission is spatially extended compared to the jet and the reduction is highly energy dependent. The dependence for a $\Gamma = 1/2$ spectrum can be derived analytically and the secondary spectrum follows $dN/dE \propto E^{3/2}$ (Tavecchio et al., 2010).

For a source at a distance d from Earth, the observed deflection of the γ rays will be $\theta_d(E) = \lambda_{\gamma\gamma}(E)\theta_B/d$ and the deflection will appear as a 'halo' if $\theta_d(E) > \theta_{PSF}(E)$, where $\theta_{PSF}(E)$ is the angular resolution of the instrument (Dermer et al., 2011). Figure 8.1 shows the geometry of the pair cascades with respect to the beam size and the finite angular resolution of the LAT. As we noted in Section 4.2, the angular resolution of the LAT is also energy dependent, with

$$\begin{cases} \theta_{PSF} \approx E^{-0.8} & E < 3 \text{ GeV} \\ \theta_{PSF} \approx \theta_{TKR} & E > 3 \text{ GeV} \end{cases} \tag{8.2}$$

where θ_{TKR} is the intrinsic resolution of the LAT from the instrument-pitch/track-length ratio. The *front*-converting γ rays have significantly better angular resolution over *back*-converting γ rays and give the best opportunity to see this effect. However, since the on-orbit PSF we derived in Section 7.1 used AGN as the calibration sample, we felt this may introduce a bias in the estimation of a pair-induced halo around AGN. In contrast,

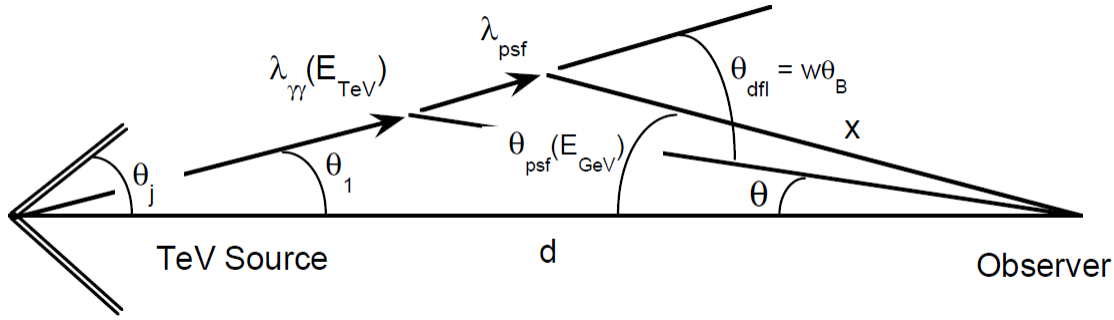

Figure 8.1 The geometry of the pair-halo emission and the intergalactic magnetic field (IGMF, reproduced from Dermer et al., 2011). θ_j is the opening angle of the AGN jet, $\lambda_{\gamma\gamma}$ is the mean free path for the TeV pair conversion, θ_{dfl} is the deflection angle due to the magnetic field, and λ_{PSF} is the effective distance along the trajectory that can be resolved by the LAT. If $\lambda_{PSF} \ll \lambda_{\gamma\gamma}$, the LAT can effectively distinguish the extended spatial emission due to the IGMF.

the pulsed γ-ray emission from any pulsar appears as a true point source to the LAT and the pulsar emission can be effectively separated from the background of any surrounding nebula and of the diffuse interstellar and extragalactic emission through the phase-based background subtraction technique described in Section 7.2. In the following sections, we place limits on the angular extension of AGN emission relative to pulsar emission and present an analysis that evaluates the significance of two extended angular profiles for BL Lac blazar populations and TeV sources, using pulsars as calibration sources.

8.3 Maximum Likelihood Analysis in Angular Bins

To test for the presence of pair halos around AGN, we use a joint likelihood for the angular distributions of γ rays around AGN and pulsars in the same manner as Section 7.4. The γ rays are binned into three logarithmic energy intervals from $1-31.6$ GeV. Additionally, the γ-ray sample is binned in angular offset from their presumed source such that there are an equal number of counts in each of 12 angular bins for the on-pulse counts from the Vela pulsar. Since the Vela pulsar emission is an order of magnitude brighter than the background intensity in the on-pulse phase, this choice of binning ensures that the point-source statistics are roughly the same for all sources in each angular bin. The *front* converting events have rates of residual cosmic rays and better angular resolution than the

back events, and therefore we limit the analysis to these γ rays.

We used a non-parametric representation of the PSF given by the fraction of events (m_i) in each of the 12 angular bins, providing a more direct comparison between the pulsar and AGN angular distributions by removing any dependence of the analysis on the choice of PSF parameterization. The model for the angular distribution of γ rays for the on-pulse pulsar emission, ν_i^{on}, is expressed as

$$\nu_i^{on} = N^{psr} m_i + \alpha \, \nu_i^{off} \ , \tag{8.3}$$

where N^{psr} is the number of γ rays attributed to the pulsar in the on-pulse phase, ν_i^{off} is the model for the number of off-pulse γ rays in angular bin i, m_i is the PSF weight in angular bin i, and α is the ratio of the width of the on and off-pulse phase selections. This model is identical to that of Section 7.4. We chose Vela and Geminga as calibration sources for this analysis, as these pulsars have the largest number of source γ rays above 100 MeV and weak or undetected associated nebular emission. The on- and off-pulse data samples were defined using the phase ranges from Table 7.2 and the angular bin ranges, counts, and models are shown in Tables 8.1 − 8.3.

The model of the angular distribution of γ rays from AGN is the sum of three components: point-source emission, a uniform background, and extended (halo) emission. It is given by

$$\nu_i^{agn} = N^{agn} m_i + N^{iso} b_i + N^{halo} h_i^*(\theta_0) \ , \tag{8.4}$$

where N^{agn} is the MLE for the number of γ rays attributed to the AGN, N^{iso} and b_i are the MLE's for the number and fraction of γ rays in angular bin i for the isotropic model, and N^{halo} and $h_i^*(\theta_0)$ are the MLE's for the total and fraction of γ rays in angular bin i for the halo model, h_i, convolved with the PSF. The isotropic fractions, b_i, were calculated from the fraction of solid angle in the ROI contained in angular bin i. For the halo models tested in this work, h_i has a single parameter, θ_0, corresponding to a characteristic halo size. We convolved the halo model with a single King function that was fit to the PSF weights in the null halo case.

Given the observations $\vec{n}^{on}, \vec{n}^{off}$, and $\vec{n}^{agn}$ corresponding to the on- and off-pulse pulsar and AGN counts in each of the 12 angular bins, the joint likelihood for the stacked pulsars and AGN is a modification to the log-likelihood of Equation 7.5

$$\begin{aligned}
\log L(\vec{m}, \vec{b}, \alpha, N^{psr}, \vec{\nu}^{off}, N^{agn}, N^{iso}, N^{halo}, \theta_0 \mid \vec{n}^{on}, \vec{n}^{off}, \vec{n}^{agn}) = \\
\sum_{i}^{angular\ bins} \log L_P(\ \nu_i^{on}(m_i, N^{psr}, \nu_i^{off}, \alpha)\ \mid\ n_i^{on}) + \\
\sum_{i}^{angular\ bins} \log L_P(\ \nu_i^{off}\ \mid\ n_i^{off}) + \\
\sum_{i}^{angular\ bins} \log L_P(\ \nu_i^{agn}(m_i, b_i, N^{agn}, N^{iso}, N^{halo}, \theta_0)\ \mid\ n_i^{agn})\ ,
\end{aligned} \tag{8.5}$$

where

$$\log L_P(\nu \mid n) = n \log \nu - \nu - \log n! \tag{8.6}$$

is the log-likelihood for observing n γ rays given ν predicted by the model. The joint likelihood is then evaluated with the data given the model, and then maximized with respect to all model parameters. Parameter uncertainties were calculated by profiling the log-likelihood in Equation 8.5.

Various models for the angular profile of halo emission induced by the IGMF have been considered (Aleksić et al., 2010; Ando & Kusenko, 2010; Elyiv et al., 2009). Here we consider both Gaussian and Disk models; these can be expressed as

$$\frac{dN_{gauss}}{d\Omega} = h(\theta, \theta_0) = \frac{1}{\pi\theta_0^2} \exp\left(-\frac{\theta^2}{\theta_0^2}\right) \tag{8.7}$$

and

$$\frac{dN_{disk}}{d\Omega} = h(\theta, \theta_0) \propto \begin{cases} \frac{1}{\pi\theta_0^2} & \theta < \theta_0 \\ 0 & \theta > \theta_0\ . \end{cases} \tag{8.8}$$

where both equations are normalized with the small angle approximation, $d\Omega = 2\pi\theta d\theta$. The Disk and Gaussian models were chosen to bracket the shape of the model tested by Ando &

Table 8.1. Statistics for the Vela and Geminga pulsars and the low and high redshift BL Lacs in the energy range $1000 - 3162$ MeV for the analysis in Section 4.2. The models for the on-pulse selection ν_i^{on} are displayed next to the number of counts n_i^{on} in each angular bin. The BL Lac model counts ν_i^{agn} are fit for the null case ($N^{halo} = 0$) in Equation 7.5.

		Vela		Geminga		BL Lac ($z < 0.5$)		BL Lac ($z > 0.5$)	
Bin edges (deg)	m_i	ν_i^{on}	n_i^{on}	ν_i^{on}	n_i^{on}	ν_i^{agn}	n_i^{agn}	ν_i^{agn}	n_i^{agn}
$0.000 - 0.083$	0.083	996.3	955	516.7	560	442	450.8	203	214.0
$0.083 - 0.124$	0.083	999.9	988	512.7	525	478	463.9	206	215.9
$0.124 - 0.160$	0.083	999.8	996	519.0	523	486	472.4	249	222.7
$0.160 - 0.199$	0.084	1000.8	1012	518.7	507	533	493.8	258	226.5
$0.199 - 0.239$	0.083	1000.1	981	512.2	532	514	502.5	218	224.4
$0.239 - 0.283$	0.083	1000.3	1008	518.0	510	508	519.2	205	227.0
$0.283 - 0.336$	0.084	1004.3	1026	510.3	488	601	570.9	255	240.5
$0.336 - 0.406$	0.084	1006.0	1034	513.9	485	667	648.3	250	254.4
$0.406 - 0.493$	0.083	1004.6	999	513.2	519	634	737.7	288	278.3
$0.493 - 0.630$	0.083	1013.6	995	513.0	532	1088	1076.9	317	340.5
$0.630 - 0.875$	0.083	1034.3	1052	517.9	500	1799	1967.6	496	524.7
$0.875 - 4.000$	0.082	1874.3	1902	765.8	743	64785	64631.0	13303	13279.2

Kusenko (2010), with the Disk and Gaussian respresenting the limiting cases of a sharply peaked and broad distribution, respectively. A test statistic for the halo models as a function of θ_0 was constructed by evaluating the difference between the maximum likelihood of the halo model ($L(N^{halo}, \theta_0)$) and the maximum likelihood of the null hypothesis ($L(0, \theta_0)$).

$$TS_{halo}(\theta_0) = 2(\log L(N^{halo}, \theta_0) - \log L(0, \theta_0)) \tag{8.9}$$

where all parameters besides θ_0 are left free. Given the constraint that $N^{halo} > 0$ and the null case is on the boundary of the parameter space (i.e. $N^{halo} = 0$), the significance of the pair halo component with characteristic extension θ_0 is $S = \sqrt{TS}\sigma$, provided that the number of γ rays associated with the pulsars and AGN, N^{psr} and N^{agn}, is larger than ~ 20 (Mattox et al., 1996; Protassov et al., 2002). To verify the TS is distributed as Equation 8.9, we run a MC of the angular bin models for both the AGN and pulsars and calculate the TS through the analysis. We confirmed the distribution of the TS is distributed as $\sim \chi_1^2$.

8.4 Limits on the pair-halo emission of 1FGL BL Lac Sources

We begin by examining the BL Lac type AGN which were detected in the Fermi energy range. This class of AGN was selected due to the inferred emission extending into the TeV

Table 8.2. As Table 8.1 with the energy range $3162 - 10000$ MeV.

Bin edges (deg)	m_i	Vela ν_i^{on}	Vela n_i^{on}	Geminga ν_i^{on}	Geminga n_i^{on}	BL Lac ($z < 0.5$) ν_i^{agn}	BL Lac ($z < 0.5$) n_i^{agn}	BL Lac ($z > 0.5$) ν_i^{agn}	BL Lac ($z > 0.5$) n_i^{agn}
$0.000 - 0.043$	0.083	177.6	175	104.4	107	156	148.4	71	59.8
$0.043 - 0.063$	0.083	178.9	182	104.1	101	133	141.5	62	58.7
$0.063 - 0.082$	0.084	179.0	188	105.1	96	145	145.9	50	56.8
$0.082 - 0.099$	0.083	178.7	196	104.4	87	162	151.7	62	58.8
$0.099 - 0.121$	0.083	178.8	167	104.1	116	170	155.3	53	57.5
$0.121 - 0.142$	0.084	179.1	175	105.8	110	177	158.3	72	60.9
$0.142 - 0.166$	0.083	178.6	184	104.4	99	121	140.5	70	60.6
$0.166 - 0.196$	0.083	178.9	179	106.1	106	131	146.0	29	54.4
$0.196 - 0.237$	0.083	178.5	176	106.4	109	171	162.9	68	61.8
$0.237 - 0.292$	0.084	179.5	167	105.3	118	149	163.2	57	61.7
$0.292 - 0.408$	0.083	180.7	176	108.1	113	207	212.0	66	70.6
$0.408 - 4.000$	0.083	329.6	336	144.9	140	13821	13817.1	2753	2751.5

Table 8.3. As Table 8.1 with the energy range $10000 - 31623$ MeV.

Bin edges (deg)	m_i	Vela ν_i^{on}	Vela n_i^{on}	Geminga ν_i^{on}	Geminga n_i^{on}	BL Lac ($z < 0.5$) ν_i^{agn}	BL Lac ($z < 0.5$) n_i^{agn}	BL Lac ($z > 0.5$) ν_i^{agn}	BL Lac ($z > 0.5$) n_i^{agn}
$0.000 - 0.026$	0.078	12.1	12	3.9	4	53	51.6	9	10.3
$0.026 - 0.040$	0.088	13.6	13	4.4	5	61	59.0	8	10.7
$0.040 - 0.051$	0.088	13.6	11	4.4	7	55	54.6	17	14.3
$0.051 - 0.067$	0.088	13.6	10	4.4	8	62	59.8	12	12.3
$0.067 - 0.077$	0.083	12.9	13	4.1	4	33	37.4	16	13.5
$0.077 - 0.086$	0.088	13.6	16	4.4	2	44	46.4	11	11.9
$0.086 - 0.104$	0.088	13.6	14	4.4	4	57	56.2	11	11.9
$0.104 - 0.134$	0.088	13.6	13	4.4	5	72	67.5	23	16.9
$0.134 - 0.164$	0.088	13.6	17	4.4	1	43	46.1	11	12.1
$0.164 - 0.191$	0.083	12.9	13	4.1	4	46	47.6	5	9.3
$0.191 - 0.260$	0.088	13.6	14	4.4	4	60	59.8	14	13.8
$0.260 - 4.000$	0.053	38.2	42	8.7	6	3195	3194.9	638	637.9

Table 8.4. Statistics for the low-redshift BL Lacs in the energy range 31623 − 100000 MeV for the analysis in Section 4.3. The model for the BL Lacs, ν_i^{agn}, is displayed next to the number of counts, n, in each angular bin. $N^{agn}m_i$ is displayed to highlight the equal statistics of the BL Lacs in each angular bin.

		BL Lac ($z < 0.5$)			
Bin edges (deg)	m_i	$N^{agn}m_i$	$N^{iso}b_i$	ν_i^{agn}	n_i^{agn}
0.000 − 0.019	0.076	20.0	0.0	20.0	20
0.019 − 0.026	0.080	21.0	0.0	21.0	21
0.026 − 0.033	0.080	21.0	0.0	21.0	21
0.033 − 0.043	0.084	22.0	0.0	22.0	22
0.043 − 0.049	0.080	21.0	0.0	21.0	21
0.049 − 0.058	0.080	21.0	0.0	21.0	21
0.058 − 0.073	0.080	20.9	0.1	21.0	21
0.073 − 0.102	0.083	21.7	0.3	22.0	22
0.102 − 0.130	0.079	20.7	0.3	21.0	21
0.130 − 0.849	0.161	42.0	36.0	78.0	78
0.849 − 2.739	0.058	15.3	346.7	362.0	362
2.739 − 4.000	0.058	15.1	433.9	449.0	449

range with the expectation of $\gamma - \gamma$ interactions with the TeV primary γ rays and the EBL. In the *Fermi* LAT First AGN Catalog catalog (henceforth 1LAC, Abdo et al., 2010d), 115 of the BL Lac-type AGN have measured redshifts. The sources were split into low and high redshift groups defined by $z < 0.5$ and $z > 0.5$, respectively, to test for a redshift-dependent size difference, e.g., Ando & Kusenko (2010). The number of low- and high-redshift sources is 94 and 21, respectively. We used data from the `P6_V3` *Diffuse* event class from 4 August 4 2008 to 14 April 2012 (mission elapsed time, MET, in the range 239557417 s – 356197259 s) for the AGN sets, while the data for Vela and Geminga pulsars were further constrained by the time ranges of the available timing solutions, which ended at MET 287398136 s for Vela and MET 284549320 s for Geminga.

As in Section 7.1, we limit the energy range to be above 1 GeV for the stacked AGN to limit the contamination from nearby bright counterparts. The γ-ray data sets for the two redshift ranges were binned in energy with two bins per logarithmic decade. The significance of the halo component was evaluated with the likelihood defined in Equation 8.5, and the Gaussian and Disk halo parameters $\theta_0 = 0.1$, 0.5, and 1 degrees. No TS larger than 0.1 ($S \approx 0.3\sigma$) was seen for any of the redshift sets or halo parameters, so upper limits were derived for the fraction of γ-rays from the source attributable to the halo parameter

($f_{halo} = N^{halo}/(N^{halo} + N^{agn})$). This finding is in contrast to the results of Ando & Kusenko (2010), who found 3.5 σ significance for $0.5 - 0.8°$ extension ($f_{halo} = 0.073$) in the 3 – 10 GeV range for one year of LAT data for all 1FGL low-redshift AGN ($z < 0.5$) using *front*- and *back*-converting events. Over the same range of energy, a halo component of this magnitude ($f_{halo} = 0.073$) and angular size is excluded at the 1.5 σ and 2.7 σ levels for the 0.5° Gaussian and Disk models, respectively. The upper limits on f_{halo} are summarized in Tables 8.5 and 8.6 and plotted in Figures 8.2 and 8.3. For the smallest halo size, 0.1°, the upper limits are least constraining in the lowest energy range due to the similarity between the halo model convolved with the PSF and the PSF itself. The broader halo models, $0.5° - 1.0°$, are more similar to the isotropic model, so the limits for the broader Gaussian models are less constraining for all energies.

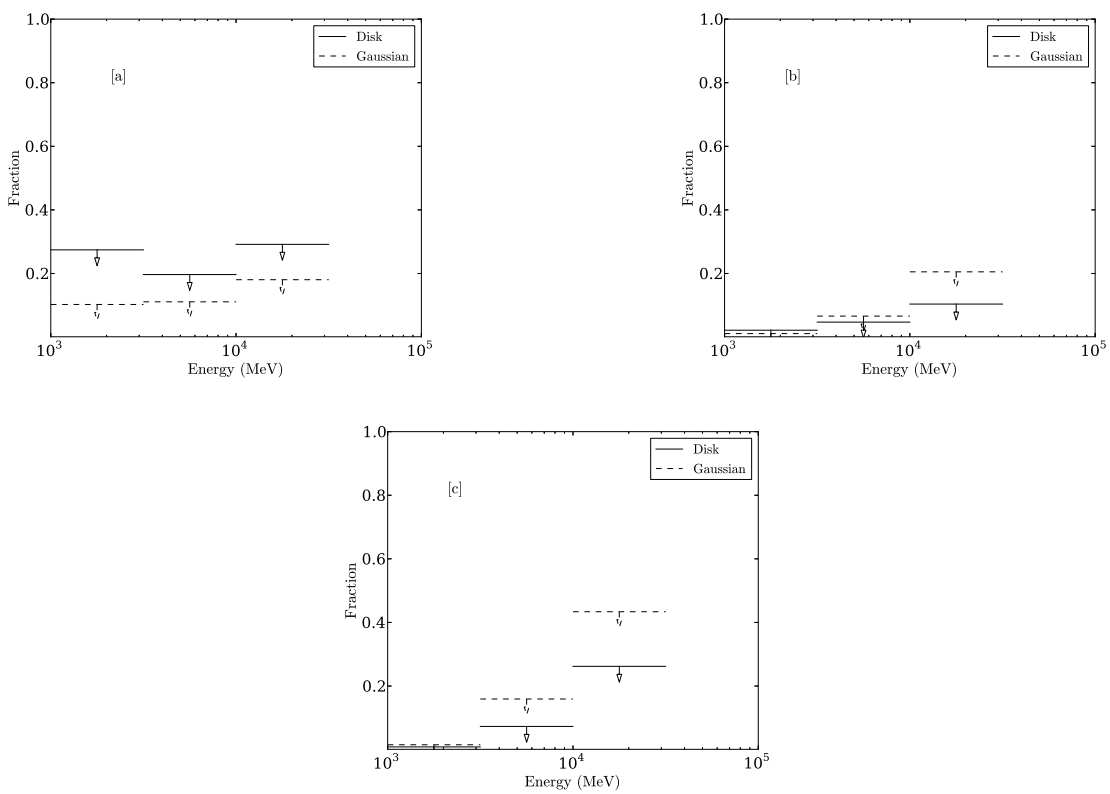

Figure 8.2 95% upper limits on the fraction of halo model γ rays from the low redshift BL Lacs, assuming a 0.1° (**a**), 0.5° (**b**), and 1.0° (**c**) halo.

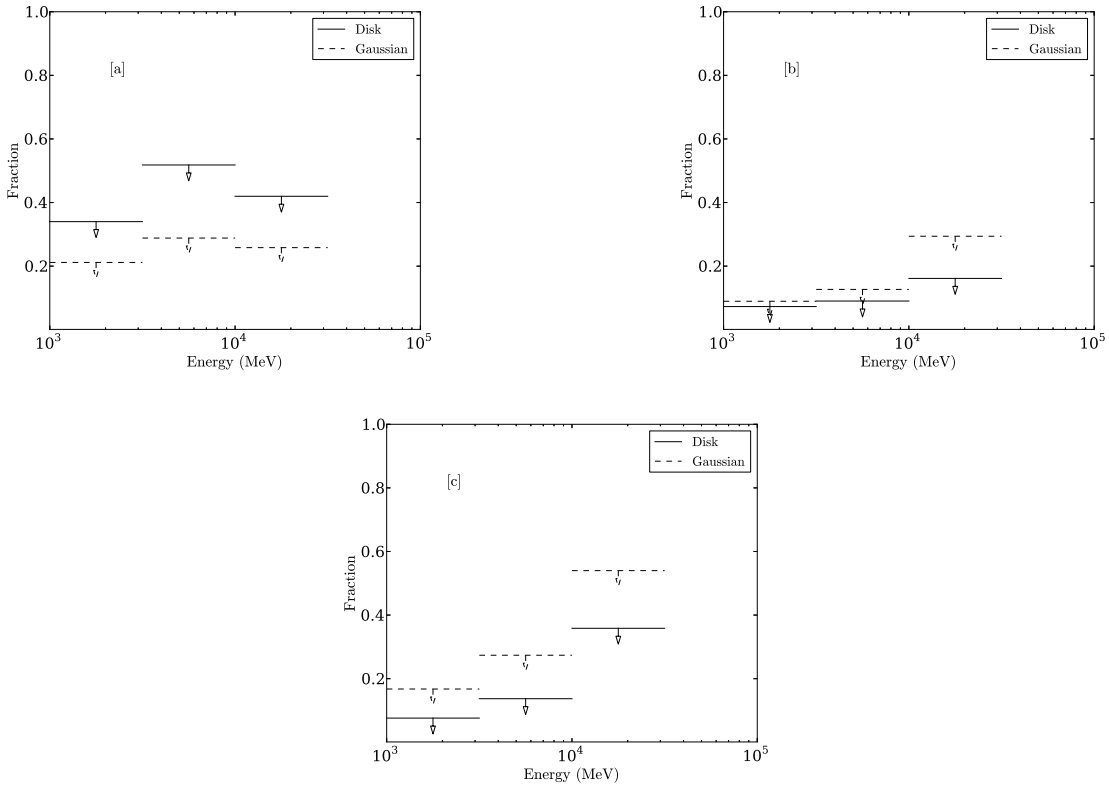

Figure 8.3 95% upper limits on the fraction of halo model γ rays from the high redshift BL Lacs, assuming a 0.1° (**a**), 0.5° (**b**), and 1.0° (**c**) halo.

8.5 Limits on the pair-halo emission of TeV BL Lacs

The TeV BL Lac-type AGN 1ES0229+200 ($z = 0.140$) and 1ES0347−121 ($z = 0.188$) are predicted to have detectable emission in the LAT energy range due to the suppression of the primary TeV γ rays from these sources by the EBL (Dermer et al., 2011; Neronov & Vovk, 2010; Tavecchio et al., 2010; Woo et al., 2005). The multi-TeV primary photons are converted into leptons that scatter EBL photons to GeV energies, unless the IGMF is sufficiently strong to deflect enough secondary pairs away from the line of sight (Neronov & Vovk, 2010). The blazar 1ES0229+200 provides the strongest constraint on the IGMF due to its significant TeV emission which extends to $\sim$ 10 TeV. The inferred primary spectrum from the synchrotron self-Compton of these sources are at or below the LAT sensitivity for an observation of 4 years, leaving the secondary processes as the primary detectable γ rays from these sources (Aharonian et al., 2007a; Dermer et al., 2011). Given that none of these

Table 8.5. Summary of the 95% C.L. upper limits on the fraction ($f_{halo} = N^{halo}/(N^{halo} + N^{agn})$) of γ-ray emission from low-redshift BL Lacs attributable to a halo component for the PSF convolved Disk and Gaussian halo models.

	Disk			Gaussian		
Energy (MeV)	$\theta_{halo} = 0.1°$	$\theta_{halo} = 0.5°$	$\theta_{halo} = 1.0°$	$\theta_{halo} = 0.1°$	$\theta_{halo} = 0.5°$	$\theta_{halo} = 1.0°$
1000 – 3162	0.27	0.02	0.01	0.10	0.01	0.02
3162 – 10000	0.20	0.04	0.07	0.11	0.07	0.16
10000 – 31623	0.29	0.10	0.26	0.18	0.20	0.43

Table 8.6. Summary of the 95% C.L. upper limits on the fraction ($f_{halo} = N^{halo}/(N^{halo} + N^{agn})$) of γ-ray emission from high-redshift BL Lacs attributable to a halo component for the PSF convolved Disk and Gaussian halo models.

	Disk			Gaussian		
Energy (MeV)	$\theta_{halo} = 0.1°$	$\theta_{halo} = 0.5°$	$\theta_{halo} = 1.0°$	$\theta_{halo} = 0.1°$	$\theta_{halo} = 0.5°$	$\theta_{halo} = 1.0°$
1000 – 3162	0.34	0.07	0.08	0.21	0.09	0.17
3162 – 10000	0.52	0.09	0.14	0.29	0.13	0.27
10000 – 31623	0.42	0.16	0.36	0.26	0.29	0.54

sources has been detected with strong significance in any LAT energy band, we examine the significance of the inferred reprocessed GeV emission of these sources, using the PSF-convolved Disk and Gaussian models with $\theta_0 = 0.1°, 0.5°$, and $1.0°$. We also examined the sources in the 32 to 100 GeV energy range.

Above 32 GeV, the statistics of pulsars in the dataset are insufficient to provide a template for the PSF γ rays, so we opted to use the low-redshift BL Lacs as the calibration sample in the 32 to 100 GeV energy range. We tested only for the significance of the halo model, setting $N^{agn} = 0$ in Equation 8.5 for those sources. As a result, the calibration samples were used only to determine the sizes of the angular bins. The AGN angular bin ranges, counts, and models are shown in Table 8.4.

There were no detections of $TS > 4$ ($S > 2$) in any energy band for 1ES0229+200, so we calculated the 95% upper limits on N^{halo} in each energy band. We converted the 95% upper limits into flux measurements by calculating the two-year exposure for each source, giving the results plotted in Figures 8.4 and 8.5 with H.E.S.S. and VERITAS measurements (Aharonian et al., 2007a,b; Perkins & VERITAS Collaboration, 2010). We find good agree-

ment between our upper limits and those derived by Neronov & Vovk (2010), Tavecchio et al. (2010), and Dermer et al. (2011).

For 1ES0347−121, we detect the source for all angular models in the energy range 3−32 GeV, most significantly for the 0.1° Disk model with a combined TS of 15. The TS increases with narrower angular models, indicating that the source is most likely a point source in this energy range. To examine the emission of the source between 100 MeV and 100 GeV, we used the unbinned *gtlike* application. All sources from the 2FGL catalog within 15° of the source were modeled with their 'catalog values' with the flux normalizations treated as a free parameters. The spectrum of 1ES0347-121 was modeled as a power law, with both the flux normalization and the power law index treated as free parameters. The TS of 1ES0347-121 reported by *gtlike* in this energy range was 49, corresponding to 7σ significance. While the source does not show signs of spatial extension, the detection of the source in the LAT energy range should provide constraints for broadband emission models based on optical, UV, and X-ray observations (Aharonian et al., 2007a).

8.6 Summary

In this chapter, we introduced the phenomenon of pair-halo emission from AGN and the effect of the IGMF on the observed flux from sources. We examined AGN that would be most likely to show evidence of interaction of the pair-halo cascades with the IGMF and found no significant emission component with spatial extension. We checked for redshift dependence of the pair-halo effect, but found no significant difference between the two populations of AGN sampled. We also examined AGN which show evidence of substantial pair-halo production and found no significant extended spatial emission. We calculated upper limits on emission for all sources and were able to rule out detections of pair-halos in AGN from LAT data.

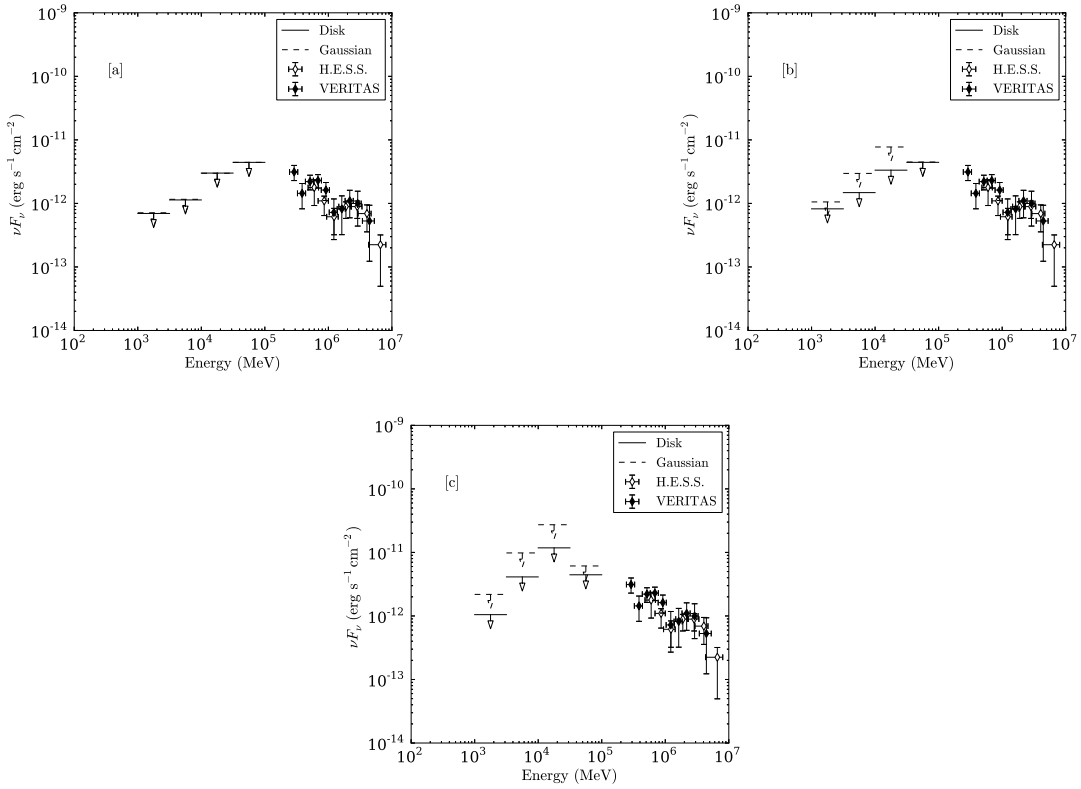

Figure 8.4 Upper limits on the energy flux from 1ES0229+200 at the 95% confidence level assuming a 0.1° (**a**), 0.5° (**b**), and 1.0° (**c**) halo, plotted with observations from HESS and VERITAS.

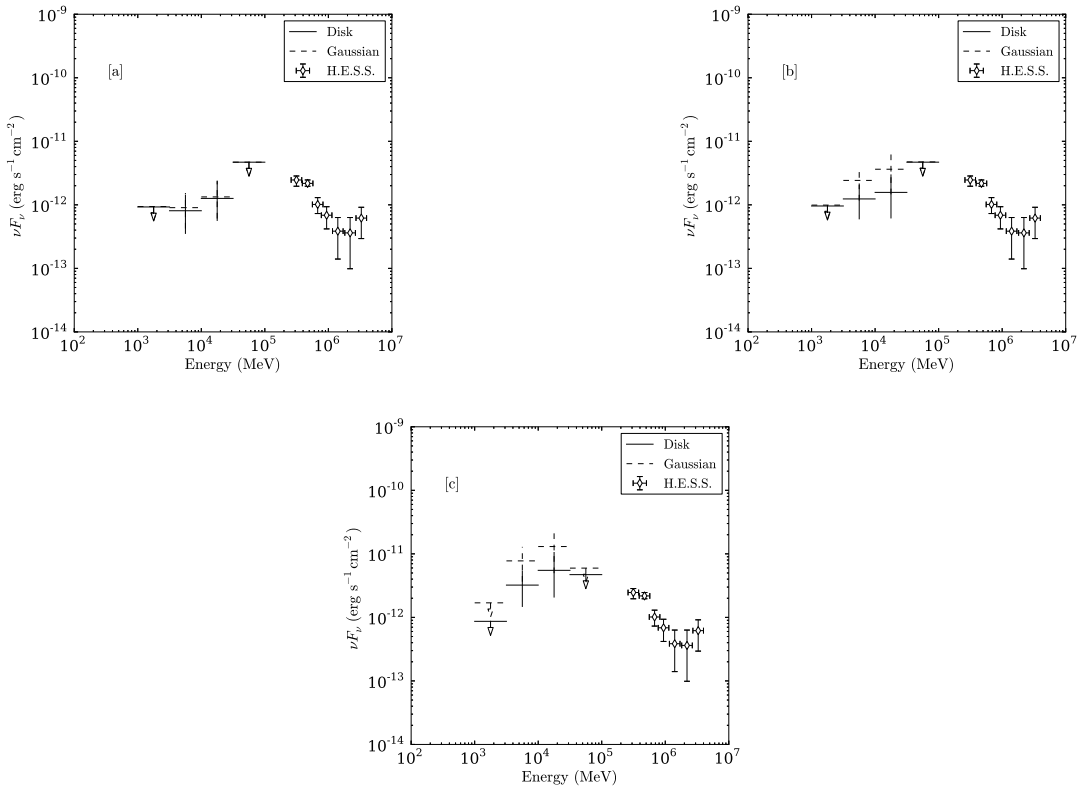

Figure 8.5 Upper limits on the energy flux from 1ES0347-121 at the 95% confidence level, plotted with observations from HESS assuming a 0.1° (**a**), 0.5° (**b**), and 1.0° (**c**) halo.

Chapter 9

Summary

The imaging properties of the *Fermi*-LAT has led to unprecedented observational capability of γ-ray point sources. In this work, we have examined the application of likelihood analysis to LAT data, specifically, to the angular models of sources and the performance of the LAT.

We examined the alignment of the LAT to the Fermi spacecraft by examining the angular distributions of γ rays around bright point sources. We found that the effects from the launch of the satellite created an offset between the LAT and spacecraft of $0.15°$. We examined the alignment parameters over various time ranges and found no significant changes, trends, or periodicity. The corrected alignment removes a small contribution to the high energy PSF, which has the best angular resolution.

We then determined the PSF on-orbit from a likelihood analysis, by examining the γ rays from bright AGN. We compared the results of the PSF determined from on-orbit data with the expectations from a simulation of the LAT performance. We found that the on-orbit PSF was broader, in general, at energies above 3 GeV. To cross-check the PSF generated from bright AGN, we examined the angular distribution γ rays from pulsar, and found nearly identical differences between the Monte Carlo. We examined sources of systematic uncertainty in the determination of the PSF and found that the calibration of the CAL light yield accounts for most of the discrepancy. We then derived a PSF that modeled the inclination angle dependence of the LAT and found that the systematic uncertainty in the measurement of the flux from bright sources is reduced considerably when using this PSF.

Finally, we presented an analysis of AGN to determine if there were significant pair-halo interactions with the weak intergalactic magnetic field and a broadening of sources. We

examined the angular distribution of γ rays around low- and high-redshift BL Lac blazars to look for evidence of broadening. We found no significant pair-halo emission from either redshift class and calculated upper limits on the emission for different angular models. We also examined two TeV sources to detect reprocessed pair-halo emission as a spatially extended source. We detected the TeV source 1ES0347-121 in the energy range 3-32 GeV, with the largest significance for the narrowest angular model. We found no evidence for spatial extension of either source.

Bibliography

Abdo, A. A., et al. 2009a, Phys. Rev. D, 80, 122004

—. 2009b, ApJS, 183, 46

—. 2009c, Astroparticle Physics, 32, 193

—. 2010a, ApJS, 188, 405

—. 2010b, ApJ, 713, 146

—. 2010c, ApJ, 720, 272

—. 2010d, ApJ, 715, 429

—. 2010e, ApJ, 713, 154

—. 2011a, ApJ, 736, 131

—. 2011b, Science, 331, 739

Ackermann, M., et al. 2011a, ApJ, 726, 35

—. 2011b, ApJ, 743, 171

Aharonian, F., et al. 2007a, A&A, 473, L25

—. 2007b, A&A, 475, L9

Aharonian, F. A. 2004, Very High Energy Cosmic Gamma Radiation (World Scientific Publishing Co. Pte. Ltd.)

Aleksić, J., et al. 2010, A&A, 524, A77+

Allison, J., et al. 2006, IEEE Transactions on Nuclear Science, 53, 270

Ando, S., & Kusenko, A. 2010, ApJ, 722, L39

Atwood, W. B., et al. 2009, ApJ, 697, 1071

Baldini, L., et al. 2007, AIP Conference Proceedings, 921, 190

Beck, R. 2008, in American Institute of Physics Conference Series, Vol. 1085, American Institute of Physics Conference Series, ed. F. A. Aharonian, W. Hofmann, & F. Rieger, 83–96

Bignami, G. F., et al. 1975, Space Science Instrumentation, 1, 245

Boinee, P., et al. 2003, in Science with the New Generation of High Energy Gamma-Ray Experiments : Between Astrophysics and Astroparticle Physics, ed. S. Ciprini, A. de Angelis, P. Lubrano, & O. Mansutti, 141

Carlson, P., Francke, T., Fuglesang, C., Weber, N., & Suffert, M. 1996, Nuclear Instruments and Methods in Physics Research Section A: Accelerators, Spectrometers, Detectors and Associated Equipment, 376, 271

Chernoff, H. 1954, Annals of Mathematical Statistics, 25, 573

Dermer, C. D., Cavadini, M., Razzaque, S., Finke, J. D., Chiang, J., & Lott, B. 2011, ApJ, 733, L21+

Du, Y. J., Qiao, G. J., & Wang, W. 2012, ApJ, 748, 84

Elyiv, A., Neronov, A., & Semikoz, D. V. 2009, Phys. Rev. D, 80, 023010

Fichtel, C. E., Hartman, R. C., Kniffen, D. A., Thompson, D. J., Ogelman, H., Ozel, M. E., Tumer, T., & Bignami, G. F. 1975a, ApJ, 198, 163

Fichtel, C. E., Kniffen, D. A., Thompson, D. J., & Ogelman, H. B. 1975b, in International Cosmic Ray Conference, Vol. 1, International Cosmic Ray Conference, 106–111

Finke, J. D., Razzaque, S., & Dermer, C. D. 2010, ApJ, 712, 238

Fossati, G., Maraschi, L., Celotti, A., Comastri, A., & Ghisellini, G. 1998, MNRAS, 299, 433

Grove, J. E., & Johnson, W. N. 2010, in Society of Photo-Optical Instrumentation Engineers (SPIE) Conference Series, Vol. 7732, Society of Photo-Optical Instrumentation Engineers (SPIE) Conference Series

Heiles, C., & Troland, T. H. 2004, ApJS, 151, 271

Hermsen, W., et al. 1981, in International Cosmic Ray Conference, Vol. 1, International Cosmic Ray Conference, 230–233

Hobbs, G. B., Edwards, R. T., & Manchester, R. N. 2006, MNRAS, 369, 655

Johnson, T. J., Çelik, Ö., Kerr, M., Harding, A. K., & Caliandro, G. A. 2009, ArXiv e-prints

Kanbach, G., et al. 1988, Space Sci. Rev., 49, 69

Kerr, M. 2011, ArXiv e-prints

Klebesadel, R. W., Strong, I. B., & Olson, R. A. 1973, ApJ, 182, L85

Kronberg, P. P., & Simard-Normandin, M. 1976, Nature, 263, 653

Kulsrud, R. M., & Zweibel, E. G. 2008, Reports on Progress in Physics, 71, 046901

Mattox, J. R., et al. 1996, ApJ, 461, 396

Moiseev, A. A., Hartman, R. C., Ormes, J. F., Thompson, D. J., Amato, M. J., Johnson, T. E., Segal, K. N., & Sheppard, D. A. 2007, Astroparticle Physics, 27, 339

Neronov, A., & Semikoz, D. V. 2009, Phys. Rev. D, 80, 123012

Neronov, A., & Vovk, I. 2010, Science, 328, 73

Neyman, J., & Pearson, E. S. 1928, Biometrika, 20A, 175

Nolan, P. L., et al. 2012, ApJS, 199, 31

Oegelman, H., Fichtel, C. E., & Kniffen, D. A. 1975, Nature, 255, 208

Perkins, J. S., & VERITAS Collaboration. 2010, in Bulletin of the American Astronomical Society, Vol. 42, AAS/High Energy Astrophysics Division #11, 708

Pollock, A. M. T., Masnou, J. L., Bignami, G. F., Hermsen, W., Swanenburg, B. N., Kanbach, G., Lichti, G. G., & Wills, R. D. 1981, A&A, 94, 116

Pollock, A. M. T., et al. 1985, A&A, 146, 352

Protassov, R., van Dyk, D. A., Connors, A., Kashyap, V. L., & Siemiginowska, A. 2002, The Astrophysical Journal, 571, 545

Read, A. M., Rosen, S. R., Saxton, R. D., & Ramirez, J. 2011, A&A, 534, A34

Romani, R. W., & Yadigaroglu, I.-A. 1995, ApJ, 438, 314

Ruderman, M. A., & Sutherland, P. G. 1975, ApJ, 196, 51

Sturrock, P. A. 1971, ApJ, 164, 529

Tavecchio, F., Ghisellini, G., Foschini, L., Bonnoli, G., Ghirlanda, G., & Coppi, P. 2010, MNRAS, 406, L70

The Fermi-LAT collaboration. 2010, ArXiv e-prints

Tibaldo, L. 2010, in American Institute of Physics Conference Series, Vol. 1223, American Institute of Physics Conference Series, ed. C. Cecchi, S. Ciprini, P. Lubrano, & G. Tosti, 89–98

Venter, C., Johnson, T. J., & Harding, A. K. 2012, ApJ, 744, 34

Weltevrede, P., et al. 2010, PASA, 27, 64

Wilks, S. S. 1938, Annals of Mathematical Statistics, 9, 60

Woo, J.-H., Urry, C. M., van der Marel, R. P., Lira, P., & Maza, J. 2005, ApJ, 631, 762

VITA

Marshall Roth was born in Tacoma, Washington. He earned his Bachelor of Science degree in Physics from the University of Washington in 2005. In 2012 he earned a Doctor of Philosophy from the University of Washington in Physics.